

Supercontinuum Pulse Shaping for the Optimal Control of Photo-Induced Processes



am
Fachbereich Physik
der
Freien Universität Berlin
eingereichte

Dissertation

vorgelegt von
Franz Philip Hagemann
aus Braunschweig

Berlin 2015

Erstgutachter: Prof. Dr. Ludger Wöste

Zweitgutachter: PD Dr. Christian Frischkorn

Tag der Disputation: 14. Dezember 2015

Abstract

This thesis set out to extend and improve the capabilities of supercontinuum laser light sources and to survey the potential of the new white-light laser setup in the optimal control of small metal clusters.

A new white-light laser setup, incorporating twofold filamentation in air for spectral broadening, ultrabroadband chirped mirrors for dispersion management and a pulse shaper setup has been developed. The twofold filamentation in air leads to a very stable spectral broadening, supplying a significant contribution in the visible (VIS) range, leading to an output spectrum spanning from 550 nm to 900 nm at 10 % of the maximum intensity. By offset-phase correction with the pulse shaper, this spectrum is compressed to 4.9 fs pulses spanning from 510 to 950 nm, with pulse energies of up to 60 μJ and a peak power of 12 GW. These supercontinuum few-cycle pulses serve as a starting point for the tailoring of near-arbitrary supercontinuum pulses with few-cycle subpulses. The tailoring of near-arbitrary amplified supercontinuum pulses is demonstrated for the first time. A home-built TG-FROG apparatus allows for the characterization of pulse forms that endure several hundreds of femtoseconds with few-cycle substructures.

This highly versatile white-light laser setup has been successfully deployed for the optimal control of the fragmentation during charge reversal of two small metal clusters, the copper trimer anion and the aluminum tetramer anion. The $(\text{Cu}_2^+ / \text{Cu}_3^+)$ product cation ratio was chosen as an objective for an evolutionary optimization, and was optimized by factors of up to three when compared to the cation yields obtained with a short 7 fs pulse. The obtained nontrivial optimal pulse shapes suggest a complex excitation mechanism involving a multitude of electronic states, in which the subpulses act in a cooperative manner, such that a higher fragmentation ratio is achieved. The obtained subpulse delays on the order of 10 fs are too fast to be probing vibrational dynamics, and thus likely are the signature of the initiation and probing of electronic wavepackets. CID experiments suggest that the fragmentation into Cu_2^+ occurs in an excited state of the neutral Cu_3 cluster, as neither Cu_3^+ nor Cu_3^- clusters fragment when irradiated with 7 fs pulses with wavelengths shorter than 540 nm blocked. Interestingly, Cu_3^- anions fragment into Cu^- anions, when irradiated with 7 fs pulses containing the wavelengths shorter than 540 nm, which could be the result of a decaying Cu^-Cu_2^+ ion pair state.

To test the broad applicability of the experimental technique and to see whether the results obtained for the copper trimer reproduce for a markedly different model system, the optimal control of the photofragmentation of Al_4^- cluster anions during charge reversal was studied. The $(\text{Al}^+ / \text{Al}_4^+)$ product cation ratio was chosen as an objective for optimization, yielding optimization factors of up to 3.4. As for the copper trimer, the obtained optimal pulses are very complex and feature subpulse delays on the order of 10 fs, which likely are the signature of electronic wavepackets. In general, the high optimization factors, obtained for two markedly different model systems, demonstrate the high selectivity in populating specific points on the potential energy surface attainable by the presented method.

Contents

Abstract	i
Abbreviations	iv
1 Introduction	1
2 Fundamentals	3
2.1 Ultrashort Laser Pulses	3
2.1.1 Time Domain Description	3
2.1.2 Frequency Domain Description	4
2.2 Generation of Ultrashort Laser Pulses	6
2.2.1 Mode Locked Femtosecond Oscillators	6
2.2.2 Chirped Pulse Amplification	9
2.2.3 Pulse Shaping	9
2.3 Nonlinear Optics	14
2.3.1 Second Harmonic Generation (SHG)	14
2.3.2 Intensity Dependent Refractive Index	15
2.3.3 Filamentation	16
2.4 Pulse Characterization	18
2.4.1 Autocorrelator and SHG FROG	18
2.4.2 TG-FROG	19
2.5 Coherent Control	23
2.5.1 Coherent Control experiments with adaptive feedback loops . .	25
3 White-Light Laser Setup	27
3.1 Introduction	27
3.2 Laser system	29
3.3 Supercontinuum Generation	30
3.4 Pulse Shaper Setup	32
3.4.1 Calibration of the LC-SLM	34
3.5 TG-FROG Setup	35
3.6 Pulse Compression	37
3.7 Supercontinuum Pulse Shaping	37
3.7.1 Fourier Shifts	38
3.7.2 Linearly Chirped Pulses	42
3.7.3 Pulse Trains	42
3.7.4 Summary	44
4 Molecular Beam Apparatus	47
4.1 Overview	47

Contents	iii
4.2 Ion Guiding Tandem Mass Spectrometer	47
4.3 Hexadecapole Ion Trap	49
4.4 Magnetron Sputtering Source	50
5 Integrated Optimal Control Setup	52
5.1 Temporal Resolution	52
5.2 NeNePo / Charge Reversal	54
5.3 Optimal Control Loop	55
5.4 GDD+GD Parametrization	56
5.5 Offset Phase Correction	56
5.6 Optimal Pulse Electric Field Determination	59
6 Experiments on the Copper Trimer	62
6.1 Introduction	62
6.2 Cu_3^- Cluster Preparation	62
6.3 White-Light Pulse Generation	64
6.4 Cu_3^- Charge Reversal Experiments	66
6.5 Optimal Control of the Cu_3^- Charge Reversal Process	67
6.6 Power Dependence of the Cu_3^- Charge Reversal	74
6.7 Laser-Induced Decomposition of Cu_3^-	74
6.8 Laser-Induced Decomposition of Cu_3^+	76
6.9 Conclusion	76
7 Experiments on the Aluminum Tetramer	79
7.1 Introduction	79
7.2 Al_4^- Cluster Preparation	80
7.3 White-Light Pulse Generation	80
7.4 Al_4^- charge reversal experiments	81
7.5 Optimal control of the Al_4^- charge reversal process	82
7.6 Power Dependence of the Al_4^- Charge Reversal	88
7.7 Conclusion	88
8 Summary and Outlook	90
8.1 Summary	90
8.2 Outlook	91
Bibliography	93
Kurzfassung	105
List of Publications	106
Danksagung	107
Eidesstattliche Erklärung	108

Abbreviations

AOM acousto-optic modulator

AOPDF acousto-optic programmable dispersive filter

BBO beta barium borate

BOXCARS crossed-beam phase-matched coherent anti-Stokes Raman scattering

CEP carrier-envelope phase

CID collision induced dissociation

CPA chirped pulse amplification

cw continuous wave

EA evolutionary algorithm

FROG frequency-resolved optical gating

FWHM full width at half maximum

FWM four-wave mixing

GD group delay

GDD group delay dispersion

IP ionization potential

ITO indium tin oxide

IVR intramolecular vibrational energy redistribution

LC liquid crystal

LC-SLM liquid crystal-spatial light modulator

LID laser induced decomposition

MEMS micro-electromechanical system

NIR near infrared

OCT optimal control theory

PG-FROG polarization gate frequency-resolved optical gating

RF radio frequency

SD-FROG	self-diffraction frequency-resolved optical gating
SHG	second harmonic generation
SLM	spatial light modulator
SPIDER	spectral phase interferometry for direct electric-field reconstruction
TG	transient grating
TG-FROG	transient-grating frequency-resolved optical gating
TG-XFROG	transient-grating cross-correlation frequency-resolved optical gating
THG-FROG	third harmonic generation frequency-resolved optical gating
Ti:Sa	titanium-doped sapphire, $\text{Ti}:(\text{Al}_2\text{O}_3)$
TOD	third order dispersion
UV	ultraviolet
VDE	vertical electron detachment energy
VIS	visible
XFROG	cross-correlation frequency-resolved optical gating
YAG	yttrium aluminum garnet
YLF	yttrium lithium fluoride
DFT	density functional theory

Introduction

1

Since the invention of the laser by Theodore Maiman in 1960 [1], it has been a dream for many scientists to use it for the control of chemical reactions. In the early days, the monochromatic nature of continuous wave (cw) lasers seemed to be an attractive tool for the selective excitation of vibrational modes and breaking of the corresponding chemical bonds. However, this early approach, called mode selective chemistry, is severely challenged by ultrafast intramolecular vibrational energy redistribution (IVR), which rapidly spreads the energy pumped into the molecule over many vibrational modes [2, 3, 4, 5]. As a consequence, the use of ultrafast laser pulses for achieving chemical selectivity was proposed by Bloembergen and Zewail [5]. In 1985 Tannor and Rice proposed the pump-dump control scheme as a method for attaining selectivity in the dissociation of molecules. In this scheme, a reactant molecule ABC is excited by a pump pulse to a superposition of several vibronic eigenstates, in order to prepare a wavepacket which propagates on the potential energy surface of an excited electronic state. After a temporal delay, a second laser pulse is employed to dump the molecule back into the electronic ground state by means of stimulated emission, where it may dissociate into the product channels A+BC or AB+C [6, 7]. Another approach to coherent control was developed by Brumer and Shapiro. In the Brumer-Shapiro scheme, control over the product distribution is achieved by means of quantum interference of multiple coherent paths which connect initial and final states. The molecule is excited to two or more different intermediate states and after a second photoexcitation, the probability amplitudes in the product channels obtained from the different paths interfere. Control over the yield in the product channels is achieved by altering sign and magnitude of the interference terms [8, 9]. In early experiments, pump-probe schemes were applied as a simplistic experimental technique for quantum control [10, 11, 12]. This approach was further advanced by chirping of the pump and probe pulses [13, 14]. While during the 1980s experiments incorporating ultrafast laser pulses were mostly relying on dye lasers, the invention of chirped pulse amplification by Strickland and Mourou, the introduction of titanium-doped sapphire (Ti:Sa) as a gain medium for ultrashort laser pulses by Moulton and the development of self-modelocked oscillators by Sibbet et al. led to the widespread availability of commercial high power ultrafast laser systems [15, 16, 17, 18]. In 1990 programmable pulse shapers were introduced by Weiner et al., opening up a straightforward route to arbitrarily shaped pulses [19]. In the following, Judson and Rabitz suggested a method for designing optimal laser pulses to control the dynamics of molecules, by creating a closed feedback loop experimental setup consisting of a laser and a pulse shaping device, a sample of molecules, a device for measuring the products and a computer that runs a learning algorithm which adapts the pulse shapes for maximizing the yield of the desired reaction product [20]. In this way, the lack of knowledge about the intricate molecular excited electronic states and the lack of sufficient processing power for the design of optimal laser fields could be circumvented. The first successful implementation of this scheme was performed by Bardeen et al. in 1997 for the optimal

population transfer from the ground to the first excited state of the laser dye molecule IR125 [21]. Adaptive feedback loops have since then been effectively applied in numerous coherent control experiments, for instance in the enhancement or suppression of the photodissociation of organometallic molecules, the quantum control of energy flow in a light harvesting antenna complex and the photoionization of potassium dimers with polarization-shaped pulses [22, 23, 24, 25, 26, 27].

The means for quantum control are steadily enhanced by the development of improved ultrafast laser technology, such as ultrabroadband light sources providing few-cycle pulses with carrier-envelope phase (CEP) stabilization, very high power lasers, attosecond pulses and devices for shaping ultraviolet (UV) laser pulses [28, 29, 30, 31, 32, 33]. Using CEP stabilized few-cycle pulses, Kling et al. realized the control of electron localization in molecular dissociation, demonstrating the coherent control of reaction dynamics at the attosecond time scale [34, 35]. By shaping and post-amplification of 150 fs input pulses, Weinacht et al. achieved the preparation of electronic wavepackets made up from Rydberg states, and recently Calegari et al. initiated and observed electronic wavepackets consisting of electrons in the outer-valence molecular orbitals with attosecond pulses [36, 37, 38]. Raising the intensity into the strong-field regime improves the chances to achieve resonance by means of Stark-shifting of the electronic energy levels [39, 40, 41, 42]. Most biomolecules absorb mainly in the UV, which stimulated the development of devices for shaping UV laser pulses that have been successfully employed for the discrimination of nearly identical flavins [43, 44].

This work strives to contribute to the numerous efforts in the development of faster, more accurate and more versatile supercontinuum light sources, by the development of a laser setup which enables the generation of near-arbitrarily shaped white-light pulses with few-cycle temporal resolution [45]. The new laser setup builds on the white-light generation and shaping setup developed by Schmidt et al., which relies on filamentation for supercontinuum generation [46, 47, 48]. The newly developed white-light laser setup is employed in the optimal control of the fragmentation during charge reversal of two small metal cluster anions, the copper trimer and the aluminum tetramer. In chapter 2, the fundamentals of ultrashort laser pulse generation, shaping and characterization, supercontinuum generation and optimal control are outlined. The white-light laser setup is described and characterized in chapter 3, where numerous examples of shaped supercontinuum pulses are displayed and the limits of the shaping setup are analyzed. In chapter 5, the integrated optimal control setup, incorporating the laser setup, a vacuum apparatus that provides the sample molecules and a computer running the evolutionary algorithm (EA) for optimizing the pulse shapes, is described. The integrated coherent control setup is shown to have a temporal resolution of at least 400 as and is tested for artifacts. For efficient laser pulse optimizations, a novel phase parametrization for the generation of near-arbitrary laser pulses, that respects the limitations of the pulse shaping device, is introduced. The vacuum apparatus providing the sample molecules, incorporating a magnetron sputtering source, a tandem mass spectrometer and a radio frequency (RF) ion trap is described in chapter 4. In chapters 6 and 7 the results of the experiments performed on the charge reversal and fragmentation of Cu_3^- anions and Al_4^- anions are presented.

Fundamentals

2

2.1 Ultrashort Laser Pulses

2.1.1 Time Domain Description

Light pulses are formed by superposition of electromagnetic waves with different frequencies. It is therefore advantageous to describe ultrashort laser pulses in the frequency domain. However, for the introduction of some basic concepts, a description in the time domain shall be given first. The formalism employed in this work follows Wollenhaupt et al. [49].

For a linearly polarized light pulse the real electric field $E(t)$ can be written as the product of the temporal envelope $A(t)$, given in V/cm, and a harmonic wave of the angular frequency ω_0 :

$$E(t) = A(t)\cos(\omega_0 t + \Phi_0). \quad (2.1)$$

The angular frequency ω_0 is related to the light frequency ν_0 by

$$\omega_0 = 2\pi \nu_0. \quad (2.2)$$

Φ_0 determines the temporal relation of the envelope with respect to its carrier wave and is usually referred to as the carrier-envelope phase (CEP) or absolute phase. For few-cycle pulses, pulses that contain only a few optical cycles, the CEP has significant impact on the waveform of the electric field. The CEP can be controlled [28] and is of great importance for the generation of attosecond pulses [29, 31] and other applications in attosecond science, such as the precise control of electronic wavepackets [29, 34]. However, if the temporal envelope $A(t)$ does not vary considerably during one carrier oscillation period T , the carrier-envelope phase is of little interest for most applications. For an arbitrary pulse, the electric field's frequency may change over time. This is taken into account by adding a time-dependent term $\Phi_a(t)$ to the temporal phase term in Eq. 2.1 according to:

$$\Phi(t) = \omega_0 t + \Phi_0 + \Phi_a(t). \quad (2.3)$$

The temporal derivative of the phase $\Phi(t)$ yields the time dependent instantaneous angular frequency

$$\omega(t) = \frac{d\Phi(t)}{dt} = \omega_0 + \frac{d\Phi_a(t)}{dt}. \quad (2.4)$$

The temporal intensity in W/cm² is given by

$$I(t) = \frac{1}{2}nc\varepsilon_0 A(t)^2, \quad (2.5)$$

where n denotes the refractive index, c the speed of light and ε_0 the vacuum permittivity. The pulse duration Δt is commonly defined as the full width at half maximum (FWHM) of the temporal intensity function $I(t)$.

2.1.2 Frequency Domain Description

In the regime of linear optics, i.e. when the intensity is low enough so that nonlinear effects can be neglected, the superposition principle holds. Thus, the real-valued electric field $E(t)$ can be decomposed into plane monochromatic waves by means of a Fourier transformation

$$E(t) = \frac{1}{2\pi} \int_{-\infty}^{\infty} \tilde{E}(\omega) e^{i\omega t} d\omega = \mathcal{F}^{-1}[\tilde{E}(\omega)]. \quad (2.6)$$

Here, the transformation from frequency domain to time domain is called the inverse Fourier transformation denoted by \mathcal{F}^{-1} . The frequency domain representation, called the complex spectrum $\tilde{E}(\omega)$ of $E(t)$, which contains the amplitudes and phases of all frequencies, is obtained by applying the Fourier transformation

$$\tilde{E}(\omega) = \int_{-\infty}^{\infty} E(t) e^{-i\omega t} dt = \mathcal{F}[E(t)]. \quad (2.7)$$

As $E(t)$ is a real quantity it is true that

$$\tilde{E}(\omega) = \tilde{E}^*(-\omega) \quad (2.8)$$

where the notation $(*)$ indicates the complex conjugate. This means that the negative frequency components of the complex spectrum $\tilde{E}(\omega)$ are superfluous and can be omitted without loss of information. To fully characterize the light field, the positive frequency components of the spectrum are sufficient. Hence it is practical to define the positive part of the spectrum,

$$\tilde{E}^+(\omega) = \begin{cases} \tilde{E}(\omega) & \text{for } \omega \geq 0 \\ 0 & \text{for } \omega < 0 \end{cases} \quad (2.9)$$

and the negative part of the spectrum,

$$\tilde{E}^-(\omega) = \begin{cases} \tilde{E}(\omega) & \text{for } \omega < 0 \\ 0 & \text{for } \omega \geq 0. \end{cases} \quad (2.10)$$

Summing up each renders the entire complex spectrum,

$$\tilde{E}(\omega) = \tilde{E}^-(\omega) + \tilde{E}^+(\omega). \quad (2.11)$$

$\tilde{E}^+(\omega)$, $\tilde{E}^-(\omega)$ and their Fourier pairs, the so called analytic signal $E^+(t)$ and its complex conjugate $E^-(t)$, are related by

$$E^\pm(t) = \mathcal{F}^{-1} [\tilde{E}^\pm(\omega)] \quad (2.12)$$

and

$$\tilde{E}^\pm(\omega) = \mathcal{F} [E^\pm(t)]. \quad (2.13)$$

Like any complex number, the positive part of the complex spectrum can be denoted in the polar form as the product of the spectral amplitude $|\tilde{E}^+(\omega)|$ and a phase factor $e^{-i\phi(\omega)}$:

$$\begin{aligned}\tilde{E}^+(\omega) &= |\tilde{E}^+(\omega)| e^{-i\phi(\omega)} \\ &= \sqrt{\frac{\pi}{\epsilon_0 c n}} \sqrt{I(\omega)} e^{-i\phi(\omega)}.\end{aligned}\quad (2.14)$$

$\phi(\omega)$ is called spectral phase and $I(\omega)$ is the spectral intensity which can be measured with a spectrometer. Devices fast enough to control the electric field in the time domain are nonexistent. Hence, in the experiment, controlling spectral phase and spectral amplitude is the common approach for manipulating the electric field in the time domain by means of the Fourier transformation, Eq. (2.12). The relationship between time and frequency domain can clearly be seen in the derivative of the respective phase factor. In the time domain the time derivative of the phase yields the instantaneous frequency $\omega(t)$ (Eq. (2.4)), while the frequency derivative of the spectral phase $\phi(\omega)$ yields the relative temporal delay of each frequency component, called the group delay $\text{GD}(\omega)$:

$$\text{GD}(\omega) = \frac{d\phi(\omega)}{d\omega} \quad (2.15)$$

The derivative of the group delay, or the second derivative of the spectral phase, is called group delay dispersion (GDD):

$$\text{GDD}(\omega) = \frac{d\text{GD}(\omega)}{d\omega} = \frac{d^2\phi(\omega)}{d\omega^2} \quad (2.16)$$

The derivative of the GDD, or the third derivative of the spectral phase, is called third order dispersion (TOD):

$$\text{TOD}(\omega) = \frac{d\text{GDD}(\omega)}{d\omega} = \frac{d^3\phi(\omega)}{d\omega^3} \quad (2.17)$$

It should be noted, that despite its name ‘third order dispersion’, this term also contains the dispersion of higher orders. To gain insight into the effects of the spectral phase function, it can be expanded into a Taylor series around the pulse’s central frequency ω_0 :

$$\begin{aligned}\phi(\omega) &= \sum_{j=0}^{\infty} \frac{\phi^{(j)}(\omega_0)}{j!} \cdot (\omega - \omega_0)^j \\ &= \phi(\omega_0) + \phi'(\omega_0) \cdot (\omega - \omega_0) + \frac{1}{2}\phi''(\omega_0) \cdot (\omega - \omega_0)^2 \\ &\quad + \frac{1}{6}\phi'''(\omega_0) \cdot (\omega - \omega_0)^3 + \dots\end{aligned}\quad (2.18)$$

The zeroth-order coefficient $\phi(\omega_0)$ is, except for the sign, equal to the CEP in the time domain: $\phi(\omega_0) = -\Phi_0$. The first order coefficient $\phi'(\omega_0)$ shifts the pulse in time without altering the waveform, an effect referred to as Fourier-shift. A positive $\phi'(\omega_0)$ shifts the pulse to later times. This is quite obvious, as during a time t every frequency component ω accumulates the phase $\phi(\omega) = \omega t$, which is a linear function in ω . The second order

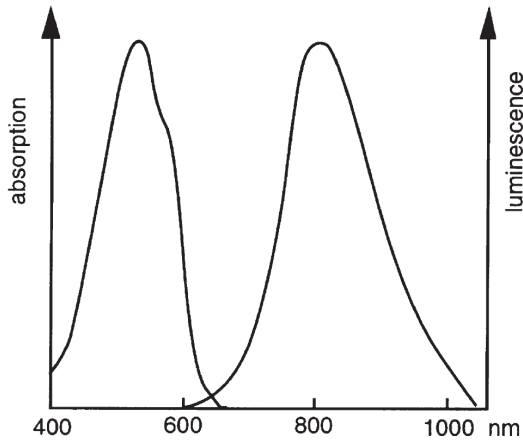


Figure 2.1: Absorption and emission spectrum of titanium-doped sapphire. Image taken from [50].

term causes a linear group delay, or linear chirp, which means that the instantaneous frequency of the pulse increases or decreases linearly in time. For a positive $\phi''(\omega_0)$ the higher frequencies arrive at later times, an effect associated with normal dispersion. The third order coefficient $\phi'''(\omega_0)$ causes a quadratic GD, or quadratic chirp, and a single-sided pulse train. The single-sided pulse train is the beating pattern of the high-frequency and low frequency tail (for $\phi'''(\omega_0) > 0$) of the pulse. For a constant or linear spectral phase $\phi(\omega)$, a laser pulse assumes its shortest possible duration for a given spectrum $I(\omega)$. Such a pulse is termed (Fourier) transform limited. The minimum duration is limited by the time-bandwidth product $\Delta t \Delta \nu$ with the FWHM bandwidth $\Delta \nu$. For a Gaussian-shaped spectrum $I(\omega)$ holds

$$\Delta t \Delta \nu \geq \frac{2 \ln 2}{\pi} \approx 0.441. \quad (2.19)$$

Hence, the minimum duration Δt of a laser pulse is inversely proportional to its bandwidth $\Delta \nu$. As a picture is worth a thousand words, some simulated ultrabroadband laser pulses are shown in section 2.4.2, to illustrate the effects of $\phi'(\omega_0)$ (see Fig. 2.11), $\phi''(\omega_0)$ (see Fig. 2.12) and $\phi'''(\omega_0)$ (see Fig. 2.13).

2.2 Generation of Ultrashort Laser Pulses

2.2.1 Mode Locked Femtosecond Oscillators

In order to obtain a short pulse, a broad spectrum with a constant or linear phase relation of the spectral components is needed. Usually the spectrum is generated by optical pumping of a laser medium with a broad emission spectrum. In most modern fs-oscillators the pump laser generating the population inversion is a green cw laser and the active medium is titanium-doped sapphire $\text{Ti}:(\text{Al}_2\text{O}_3)$ commonly referred to as Ti:Sa. Operation of a Ti:Sa laser was first reported by P. F. Moulton in 1982 [16]. Ti:Sa absorbs green light and has a very broad emission spectrum centered at 800 nm, as shown in Fig. 2.1. The Ti:Sa medium is placed inside a laser cavity with length L and a cavity

round-trip time of

$$T_{RT} = \frac{2L}{c}. \quad (2.20)$$

Inside the cavity only longitudinal modes with a frequency spacing

$$\delta\nu = \nu_{n+1} - \nu_n = \frac{c}{2L} = \frac{1}{T_{RT}} \quad (2.21)$$

are allowed. The electric field $E(t)$ resulting from the superposition of all N lasing modes ν_n at a fixed point in space is

$$E(t) = \sum_{n=0}^{N-1} E_n \sin(2\pi(\nu_0 + n\delta\nu)t + \phi_n(t)), \quad (2.22)$$

where ν_0 is the lowest frequency lasing mode. If there is no mechanism employed for locking the phases $\phi_n(t)$ of the modes ν_n , the relative phases will vary randomly in time. The radiation energy in the cavity will spread uniformly over the whole length of the cavity and the radiation energy will concentrate in a relatively small number of modes having the highest gain. The emission spectrum reflecting the gain coefficient is depicted in Fig. 2.1. In consequence, these modes will also interfere randomly in time, leading to a random output power $P(t)$. If the relative phases are random but do not vary over time, the resulting electric field $E(t)$ will repeat itself with the period T_{RT} , which is illustrated in Fig. 2.2 (a). A mode locked laser meets the mode locking condition

$$\phi_n = n\alpha. \quad (2.23)$$

For a simplified analysis of this case, the amplitudes $E_n = E_0$ of all modes are defined to be equal, which corresponds to a square gain profile, and α is set to zero. The resulting electric field is

$$E(t) = E_0 \sin(2\pi(\nu_0 + \frac{N-1}{2}\delta\nu)t) \frac{\sin(N\pi\delta\nu t)}{\sin(\pi\delta\nu t)}. \quad (2.24)$$

The term $\nu_c = \nu_0 + \frac{N-1}{2}\delta\nu$ gives the central frequency of the laser output and $|\frac{\sin(N\pi\delta\nu t)}{\sin(\pi\delta\nu t)}|$ is the envelope oscillating with $\delta\nu = \frac{1}{T_{RT}}$. Averaging the fast carrier oscillations of ν_c yields the output power

$$P(t) = P_0 \left[\frac{\sin(N\pi\delta\nu t)}{\sin(\pi\delta\nu t)} \right]^2 \quad (2.25)$$

with the average power of one mode P_0 .

From this equation it can be seen that for a large number of modes the peak output power increases quadratically with the number of locked modes. As the bandwidth $\delta\nu$ increases linearly with the number N of modes, according to the time bandwidth product Eq.(2.19), the FWHM pulse duration is inversely proportional to the number of locked modes:

$$\Delta t = \frac{1}{N\delta\nu} = \frac{1}{\Delta\nu}. \quad (2.26)$$

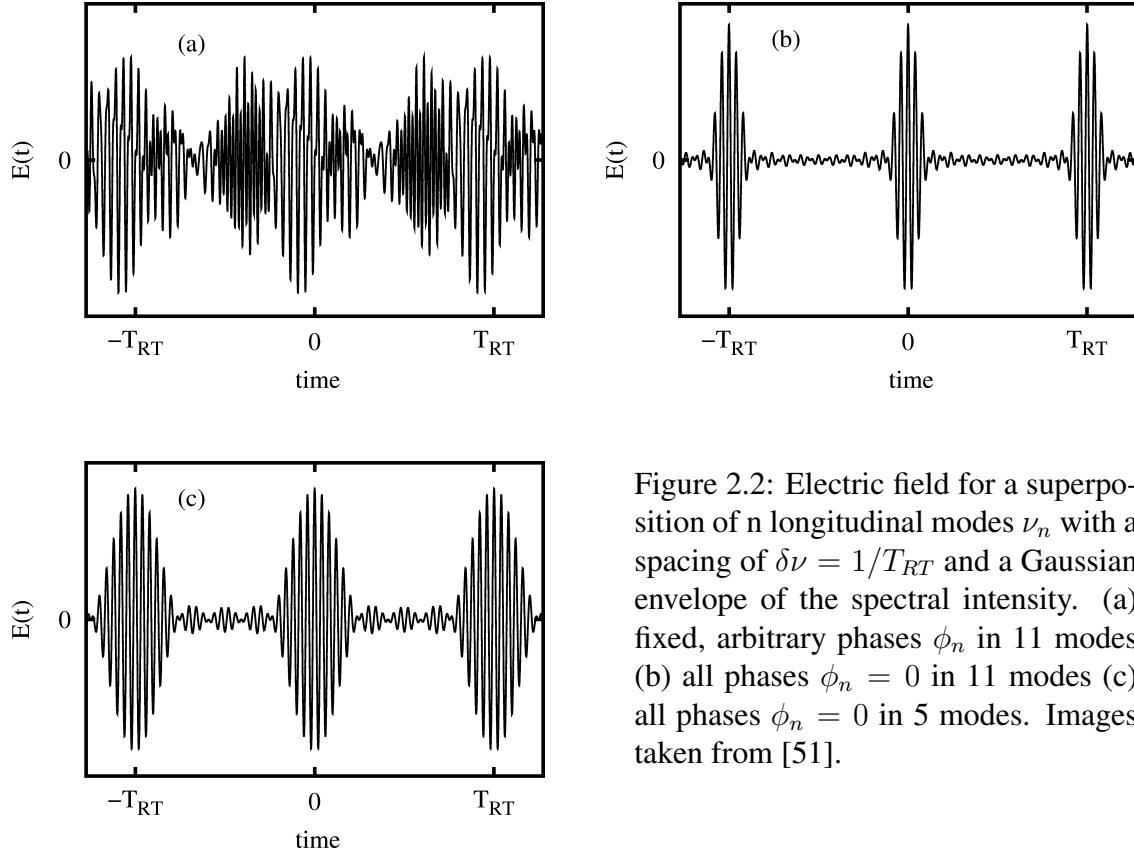


Figure 2.2: Electric field for a superposition of n longitudinal modes ν_n with a spacing of $\delta\nu = 1/T_{RT}$ and a Gaussian envelope of the spectral intensity. (a) fixed, arbitrary phases ϕ_n in 11 modes (b) all phases $\phi_n = 0$ in 11 modes (c) all phases $\phi_n = 0$ in 5 modes. Images taken from [51].

The electric field of 11 and 5 locked modes is shown in Fig. 2.2 (b) and (c), respectively. The electric field in Fig. 2.2 (a) results from 11 modes with arbitrary but fixed phases. Modern oscillators achieve the locking of the longitudinal modes passively by means of the optical Kerr effect, or self-focusing, discussed in section 2.3.2. This method is called Kerr lens mode locking and will be described in the following.

To start the locking process, a finite number of modes have to be lasing. Then a short perturbation is introduced, such that the radiation energy is no longer distributed uniformly over the entire cavity. This can be achieved, for example, by moving one of the end mirrors of the cavity, leading to short bursts of above average intensity that propagate through the cavity and show enhanced self-focusing in the active medium. These bursts of elevated intensity can be favored by placing an aperture with proper diameter behind the Ti:Sa medium, increasing the loss for average power radiation and allowing a higher throughput for self-focused bursts. A more efficient method is to make use of the pump beam as an aperture, by reducing its diameter to less than the beam waist during cw operation. Hence, the self-focused bursts will see more inversion caused by the pump beam than the unfocused cw radiation of which a smaller fraction overlaps with the pump beam. Thus, bursts will receive more gain than cw radiation. Meanwhile, a burst traveling around the cavity at the frequency $\delta\nu$ will cause a periodic change of the refractive index of the Ti:Sa medium at the frequency $\delta\nu$. This leads to a periodic phase modulation of the modes already lasing, generating sidebands with frequencies $\nu_s = \nu_n \pm \delta\nu$ which are consistent with the frequencies of the longitudinal modes defined by the length of the cavity. In this manner, bursts broaden the spectrum. Finally,

the most intense burst will prevail in depleting the inversion over all other radiation, thus picking up all the energy from the gain medium. Hence, by designing the laser cavity in a way that favors highest intensity, it locks the phases of all modes according to the mode locking condition, as this is the phase relation producing the highest intensity.

As a pulse broadens due to dispersion when propagating around the cavity, some dispersion compensation has to be employed to keep the pulse short. This can be achieved by the use of prisms or chirped mirrors [52]. Ti:Sa oscillators output pulses with energies of several nJ at repetition rates around of $8 \cdot 10^7$ Hz with pulse durations from 80 fs down to below 6 fs [53].

2.2.2 Chirped Pulse Amplification

Virtually all high power ultrafast laser systems utilize a method called chirped pulse amplification (CPA) [15] to amplify pulses obtained from a fs-oscillator. In this scheme, the seed pulse from the fs-oscillator is strongly chirped and hence elongated by passing it through a stretcher [54], to keep the intensity of the amplified pulse below the damage threshold of the gain medium and to prevent self-focusing. Population inversion is achieved by optical pumping of the gain medium. In most cases Ti:Sa is used, which is pumped by a frequency-doubled YAG or YLF laser. The seed pulse is amplified during several passes through the gain medium. After amplification the pulse is recompressed by means of a grating compressor [15]. A scheme of a chirped pulse amplification setup is depicted in Fig. 2.3. The stretching factor typically is on the order of 1000 and the amplification factor can reach 50 per pass of the gain medium. The total amplification factor ranges from about 10^3 for high repetition rate systems to about 10^9 for high energy systems with several amplification stages. The Quantronix Odin C amplifier used in the context of this work achieves an amplification factor of $\approx 3 \cdot 10^5$ in 8 passes of the Ti:Sa medium at a 1kHz repetition rate. In most amplifiers, only a small fraction of the seed pulses generated by the oscillator are amplified, as amplification at a 80 MHz repetition rate would require excessive pumping power. This is achieved by picking for example 10 or 1000 pulses per second by means of a Pockels cell [55] before the seed beam enters the amplifier.

2.2.3 Pulse Shaping

The generation of tailored laser pulses with pulse shaping techniques is a powerful tool in coherent control (see section 2.5). Pulse shaping devices may as well be employed for the generation of few-cycle and monocycle pulses [56, 57, 58, 59, 60]. As described in section 2.1.2, the shape of a laser pulse depends on its spectral intensity $I(\omega)$ and its spectral phase $\phi(\omega)$. Control of spectral phase and spectral intensity can be achieved by means of liquid crystal-spatial light modulators (LC-SLMs) [19, 61] and acousto-optic modulators (AOMs) [62] placed in the Fourier plane of a 4-f setup as depicted in Fig. 2.7. LC-SLMs rely on the adjustable refractive index of liquid crystals (LCs) to manipulate

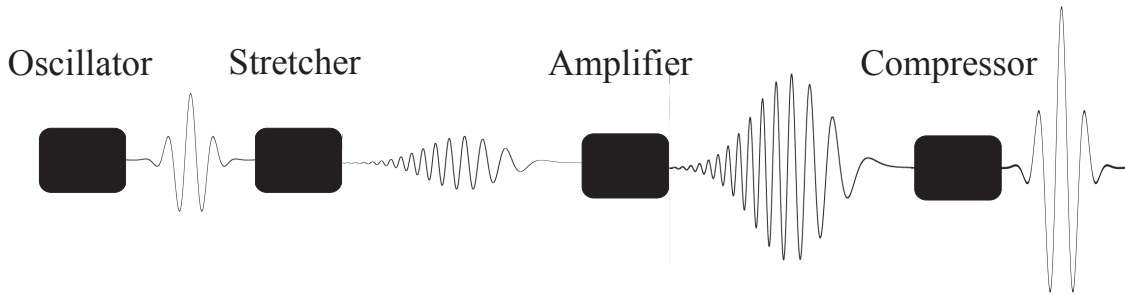


Figure 2.3: Chirped pulse amplification scheme. Femtosecond pulses are obtained from a fs-oscillator and are stretched by means of a stretcher by a factor of about 1000 for safe amplification. In the amplifier, the pulses are amplified by a factor of up to 10^9 and are subsequently recompressed by means of a compressor. Image from [51].

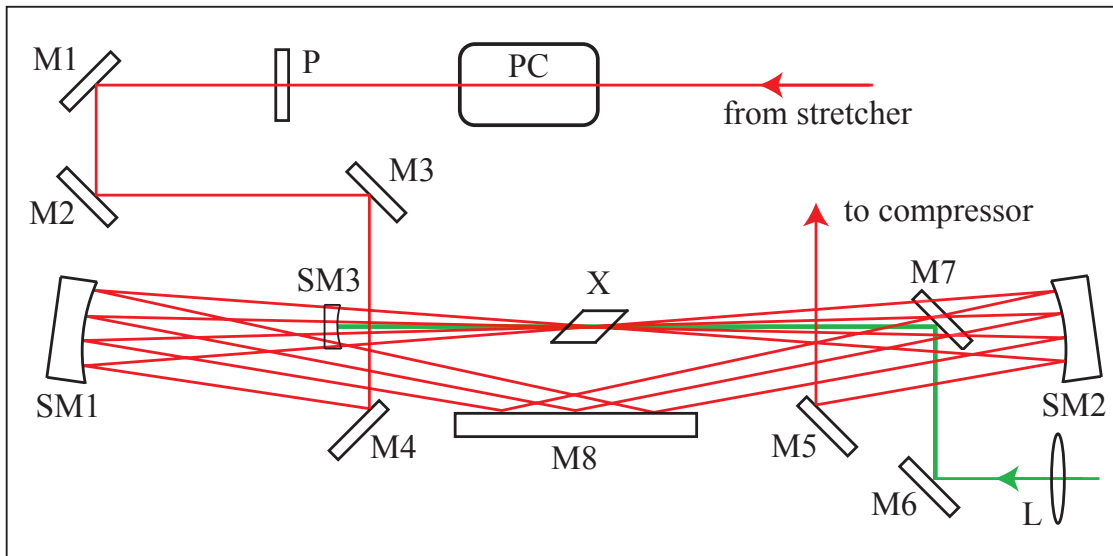


Figure 2.4: Scheme of a multipass amplifier. The input beam (red) coming from the stretcher passes through a Pockels cell (PC) that turns the polarization of the pulses to be amplified by 90° . The polarizer (P) erases all pulses of which the polarization has not been turned by the Pockels cell. Thereafter the remaining seed pulses are fed into the amplifier. The spherical mirror SM1 focuses the beam into the Ti:Sa crystal X where the amplification takes place. Then the divergent beam is recollimated by the spherical mirror SM2. Via the flat mirror M8 the beam is guided back to the spherical mirror SM1 for the next pass of the active medium. Here, after four passes of the Ti:Sa crystal, the beam hits the flat mirror M5 which steers it to the compressor. The pump beam (green) is focused by the lens L and is steered into the active medium by the flat mirror M7 at a slightly rising beam path. After the first passage of the active medium the beam is refocused for a second pass of the Ti:Sa crystal by the spherical mirror SM3. M7 is placed below the red beams, SM3 is placed above them. M1-8 are flat mirrors. Image taken from [51].

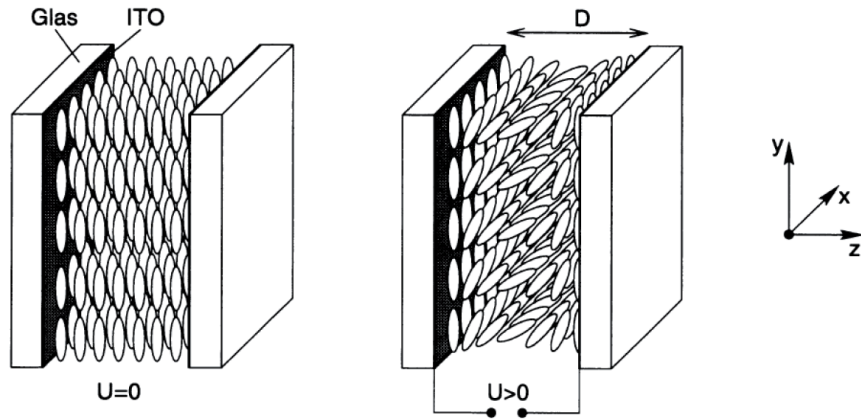


Figure 2.5: Cross section of a LC cell. left: The elongated molecules forming the LC are embedded between glass windows. The inner sides of the windows are coated with indium tin oxide (ITO), which acts as a transparent electrode. To align the molecules, the insides of the windows are brushed. right: A nonzero voltage is applied to the ITO electrodes, tilting the molecules and thereby reducing the refractive index along the slow axis of the LC. Image taken from [66].

the relative phase and polarization of different frequencies. By adding a subsequent polarizer, the polarization control can be translated into amplitude shaping. AOMs diffract light by means of a programmable radio-frequency acoustic wave propagating through a transparent material. Micromirror spatial light modulators (SLMs) [63] and deformable mirrors [64] can be employed in a reflective 4-f setup for shaping high power pulses and UV pulses. Without the need for a 4-f setup, acousto-optic programmable dispersive filters (AOPDFs) [65], also known as Dazzler (Fastlite), achieve phase and amplitude shaping due to longitudinal interaction of a polychromatic acoustic wave with the laser pulse. All these techniques have advantages and downsides. LC-SLMs are capable of implementing highly complex spectral phase and amplitude functions and they have a high light transmission. Even LC-SLMs usable in the UV down to 260 nm, thanks to a mixture of cyclohexane derivatives with fluorine substituents as LC, have recently been developed [32]. On the other hand, LC-SLMs have a limited (though not terribly low) power handling capability and a slow response time. Their pixels limit the steepness of spectral phase functions and cause satellite pulses. AOMs are not pixelated, but their optical transmission is below 50 % and they are unusable for shaping typical fs-oscillators with repetition rates around 80 MHz [49]. AOPDFs require no additional optical components, but their transmission is 50 % at best. In the following, only pulse shaping by means of LC-SLMs will be described in detail.

LC-SLMs are LC cells embedded between glass windows, with pixelated arrays of transparent electrodes made of indium tin oxide (ITO) applied as a coating to the insides of the windows. A LC cell is shown in Fig. 2.5. The insides of the windows are brushed, leaving tiny grooves to orient the elongated molecules forming the birefringent liquid crystal. The orientation of the elongated molecules defines the axis of extraordinary refractive index $n_e(V, \omega)$ of the LC, which can be adjusted by applying a nonzero voltage

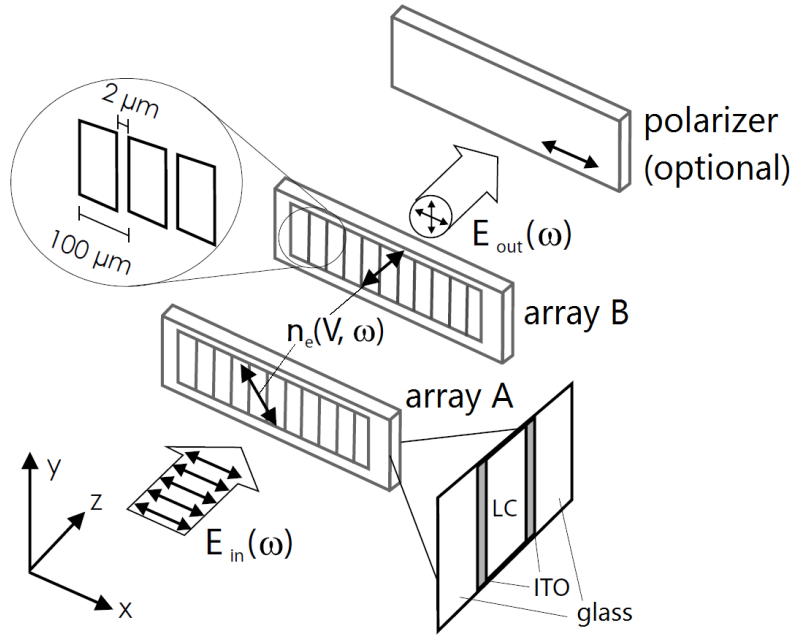


Figure 2.6: Structure of a double array LC-SLM. The incoming light $E_{in}(\omega)$ should be horizontally polarized. The axes of voltage-adjustable refractive index $n_e(V, \omega)$ in the two LC arrays (array A and array B) are orthogonally oriented at $\pm 45^\circ$. For amplitude shaping, the polarization of the outgoing light $E_{out}(\omega)$ is rotated and attenuated by a polarizer. For phase-only shaping, the polarizer may be omitted. The LC-SLM employed in this work has a pixel pitch of $100 \mu\text{m}$ and interpixel gaps of $2 \mu\text{m}$. Image adapted from [67].

to the transparent electrodes. The electric field tilts the elongated molecules, lowering the refractive index along the (former) axis of extraordinary refractive index. For phase and amplitude shaping, double array LC-SLMs as shown in Fig. 2.6 are used, featuring two arrays, dubbed A and B, where the axes of extraordinary refractive index are crossed and oriented at $\pm 45^\circ$ with respect to the polarization of the incoming light. In this way, the two arrays can be employed to rotate the polarization by setting different extraordinary refractive indices $n_e(V, \omega)$ in the two arrays. For example if $n_e(V, \omega)$ in one array is chosen such that it retards the incoming light wave by $\lambda/2$ less than the other array, the LC-SLM acts like a half-wave-plate, rotating the polarization by 90° . Hence, a double-array LC-SLM can be employed for phase shaping and either polarization shaping or amplitude shaping, by adding a subsequent polarizer.

Of course, every frequency component has to be addressed individually. For this, the LC-SLM is placed in the Fourier plane of a so-called 4- f line as depicted in Fig. 2.7 which works as follows. The incident beam is spectrally dispersed by a diffraction grating. A cylindrical lens with focal length f is placed at distance f from the grating, to parallelize the different frequency components and to focus each frequency component. The foci of all frequency components form the Fourier plane. A second cylindrical lens, also with the focal length f , is placed in at distance f behind the Fourier plane, to recollimate each frequency component and to refocus the spectrum onto the second grating. The second grating is placed at distance f from the second cylindrical lens and recollimates

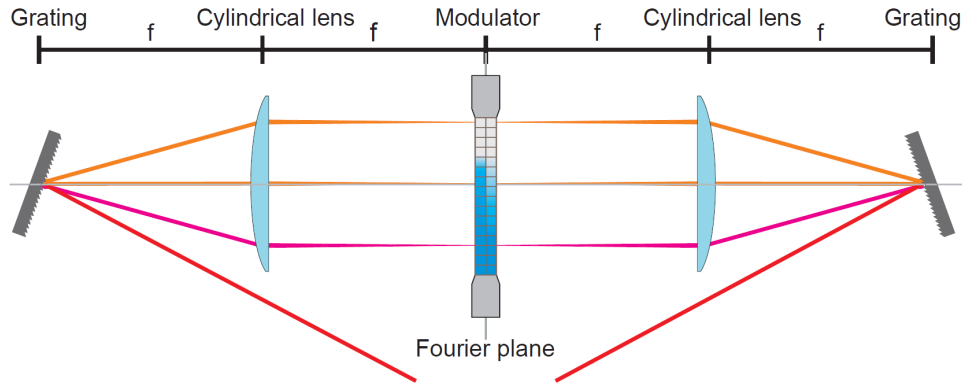


Figure 2.7: 4- f pulse shaper setup with an LC-SLM placed in the Fourier plane. The incoming beam is dispersed by a grating. A cylindrical lens with the focal length f is placed at distance f from the grating, to parallelize the different wavelengths and to focus each wavelength in the Fourier plane, which is located at distance f from the cylindrical lens. The second cylindrical lens recollimates each wavelength and focuses all wavelengths onto the second grating, where the beam is recollimated. Image taken from [67].

the beam. For broadband laser pulses, chromatic aberrations and material dispersion in the lenses cause problems. To avoid these, the lenses are replaced by cylindrical mirrors. For this, the linear setup employing lenses is converted into a ‘folded’ reflective setup. An optimized reflective setup is presented in [68].

In the LC-SLM, the difference of the voltage-adjustable extraordinary refractive index $n_e(V, \omega)$ and the ordinary refractive index $n_o(\omega)$ causes a phase retardation $\Delta\phi(V, \omega)$ of the extraordinary ray with respect to the ordinary ray. For x -polarized light incident on a particular pixel of the double-array LC-SLM, the outgoing electric field E_{out} is given by [61]

$$E_{out} = E_{in} \exp \left[\frac{\Delta\phi^A + \Delta\phi^B}{2} \right] \cdot \left[\hat{\mathbf{e}}_x \cos \left(\frac{\Delta\phi^A - \Delta\phi^B}{2} \right) + i \hat{\mathbf{e}}_y \sin \left(\frac{\Delta\phi^A - \Delta\phi^B}{2} \right) \right] \quad (2.27)$$

with the unit vectors $\hat{\mathbf{e}}_x$ and $\hat{\mathbf{e}}_y$ in x and y direction, and the respective voltage dependent phase retardations $\Delta\phi^A$ and $\Delta\phi^B$ in array A and array B . Hence, without a subsequent polarizer, an LC-SLM can be used for phase and polarization shaping. When a subsequent polarizer oriented in x -direction is added, the outgoing electric field becomes

$$E_{out} = E_{in} \exp \left[\frac{\Delta\phi^A + \Delta\phi^B}{2} \right] \left[\hat{\mathbf{e}}_x \cos \left(\frac{\Delta\phi^A - \Delta\phi^B}{2} \right) \right]. \quad (2.28)$$

In this way, the LC-SLM is employed for phase and amplitude shaping. From the above equation it is apparent that the relative additional phase ϕ_a imposed by the LC-SLM is

$$\phi_a = \frac{\Delta\phi^A + \Delta\phi^B}{2}, \quad (2.29)$$

and that the transmission T through the postponed polarizer is

$$T = \cos^2 \left(\frac{\Delta\phi^A - \Delta\phi^B}{2} \right). \quad (2.30)$$

The phase retardations for a given additional phase ϕ_a and transmission T are given by

$$\Delta\phi^A = \arccos(\sqrt{T}) + \phi_a \quad (2.31)$$

$$\Delta\phi^B = \phi_a - \arccos(\sqrt{T}). \quad (2.32)$$

It should be noted that negative phase retardations are physically impossible, which has to be taken into account when calculating the drive voltages for the LC-SLM [69].

Another important limitation of LC-SLMs arises from the discrete sampling of the phase function. The phase function imposed by the LC-SLM should be smooth, despite its pixelation. To fulfill this demand, it is required that the phase change $\delta\phi$ between two adjacent pixels satisfies the condition $|\delta\phi| \ll \pi$. Hence, the time τ by which a pulse can be delayed or advanced is restricted according to $\tau \ll \pi/\delta\omega$, with the difference of the angular frequencies transmitted through the center of two adjacent pixels $\delta\omega$ [70]. Due to the 2π -periodicity of the light field regarding the spectral phase, the discretized phase function applied by an LC-SLM is also ambiguous. For example a $\delta\phi = \pi/2$ can as well be interpreted as $\delta\phi = -3\pi/2$, which causes sampling replica pulses [71].

2.3 Nonlinear Optics

2.3.1 Second Harmonic Generation (SHG)

While the intensity of light passing through a medium is sufficiently low, the excursion of the loosely bound outer or valence electrons will be proportional to the force exerted on them by the electric field. In this case the polarization P inside the medium can be written in the form ([55])

$$P = \epsilon_0 \chi E, \quad (2.33)$$

with the dimensionless susceptibility χ and the vacuum permittivity ϵ_0 . However, the excursion of the electrons cannot grow infinitely as E increases. Thus, for strong electric fields, the relation of the excursion of the electrons and hence the polarization is not linear in E any more. The nonlinear polarization can be developed into a power series

$$P = \epsilon_0 (\chi^{(1)} E + \chi^{(2)} E^2 + \chi^{(3)} E^3 + \dots) \quad (2.34)$$

with the n -th order susceptibilities $\chi^{(n)}$. As the higher order susceptibilities are smaller than $\chi^{(1)}$, these terms only contribute significantly at very high intensities. If a harmonic light wave of the form

$$E = E_0 \sin \omega t \quad (2.35)$$

is incident on the medium, the resulting polarization

$$P = \epsilon_0 \chi^{(1)} E_0 \sin \omega t + \epsilon_0 \chi^{(2)} E_0^2 \sin^2 \omega t + \epsilon_0 \chi^{(3)} E_0^3 \sin^3 \omega t + \dots \quad (2.36)$$

can be transformed to

$$P = \epsilon_0 \chi^{(1)} E_0 \sin \omega t + \frac{\epsilon_0 \chi^{(2)}}{2} E_0^2 (1 - \cos 2\omega t) + \frac{\epsilon_0 \chi^{(3)}}{4} E_0^3 (3 \sin \omega t - \sin 3\omega t) + \dots \quad (2.37)$$

The second term features two interesting phenomena: First, a constant component, and second, a component oscillating at twice the frequency of the incident light, both proportional to the intensity of the incident light. The former component causes a voltage difference across a medium with nonzero $\chi^{(2)}$, an effect referred to as optical rectification. The latter component gives rise to a light wave reradiated by the polarization with twice the frequency of the incident light. This effect is called second harmonic generation (SHG).

It is noteworthy that, in an isotrope material, reversing the direction of E would reverse the direction of P as well. Hence, for a material with inversion symmetry all even terms in E in Eq. (2.34) must vanish. This is why optical rectification and SHG can be observed only in media with no inversion symmetry, like piezoelectric crystals. It has to be considered as well that, in general, light with the fundamental frequency ω and light with the second harmonic frequency do not travel with the same velocity as their refractive indices differ ($n_\omega \neq n_{2\omega}$). In consequence, two 2ω -waves generated at different points in space do not interfere coherently. Hence, efficient SHG can only be achieved if ($n_\omega = n_{2\omega}$) so that the fundamental and the 2ω -wave propagate equally fast and all generated 2ω -waves are in phase. This can be achieved by using a birefringent crystal in a suitable orientation, a method referred to as phase matching. For example a negative uniaxial crystal ($n_e < n_o$) can be oriented in such a way that the polarization of the ω -wave is parallel to the ordinary axis, resulting in phase matching for a 2ω -wave polarized along the extraordinary axis if $n_e(2\omega) = n_o(\omega)$ [50]. The material commonly used for SHG of 800 nm pulses is beta barium borate (BBO) which is negative uniaxial and transparent for wavelengths from 190 nm to 2.5 μm .

2.3.2 Intensity Dependent Refractive Index

When an intense beam propagates through an optical medium, the refractive index is no longer independent of the intensity. (In this context, “intense” means, that the mean electrostatic energy of the Field, $\frac{1}{2}\epsilon|E|^2V$, with the interaction volume V , becomes comparable to the energy of the electronic states (a few eV).) For isotropic media $\chi^{(2)}$ vanishes and the dielectric response of the medium becomes [50]:

$$\epsilon_t = \epsilon + \epsilon_2 \langle E \cdot E \rangle + \dots \quad (2.38)$$

with the time average of the squared electric field $\langle E \cdot E \rangle = \frac{1}{2}|E|^2$, $\epsilon = 1 + \chi^{(1)}$ and $\epsilon_2 = 1 + \chi^{(3)}$. The index of refraction n is given by the square root of the dielectric function

$$n = \sqrt{\epsilon_t} = \sqrt{\epsilon + \epsilon_2 \langle E \cdot E \rangle} \approx n_0 + n_2 \langle E \cdot E \rangle \quad (2.39)$$

yielding the final form

$$n = n_0 + \frac{1}{2}n_2 I \quad (2.40)$$

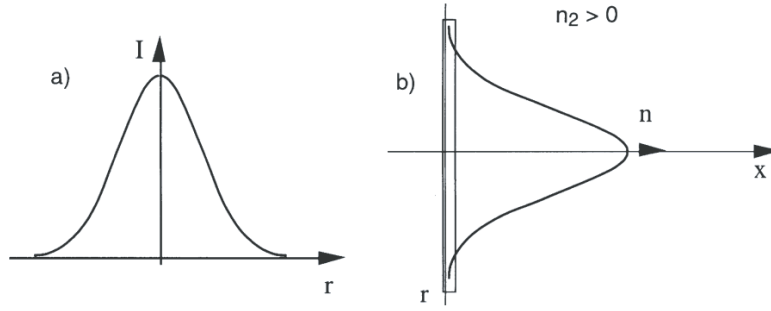


Figure 2.8: a) Intensity profile of a Gaussian beam. b) The intensity dependent refractive index n_2 of a disc of dielectric medium along the diameter of a beam traveling in x -direction. Image from [50].

with the intensity $I = |E|^2$. This change of the refractive index due to the intensity of the incident light is called the optical Kerr effect. n_0 is the fundamental refractive index of the medium measured at a low intensity. n_2 is the effective nonlinear refractive index associated with the intensity I . If a beam with a Gaussian intensity profile passes through a dielectric medium with a positive n_2 , the nonlinear refractive index has a Gaussian profile around the beam center as well:

$$n(r) = n_0 + \frac{1}{2}n_2I(r) \quad \text{with} \quad I(r) = e^{-gr^2} \quad (2.41)$$

where r denotes the distance (or radius) from the beam center. This is depicted in Fig.2.8. Thus, the center of the beam sees a higher refractive index than its outer parts. In geometrical optics the crucial quantity for the propagation of a light ray is the product of the refractive index and the traveled distance e , known as the optical path $P(r) = n(r)e$. Hence, an equivalent of the disc of dielectric medium with varying refractive index can be constructed from a disc featuring a changing thickness e and a constant refractive index:

$$P(r) = n(r)e = n_0e(r), \quad (2.42)$$

which is equivalent to a disc of the thickness

$$e(r) = \frac{n(r)e}{n_0}, \quad (2.43)$$

which is a focusing Gaussian lens. The effect of an intense beam focusing itself inside a dielectric medium is called self-focusing.

2.3.3 Filamentation

As discussed in the previous section, intense beams may self-focus, and self-focusing can lead to the filamentation of the beam, a highly nonlinear propagation induced by the collapse of the optical beam, accompanied by plasma generation, self-phase modulation, spectral broadening and other nonlinear effects. During filamentation coherence and even the carrier-envelope phase stability of the filamenting pulses are preserved, which

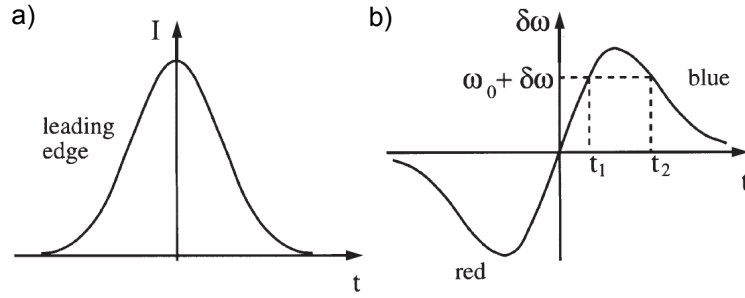


Figure 2.9: a) Temporal intensity of a Gaussian pulse. b) Frequency shift due to self-phase modulation. The frequencies are red-shifted at the leading edge of the pulse and blue shifted at the trailing edge. Image taken from [50].

makes filamentation a highly interesting tool for spectral broadening and compression of laser pulses [46, 72] as well as spectroscopic applications [73]. In 1964 Michael Hercher reported the first observation of filaments [74]. A ruby laser propagating through optical glass left visible damage tracks and the phenomenon was interpreted as self-trapping of optical beams due to self-focusing [75]. Collapse of the optical beam occurs only when self-focusing overcomes diffraction. The critical input peak power for this is [76]

$$P_{cr} = 3.72\lambda_0^2/8\pi n_0 n_2 \quad (2.44)$$

for Townes beams (beams with the radial profile calculated by Chiao et al. [75]), for which diffraction and self-focusing are balanced. For gaussian beams the coefficient 3.72 has to be replaced by 3.77. For Ti:Sa lasers ($\lambda_0 = 800$ nm) in air at atmospheric pressure, $P_{cr} = 3.2$ GW, a peak power easily achieved by commercially available laser systems. The varying intensity $I(r, t)$ of the pulse along the propagation direction causes changes in the refractive index $n = n_0 + n_2 I(r, t)$, which leads to the generation of new frequencies in the spectrum of the laser pulse, an effect called self-phase modulation (SPM). Considering that the instantaneous frequency $\omega(t)$ is the temporal derivative of the temporal phase it can be written as [50]

$$\omega(t) = -\frac{\partial}{\partial t}\Phi(t) = \omega_0 - \frac{\omega_0}{c}z\frac{\partial n(t)}{\partial t}, \quad (2.45)$$

with the propagation distance z for the frequency component ω_0 . The frequency-shift exerted on ω_0 is

$$\delta\omega(t) = \omega(t) - \omega_0 = -\frac{n_2\omega_0}{2c}z\frac{\partial I(r, t)}{\partial t}, \quad (2.46)$$

which, due to the rising intensity, leads to the generation of red-shifted frequencies at the leading edge of the pulse, and to the generation of blue-shifted frequencies at the trailing edge, due to the decreasing intensity.

Another effect caused by the varying refractive index along the propagation direction is self-steepening. The trailing part of the pulse sees a smaller refractive index than the central part, and thus moves faster, catching up with the central part of the pulse, which leads to a steepening of the trailing edge [77]. The steepening of the trailing edge in turn

enhances the blue-shifting by self-phase modulation, resulting in a mainly blue-shifted output spectrum. A pulse can also undergo asymmetric pulse splitting, as the leading part sees a smaller refractive index than the central part, which further increases in intensity at the trailing edge due to self-steepening. Hence the leading part may propagate faster and separate from the central part of the pulse [76, 78, 79].

Self-focusing of a pulse is limited by plasma generation due to multi-photon ionization and tunnel ionization. A free electron density $\rho(r, t)$ reduces the refractive index of the medium according to [76]

$$n \simeq n_0 - \frac{\rho(r, t)}{2\rho_c}, \quad (2.47)$$

with the critical plasma density $\rho_c \equiv \epsilon_0 m_e \omega_0^2 / e^2$, above which the plasma becomes opaque. As a result the beam acts like a defocusing lens when the intensity becomes sufficient to ionize the dielectric medium. During filamentation, a pulse undergoes several cycles of self-focusing and plasma-defocusing. At elevated intensities in the range of $6 P_{cr}$ or more, plasma generation leads to very strong spectral broadening, especially on the blue side [79]. In atmospheric air, filaments can persist for several tens of meters [80] or even 2 km for 200 mJ pulses [81]. A detailed description of filamentation is far beyond the scope of this work and the reader is referred to the extensive reviews by Couairon et al. [76] and Bergé et al. [79] for a thorough discourse.

2.4 Pulse Characterization

Ultrashort laser pulses are too short for a characterization with only electronic equipment and there are no mechanical gating mechanisms available that are fast enough for the task as well. Hence, ultrashort laser pulses are usually characterized by autocorrelation or different frequency-resolved optical gating (FROG) techniques.

2.4.1 Autocorrelator and SHG FROG

Autocorrelators and FROGs are usually realized by splitting the input pulse into two identical ones, one of which is variably delayed. Then both pulses k_1 and k_2 are focused into an SHG crystal and the SHG signal k_1+k_2 is recorded as a function of the delay τ . If only the intensity of the SHG signal is recorded, the apparatus constitutes an autocorrelator. The intensity of the signal recorded by an autocorrelator is [82]

$$I_{AC}(\tau) = \int_{-\infty}^{\infty} I(t)I(t - \tau)dt. \quad (2.48)$$

If the SHG signal is recorded frequency resolved, i.e. with a spectrometer, the apparatus constitutes an SHG-FROG with the signal [82]

$$I_{FROG}^{SHG}(\omega, \tau) = \left| \int_{-\infty}^{\infty} E(t)E(t - \tau)e^{-i\omega t}dt \right|^2. \quad (2.49)$$

The recorded signals $I_{AC}(\tau)$ and $I_{FROG}^{SHG}(\omega, \tau)$ are called autocorrelation trace and FROG trace, respectively, both of which are perfectly symmetric with respect to $\tau = 0$, not

revealing any information on the sign of the chirps of the pulse. To remove the time ambiguity, a second, well characterized pulse E_{Ref} may be employed for optical gating of the pulse under investigation, a method termed cross-correlation frequency-resolved optical gating (XFROG) [83]. SHG XFROG yields traces of the form

$$I_{XFROG}^{SHG}(\omega, \tau) = \left| \int_{-\infty}^{\infty} E(t) E_{Ref}(t - \tau) e^{-i\omega t} dt \right|^2, \quad (2.50)$$

which are much more intuitive than FROG traces. Moreover, XFROG allows for the characterization of weak ultrashort pulses when a reference pulse of higher intensity is employed. For the characterization of ultrashort pulses via SHG-FROG or SHG-XFROG thin SHG crystals are needed in order to maintain an efficient frequency doubling across the entire bandwidth and the crystals have to be cut at the correct angles for the desired wavelength range. Thus, an SHG-FROG for 5 fs pulses at 800 nm requires a BBO as thin as 10 μm [84, p. 246].

While SHG-XFROG provides intuitive traces, the necessity for a reference pulse is a drawback, especially when it has to be a few-cycle pulse. Fortunately, the time ambiguity of self-referenced FROG techniques is raised when a third order optical process is employed. This is the case e.g. in the third harmonic generation frequency-resolved optical gating (THG-FROG), the polarization gate FROG (PG-FROG), transient-grating FROG (TG-FROG) and self-diffraction FROG (SD-FROG). The transient grating and self-diffraction four-wave mixing techniques require only a thin slice of glass as χ^3 -medium for the nonlinear interaction, which is very convenient. TG-FROG is background-free and phase-matched, making it very sensitive. SD-FROG is not phase-matched, which can cause errors in the measured trace for extremely short pulses and makes it less sensitive than TG-FROG [82, 85].

2.4.2 TG-FROG

TG-FROG is usually realized in a crossed-beam phase-matched coherent anti-Stokes Raman scattering (BOXCARS) arrangement [86] as shown in fig. 2.10. The input pulse is split into three beams k_1 , k_2 and k_3 . k_3 is variably delayed and all three beams are brought on parallel paths in the corners of a square or a rectangle. The beams are then focused into the nonlinear medium for degenerate four-wave mixing (FWM) in a BOXCAR geometry. After nonlinear interaction the signal beam $k_S = k_3 + k_1 - k_2$ emerges in the fourth corner of the rectangle and is easily isolated by means of an iris for detection by a spectrometer. This FWM process can be interpreted as a Bragg diffraction of the delayed beam k_3 by a transient refractive index grating induced by the two pump beams k_1 and k_2 by means of the optical Kerr effect. A TG-FROG apparatus yields traces of the form [82]

$$I_{FROG}^{TG}(\omega, \tau) = \left| \int_{-\infty}^{\infty} E(t) |E(t - \tau)|^2 e^{-i\omega t} dt \right|^2. \quad (2.51)$$

For Gaussian pulses, the trace given by Eq. 2.51 has a Gaussian intensity profile as well, whereby the temporal width of the trace is elongated by a factor of $\sqrt{3/2} \approx 1.225$

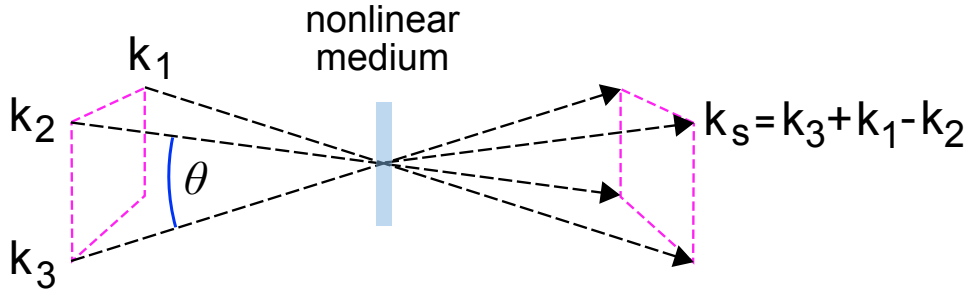


Figure 2.10: TG-FROG: The input beam is split into three beams k_1 , k_2 and k_3 . k_3 is variably delayed and all beams are brought on parallel paths in the corners of a square or rectangle. All beams are focused into a nonlinear medium for four-wave mixing in a BOXCARS geometry. The signal beam k_s emerges in the fourth corner of the rectangle. θ is the intersection angle between the beams.

when compared to the duration of the measured pulse [87, p.283]. Moreover, it has to be considered that the finite crossing angle θ of the beams in the BOXCARS arrangement causes some temporal smearing of the TG-FROG trace. The relative delay between pulses has a transversal variation

$$\Delta\tau_{trans} = 2(d_f/c) \tan(\theta/2), \quad (2.52)$$

depending on the focal diameter d_f and the crossing angle θ [87, p.143]. Moreover, a longitudinal variation of the delay occurs while the pulses travel across the nonlinear medium which amounts to

$$\Delta\tau_{long} = L\theta^2/2c, \quad (2.53)$$

with the thickness L of the nonlinear medium [87, p.151]. Due to the variation of the delay, the measured pulse duration τ_{meas} is increased according to

$$\tau_{meas} = \sqrt{\tau_0^2 + \beta\Delta\tau^2}, \quad (2.54)$$

with the scaling constant β depending on the beam geometry. For a TG-FROG in a BOXCARS arrangement $\beta \approx 5/3$ [87, p.283]. The transient grating (TG) technique can also be employed for XFROG, forming transient-grating cross-correlation frequency-resolved optical gating (TG-XFROG). If a well characterized reference pulse E_{ref} is available for optical gating, it can be used for beams k_1 and k_2 . By replacing the gate function $|E(t - \tau)|^2$ in Eq. 2.51 by $|E_{ref}(t - \tau)|^2$ an expression for the TG-XFROG trace is obtained:

$$I_{XFROG}^{TG}(\omega, \tau) = \left| \int_{-\infty}^{\infty} E(t) |E_{ref}(t - \tau)|^2 e^{-i\omega t} dt \right|^2. \quad (2.55)$$

Usually a slice of glass is used as a nonlinear medium, which should be sufficiently thin such that it introduces only negligible dispersion. The phase-matched bandwidth of a

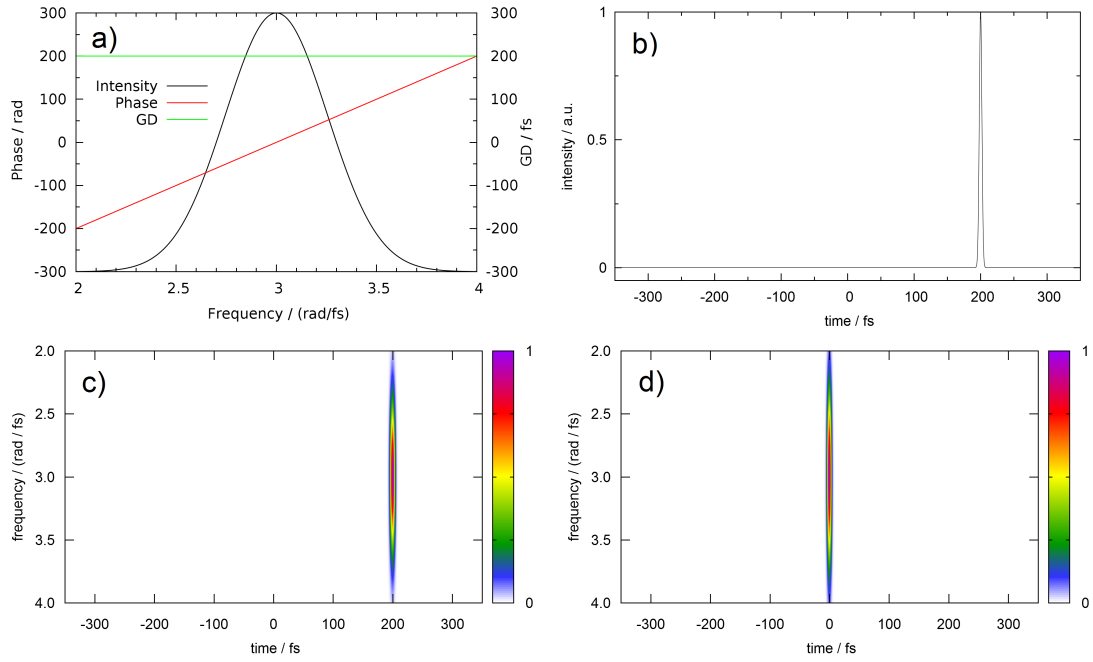


Figure 2.11: Simulation of a laser pulse with a central frequency $\omega_0 = 3$ rad / fs, a FWHM bandwidth of 0.6 rad / fs and a linear spectral phase with $\phi' = 200$ fs. (a) Spectral intensity, spectral phase and group delay GD. (b) Temporal intensity. (c) Simulated TG-XFROG trace calculated with a Gaussian 6 fs FWHM gate function. (d) Simulated TG-FROG trace. Note: With self-referenced measurement techniques like TG-FROG, the temporal shift cannot be determined.

TG-FROG is comparable with the bandwidth of the pump beams k_1 and k_2 . The phase-matched bandwidth is further increased due to the focusing of the beams, as the cones of the foci, which contain wave-vectors with a range of angles, allow for more geometric options for phase matching [88]. Although Lee et al. made these considerations for a TG-XFROG, they apply for a TG-FROG as well. However, for TG-FROG it has to be taken into account, that the full bandwidth may not be available in the pump beams k_1 and k_2 at all delays τ when measuring complex pulses, potentially leading to the loss of phase-matching and hence to the loss of signal.

In the following some simulated ultrabroadband laser pulses are shown, to illustrate the effects of the coefficients $\phi'(\omega_0)$, $\phi''(\omega_0)$ and $\phi'''(\omega_0)$ in the Taylor series of the spectral phase (Eq. 2.18). Because a TG-FROG was employed for pulse characterization in the course of this work, simulated TG-FROG traces of the example pulses are shown. TG-XFROG provides very intuitive traces and simulated TG-XFROG traces thus are a very useful representation of complex pulses. Therefore, simulated TG-XFROG traces are shown here as well and are employed for the representation of optimized laser pulses in the course of this work. The TG-FROG traces are calculated according to Eq. 2.51 and the TG-XFROG traces are calculated according to Eq. 2.55, whereby the term $|E_{ref}(t - \tau)|^2$ was replaced by a Gaussian gate function $G(t - \tau)$ with a variable FWHM temporal width. Essentially, for every time τ , the electric field $E(t)$ of the pulse is gated with $G(t - \tau)$, is Fourier transformed and finally the absolute square is computed

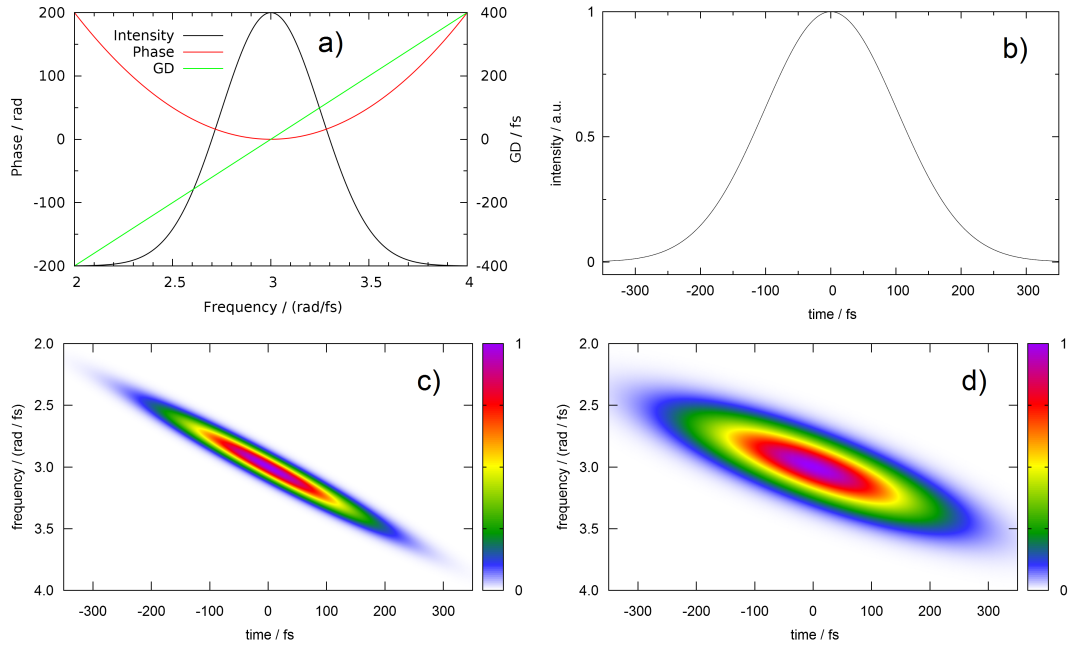


Figure 2.12: Simulation of a laser pulse with a central frequency $\omega_0 = 3$ rad / fs, a FWHM bandwidth of 0.6 rad / fs and a quadratic chirp of $\phi'' = 400$ fs². (a) Spectral intensity, spectral phase and group delay GD. (b) Temporal intensity. (c) Simulated TG-XFROG trace calculated with a Gaussian 30 fs gate function. The long gate function was chosen for high spectral resolution, as there is no fast structure to resolve. (d) Simulated TG-FROG trace. Note: The TG-FROG trace shows a stronger tilt than the TG-XFROG trace and hence chirps cannot be “read” directly from the TG-FROG trace.

to obtain the spectral intensity $I(\omega)$ for each time τ . The temporal width of the gate function $G(t - \tau)$ determines the temporal resolution and also the spectral resolution of the TG-XFROG traces. Of course, temporal resolution and spectral resolution are related by the Fourier transformation and hence scale inversely. So, in order to attain a high spectral resolution, a long $G(t - \tau)$ has to be employed while to attain a high temporal resolution, a short $G(t - \tau)$ is needed. This is investigated in Fig. 2.13 showing different TG-XFROG traces of a pulse with a third order phase function. There is always a trade-off between spectral and temporal resolution in TG-XFROG.

All simulated pulses shown here have a Gaussian spectrum centered at 3 rad / fs with a FWHM bandwidth of 0.6 rad / fs. This is a huge bandwidth, but comparable with the bandwidth of the pulses obtained from the laser setup developed in the course of this work.

A simulated pulse with a linear spectral phase ($\phi'(\omega_0)=200$ fs and all other coefficients set to zero) is illustrated in Fig. 2.11. The pulse is transform limited and shifted to later times by 200 fs.

A simulated pulse with a quadratic spectral phase ($\phi''(\omega_0)=400$ fs² and all other coefficients set to zero) is illustrated in Fig. 2.12. The pulse features a positive linear chirp.

A simulated pulse with a cubic spectral phase ($\phi'''(\omega_0)=1800$ fs³ and all other coefficients set to zero) is illustrated in Fig. 2.13. The pulse features a positive quadratic chirp.

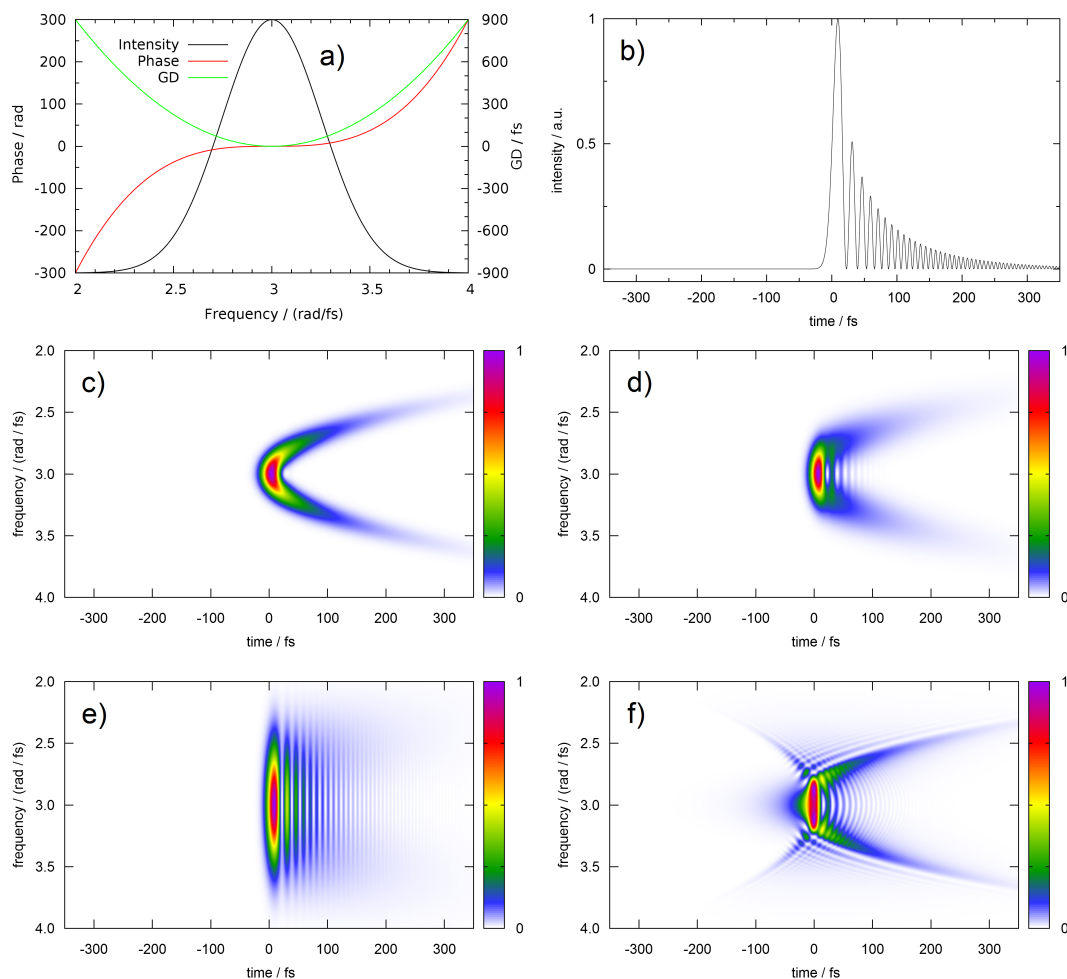


Figure 2.13: Simulation of a laser pulse with a central frequency $\omega_0 = 3$ rad / fs, a FWHM bandwidth of 0.6 rad / fs and a quadratic chirp of $\phi''' = 1800$ fs³. (a) Spectral intensity, spectral phase and group delay GD. (b) Temporal intensity. (c) Simulated TG-XFROG trace calculated with a Gaussian 30 fs gate function. (d) Simulated TG-XFROG trace calculated with a Gaussian 15 fs gate function. (e) Simulated TG-XFROG trace calculated with a Gaussian 6 fs gate function. Note the trade-off between spectral and temporal resolution in the TG-XFROG traces. The trace in (c) contains mainly spectral information, while the trace in (e) contains mainly temporal information. (f) Simulated TG-FROG trace. The TG-FROG trace contains a lot of spectral and temporal information, but is much more complex than the TG-XFROG traces.

2.5 Coherent Control

The development of coherent control was driven by the ambition of influencing chemical reactions with laser radiation. An early concept for achieving chemical selectivity is mode-selective chemistry, which relies on branching a chemical bond by exciting its respective vibrational mode with a cw laser. Due to rapid IVR, mode-selective chemistry with monochromatic cw lasers or nanosecond lasers seemed not generally feasible. As a consequence, the use of ultrafast laser pulses was proposed for achieving chemical selectivity [5]. In 1985 Tannor and Rice proposed the pump-dump control scheme

[6, 7] to attain selectivity in the dissociation of molecules. In this scheme, a reactant molecule ABC is excited by a pump pulse to a superposition of several vibronic eigenstates, in order to prepare a wavepacket which propagates on the potential energy surface of an excited electronic state. After a delay time t , a second laser pulse is employed to dump the molecule back into the electronic ground state by means of stimulated emission, where it may dissociate into the product channels A+BC or AB+C. Usually, once a wave-packet is created, it will not remain localized, but may quickly disperse on the excited electronic state potential energy surface, compromising selectivity in product yield [89, p. 89]. By tailoring pump and dump pulse, i.e. adjusting central frequencies and spectral phase functions, the wave-packet dynamics can be influenced and selectivity can be improved [90, p. 80] [91]. By tuning the delay time t , the molecule ABC can be dumped to different points on the electronic ground state potential energy surface. In this way, the dynamics on the excited electronic state, which can be influenced by tailoring the pump pulses, are used to manipulate yields in the product channels of the electronic ground state.

Another approach to coherent control was developed by Brumer and Shapiro. In the Brumer-Shapiro scheme, control over the product distribution is achieved by means of quantum interference of multiple coherent paths. The molecule is excited to two or more different intermediate states and after a second photoexcitation, the probability amplitudes in the product channels obtained from the different paths interfere. Control over the yield in the product channels is achieved by altering sign and magnitude of the interference terms [8, 9]. In general, controlling a molecular process with laser pulses can involve more than two excitation steps. The efficiency/probability of excitations depends on Franck-Condon factors, the overlap of the vibrational wavefunctions of initial and final state, which are maximized by proper timing and fine-tuning of the central frequency of the exciting pulse. optimal control theory (OCT), developed by Tannor, Kosloff and Rice [6, 7, 91] and Rabitz et al. [92, 93], deals with the determination of optimal pulses for inducing a given molecular process.

For a given initial wave function $\Psi(t_0)$, it is the objective of OCT to maximize the projection J of the wave function $\Psi(t_f)$ at a given time t_f , onto a defined product state Φ , where

$$J = \langle \Psi(t_f) | \mathcal{P} | \Psi(t_f) \rangle, \quad (2.56)$$

with the projection operator $\mathcal{P} \equiv |\Phi\rangle \langle \Phi|$. Maximization of J is physically constrained by the total energy E_{tot} of the laser pulse which relates to the electric field according to

$$E_{tot} = \int_{t_0}^{t_f} |E(t)|^2 dt, \quad (2.57)$$

and the time-dependent Schrödinger Equation,

$$\left(i\hbar \frac{\partial}{\partial t} - H(t) \right) \Psi = 0. \quad (2.58)$$

If the optimized laser pulse is supposed to be employed in an actual experiment, there are practical constraints such as the limited laser bandwidth or the spectral resolution of the pulse shaping device, which have to be taken into account as well. To determine the optimal electric field, J is maximized by an iterative procedure.

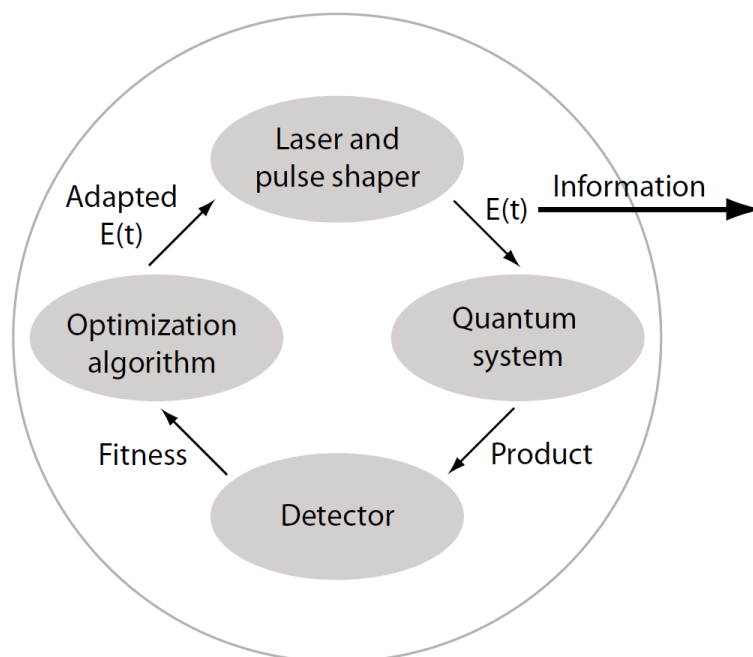


Figure 2.14: Principle of an optimal control experiment employing an adaptive feedback loop for the optimization of the driving laser pulse. A computer running an optimization algorithm creates parameters for various pulse shapes $E(t)$, which are generated by a laser system and a pulse shaper. These pulses are applied to a quantum system and the resulting products are measured by a detector. For each pulse shape, the signal is analyzed to obtain the fitness of that pulse. With the help of the fitness data, the optimization algorithm creates adapted pulse shapes. Finally, information on the quantum system can be obtained from the optimized laser pulse $E(t)$. Image taken from [67].

2.5.1 Coherent Control experiments with adaptive feedback loops

Difficulties in the optimization of laser pulses using OCT can arise from insufficient knowledge of the molecular Hamiltonian. Hence, Judson and Rabitz suggested to design laser pulses by means of adaptive feedback control using a genetic algorithm in a laboratory experiment [20]. In the suggested scheme outlined in Fig. 2.14, the laboratory experiment serves as an “analog computer”, that solves Schrödinger’s equation in real time. A computer running an optimization algorithm first creates parameters for various pulse shapes $E(t)$, which are generated by a laser system and a pulse shaper. These pulses are applied to a quantum system and the resulting products are measured. For each pulse shape, the signal is evaluated to obtain the fitness of that pulse. With the help of the fitness data, the optimization algorithm creates adapted pulse shapes. The most popular optimization algorithms for coherent control experiments are EAs. EAs use optimization strategies which are inherited from natural evolution. A randomly initialized population of individuals (laser pulses) gradually evolves towards better regions of the search space by means of selection, mutation and recombination [94]. The first quantum control experiment using an adaptive feedback loop was performed by Bardeen et al. in 1997, optimizing the electronic population transfer in a laser dye molecule [21].

Adaptive feedback loops have since then been successfully applied in numerous coherent control experiments, for example in the enhancement or suppression of the photodissociation of organometallic molecules [22, 23], the quantum control of energy flow in light harvesting [24] and the photoionization of potassium dimers with polarization-shaped pulses [25].

White-Light Laser Setup

3

3.1 Introduction

Driven by the desire to investigate and control ever faster processes, supercontinuum light sources for the generation of few- and single-cycle pulses are improved continuously. In 1987, 6 fs pulses were generated by Fork et al. [95], which was a long-standing record. Pulses obtained from a dye amplifier were spectrally broadened in a Quartz fiber, compressed by means of a grating and prism sequence and analyzed by interferometric autocorrelation. Eventually, the record of Fork et al. was broken by Baltuska et al. in 1997 [96]. They used a single-mode fiber for spectral broadening of 13 fs pulses obtained from a cavity-dumped Ti:Sa laser at a repetition rate of 1 MHz. Compression using a grating and prism sequence yielded 4.9 fs pulses, while 5.5 fs pulses were obtained by compression with a pair of chirped mirrors and a prism sequence. Higher pulse energies were achieved by using hollow-core fibers filled with noble gases for spectral broadening. Also in 1997, Nisoli et al. generated 5 fs pulses with multi-gigawatt peak powers [97] by using an argon-filled hollow-core fiber and a chirped mirror to compensate for cubic phase distortion. In the same year, Sartania et al. generated 0.5 mJ, 5 fs pulses featuring a peak power of 0.1 TW, by means of an argon-filled hollow-fiber and a chirped mirror compressor [98]. Spectral broadening in noble gas filled hollow-core fibers has since then become a widespread technique [29, 30, 56, 59, 99, 100] and, combined with pulse shaping techniques, led to the generation of pulses as short as 2.6 fs by Matsubara et al. [60]. Few-cycle field-synthesis with unamplified pulses obtained from a CEO-stabilized Ti:Sa oscillator has been demonstrated by Binhammer and Rausch et al., however only relatively short waveforms are shown due to the limitation of the spectral phase interferometry for direct electric-field reconstruction (SPIDER) apparatus employed for pulse characterization [101, 102].

While propagation through optical fibers serves well as a means for spectral broadening of amplified pulses, filamentation (see section 2.3.3) has some practical advantages. Filamentation in gaseous media was introduced as a method for spectral broadening by Corkum et al. already in 1986 [103], however it took a long while until filamentation was put to use for pulse compression. In 2004 Hauri et al. demonstrated the compression of 43 fs near infrared (NIR) pulses to 5.7 fs by twofold filamentation in argon and subsequent chirped mirror compression [72]. In addition to this highly encouraging result, different studies have shown that filamentation preserves the CEO phase stability, a prerequisite for the controlled generation of isolated attosecond pulses [72, 104, 105]. Filamentation also allows for the self-compression to sub-8 fs pulse durations in the multi-millijoule regime [106]. Highly efficient spectral broadening of 0.86 mJ NIR pulses was attained by filamentation in SF₆ gas, resulting in an output spectrum spanning from 440 to 875 nm FWHM [107]. Sub-7 fs pulses were generated by filamentation of 1 mJ NIR pulses in air at atmospheric pressure and subsequent chirped mirror compression

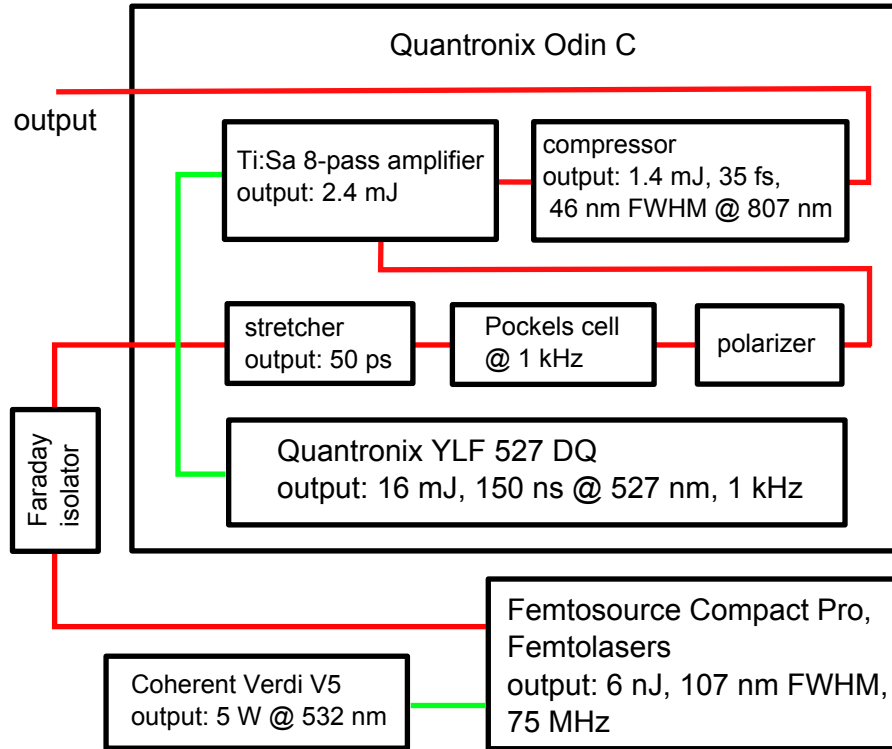


Figure 3.1: Scheme of the laser system showing the major components. For details see text.

[46]. Moreover, filamentation of NIR pulses in atmospheric air facilitates the generation of octave-spanning spectra, with an intensity of the visible part of the spectrum of a few percent of the maximum intensity in the NIR. In combination with spectral filtering, a relatively homogeneous octave-spanning spectrum can be obtained by filamentation of 1 mJ NIR pulses in air at atmospheric pressure, circumventing the need for windowed gas filled tubes [47]. Laser pulses undergoing filamentation do not suffer from misalignment of fiber coupling [108], which makes filamentation more suitable for lengthy experiments.

In the course of this work, an improved setup for the generation of tailored white-light pulses was developed, incorporating two filamentation stages in atmospheric air, pre-compression with ultrabroadband chirped mirrors and a pulse shaper setup. The synthesis of near-arbitrary, amplified pulses with few-cycle subpulses has been demonstrated for the first time, while the phase-shaping capabilities of the pulse shaper setup are fully exploited for the generation of pulse shapes enduring several hundreds of femtoseconds[45].

The combination of supercontinuum bandwidths with few-cycle subpulses, pulse shaping and a peak-power in the 10 GW regime makes this setup a valuable tool for quantum control experiments. Such a setup allows for addressing very fast processes as well as a wide range of electronic resonances [109]. With adequate focusing, intensities approaching the strong-field regime are attained, further enhancing the chances to achieve resonance by means of Stark-shifting of the electronic energy levels [39].

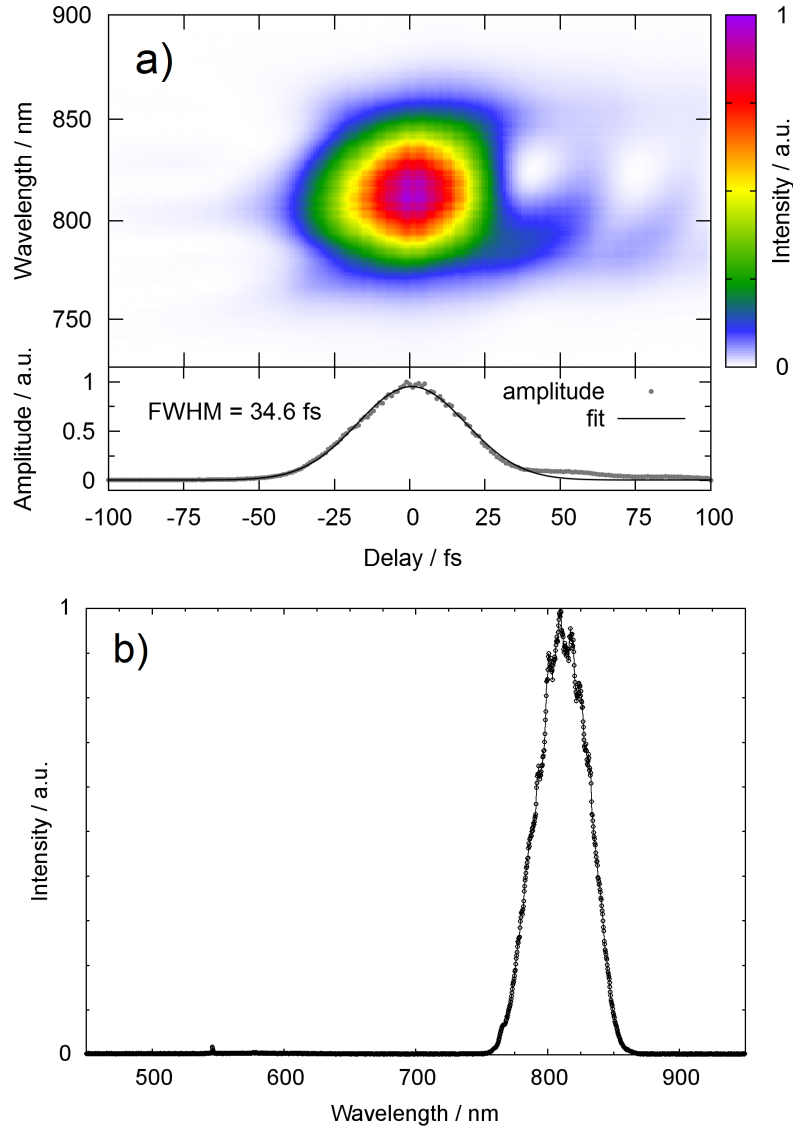


Figure 3.2: Output pulse of the Odin C amplifier. a) TG-FROG trace. b) Pulse spectrum.

3.2 Laser system

The laser system used in this work is a commercial Ti:Sa based fs-oscillator and a 1 kHz multipass amplifier system. A schematic representation of the laser system, showing the major components, is depicted in Fig. 3.1. The oscillator providing the seed pulses is a Femtosource Compact Pro (Femtolasers) producing 5-6 nJ pulses with a bandwidth of 100 nm FWHM and a central wavelength of 805 nm at a repetition rate of 75 MHz. With external chirped mirror compression this oscillator generates 11 fs pulses. The oscillator is pumped at a power of 5 W by a green frequency-doubled Nd:Vanadate cw-laser (Verdi V5, Coherent) with a wavelength of 532 nm. After passing a Faraday isolator to protect the oscillator from back-reflected amplified pulses, the seed pulses are coupled into the Quantronix Odin C chirped pulse amplification system. Prior to amplification, the seed pulses are strongly chirped by the stretcher, elongating the pulses to about 50 ps to prevent damage of the amplifier's Ti:Sa crystal. Thereafter, 1000 pulses per second are

picked from the 75 MHz train by means of a Pockels cell and a subsequent polarizer. The seed pulses are then steered into the 8-pass amplifier where they are amplified to 2.4 mJ. The amplifier's Ti:Sa active medium is pumped by a Quantronix YLF 527 DQ laser, providing 16 mJ, 150 ns pulses with a wavelength of 527 nm at a repetition rate of 1 kHz. The pump pulses are synchronized with the seed pulses by means of the Pockels cell driver electronics (Medox Electro-optics, Inc.) and a fast photodiode (EOT) detecting the seed pulses. After amplification, the pulses are spatially filtered for mode-cleaning, by focusing into a pinhole. After recollimation, the pulses are compressed to 35 fs pulses with a central wavelength of 807 nm and a FWHM bandwidth of 46 nm. A TG-FROG trace and the typical spectrum of the output pulses is depicted in Fig. 3.2.

3.3 Supercontinuum Generation

The complete optical setup for white-light generation and shaping and pulse characterization is shown in Fig. 3.3. Supercontinuum generation is realized in two filamentation stages with intermediate chirped mirror compression [72] in air at atmospheric pressure [46]. For a mild spectral broadening in the first filamentation stage, the pulses from the amplifier are attenuated by spatial filtering with a circular iris (I1) to 430 μJ . The input-pulse is adjusted to have zero linear chirp at the location of the focus, like the amplifier's output-pulse shown in Fig. 3.2 a). The seed pulse for filamentation has a duration of 35 fs and a bandwidth of 46 nm FWHM, corresponding to filamentation at a peak power of approximately 12 GW. To initiate filamentation, the pulses are focused with a concave spherical mirror (SM1, $R = 4000$ mm) into an air filled thin tube with open ends. The tube impedes a disturbing airflow in the filamentation region, improving the stability of the output beam. A concave spherical mirror (SM2, $R = 5000$ mm) recollimates the beam. The spectrum of the laser pulses emerging from the first filament, which is modulated and broadened to approximately 70 nm FWHM by self-phase modulation, is depicted in Fig. 3.4 b). For the second filamentation stage, the pulses are compressed by two double-bounces on a pair of chirped mirrors (CM1 and CM2, Layertec) with an average GDD of -60 fs^2 per double-bounce over the spectral range of 700 to 900 nm. In this way, a compression to 15 fs is attained in the first filamentation stage with a final pulse energy of 400 μJ , yielding a high transmission of approximately 90%. The significant compression is essential for the very efficient generation of visible wavelengths in the second filamentation stage.

The pulse energy is adjusted to 300 μJ by means of an iris (I2), resulting in a peak power of approximately 20 GW for the second filamentation, which is initiated by focusing with a concave spherical mirror (SM3, $R = 3000$ mm). The length of the optical path to the focus is adjusted such that the filamenting pulses have zero linear chirp, as shown in the TG-FROG trace of the input-pulses for the second filament, Fig. 3.4 a). These pulse parameters resulted in the highest contribution of visible light in the output spectrum, while conical emission is suppressed. After the second filament, the beam is recollimated by a silver coated concave spherical mirror (SM4, $R = 2500$ mm). A strong spectral broadening is achieved in the second filamentation stage, resulting in a spectrum

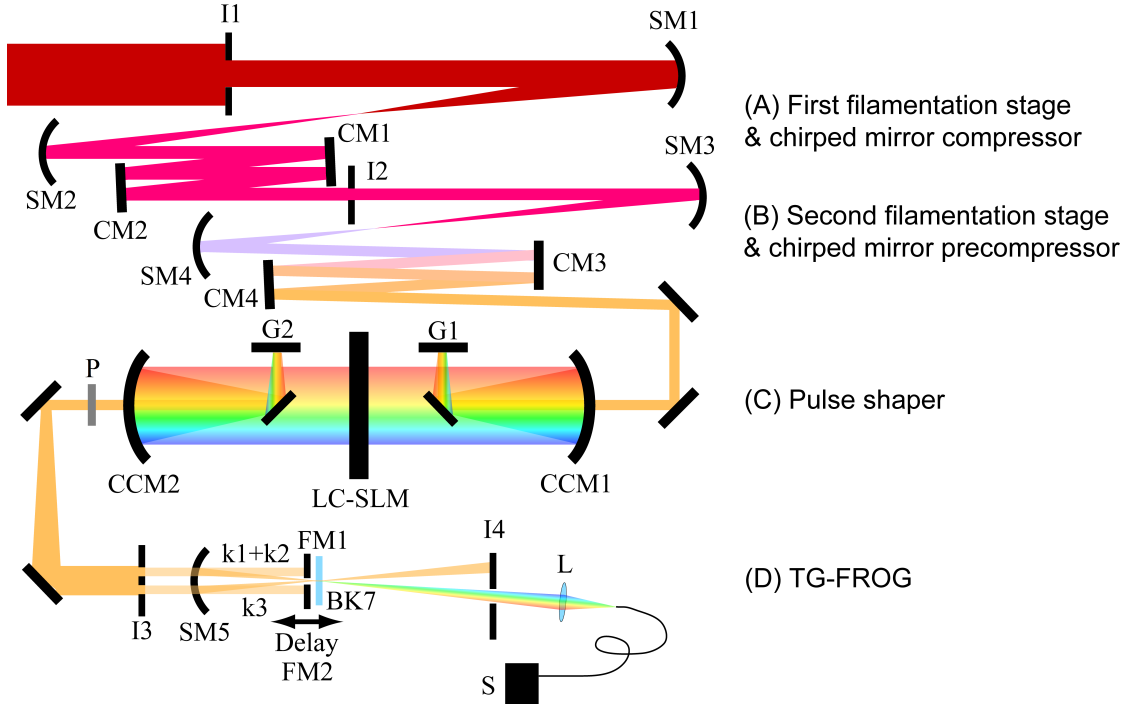


Figure 3.3: Scheme of the experimental setup for supercontinuum generation and pulse shaping. (A) First filamentation stage and compression: (I1) iris, (SM1) concave spherical mirror, $R = 4000$ mm; (SM2) concave spherical mirror, $R = 5000$ mm; (CM1, CM2) chirped mirror pair, $GVD -60 \text{ fs}^2/\text{double-bounce}$. (B) Second filamentation stage and pre-compression: (I2) iris; (SM3) concave spherical mirror, $R = 3000$ mm; (SM4) concave spherical mirror, $R = 2500$ mm; (CM3, CM4) chirped mirror pair, $GVD -40 \text{ fs}^2/\text{double-bounce}$. (C) Pulse shaper: (G1, G2) diffraction grating, 300 l/mm and 600 nm blaze; (CCM1, CCM2) concave cylindrical mirrors, $R = 500$ mm; (LC-SLM) spatial light modulator, 2×640 pixels; (P) polarizer (optional). (D) Frequency-resolved optical gating, TG-FROG: (I3) spatial filter; (FM1, FM2) D-shaped mirrors; (SM5) concave spherical mirror, $R = 500$ mm; (BK7) glass platelet, BK7; (I4) iris; (L) lens, $f = 100$ mm; (S) fiber spectrometer.

with a high contribution in the visible region, spanning the range of $550 - 900 \text{ nm}$ at 10% of the maximum intensity, as depicted in Fig. 3.5 a). The supercontinuum pulses emerging from the second filament are pre-compressed by ten double-bounces on a pair of ultrabroadband chirped mirrors (CM3 and CM4, Layertec), with an average GDD of -40 fs^2 per double-bounce over the spectral range of 510 to 920 nm . The number of reflections for pre-compression after the second filamentation stage is chosen with regard to the dispersion in the LC-SLM and optical path that follows. It is important to note that the ultrabroadband chirped mirror pair does not have a constant GDD over the specified spectral range, leading to a pre-compressed pulse with a varying chirp and a duration on the order of 100 fs . A TG-FROG trace of the pre-compressed pulse is shown in fig. 3.5 b), which exhibits a negative chirp for wavelengths above 715 nm , a positive chirp from 600 to 700 nm and again a negative chirp for the wavelengths between 600 and 510 nm . The information provided by this FROG trace allowed for the compilation

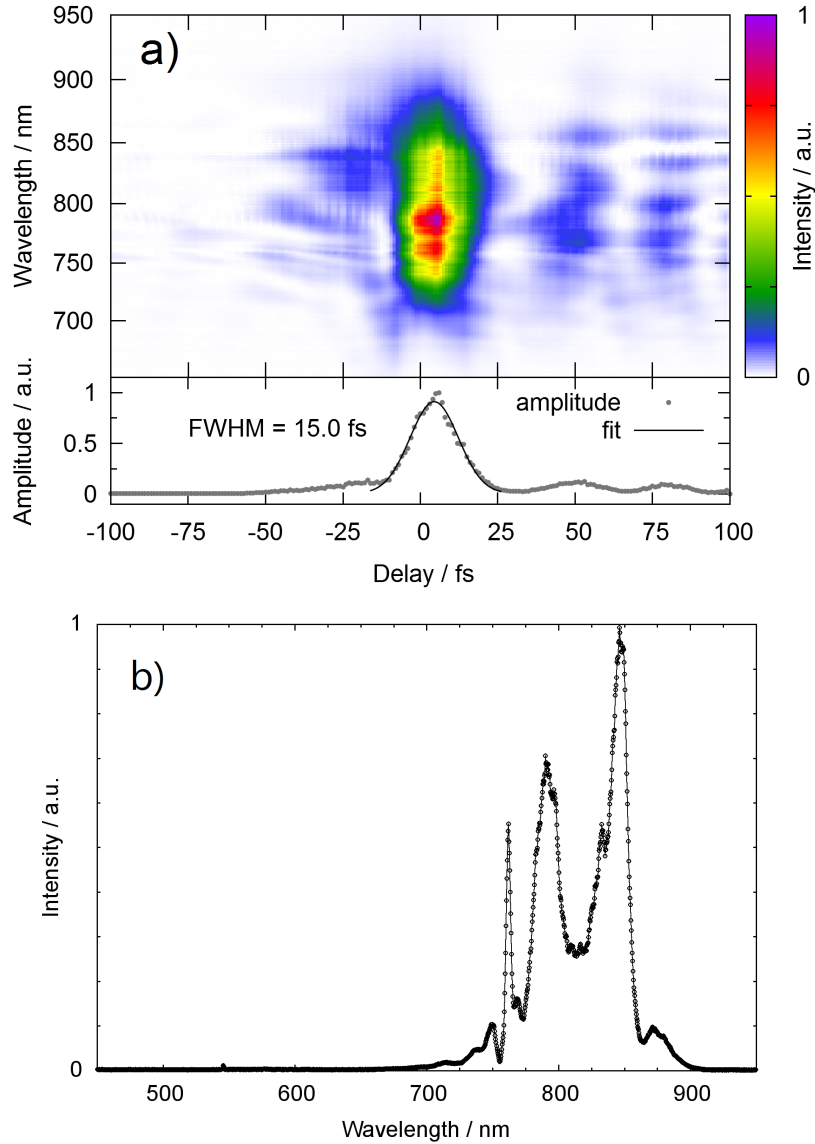


Figure 3.4: Input pulse of the second filament. a) TG-FROG trace. b) Pulse spectrum.

of a phase function for the pulse shaper, which resulted in the compression of these complex supercontinuum pulses.

3.4 Pulse Shaper Setup

After pre-compression, the pulses are guided into the pulse shaper setup, which consists of a 4-f zero dispersion compressor and an LC-SLM (see section 2.2.3). The design of the reflective 4-f zero dispersion compressor built in the course of this work is similar to the one presented in the Ph.D. thesis of Bruno Schmidt [47, p.54]. The incoming beam passes underneath the first concave cylindrical mirror (CCM1, silver coated, $R = 500$ mm), hits the silver coated flat folding mirror and is dispersed by the first diffraction grating (G1). The dispersed beam goes slightly upwards, hits the folding

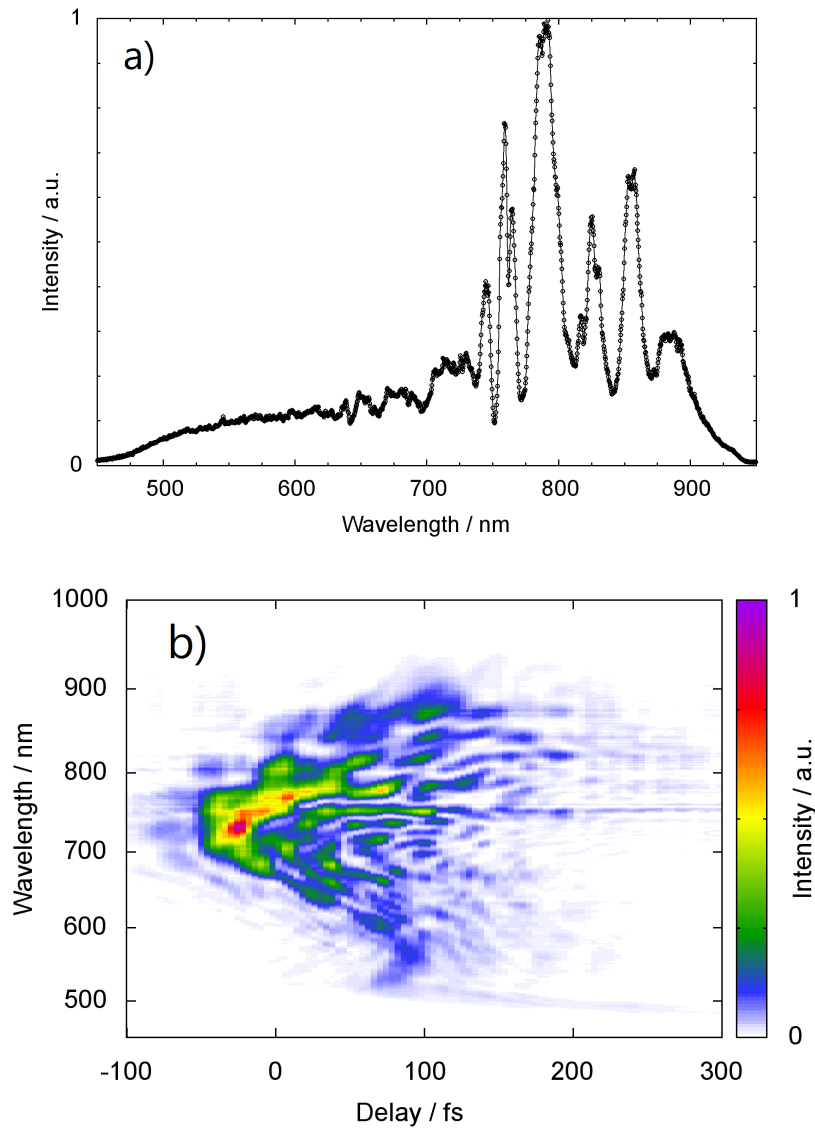


Figure 3.5: a) Output spectrum of the second filament. b) TG-FROG trace of the pulses exiting the second filament, pre-compressed by ten double-bounces on the ultrabroad-band chirped mirrors.

mirror again and is steered towards CCM1. CCM1 parallelizes the spectral components and focuses each wavelength in the Fourier plane, where the LC-SLM (SLM-640-D-VN, Cambridge Research & Instrumentation) is placed. The second concave cylindrical mirror (CCM2, silver coated, $R = 500$ mm) then recollimates the spectral components and, via the second flat folding mirror, focuses them onto the second diffraction grating (G2), where the beam is recollimated. The beam then hits the second flat folding mirror again and exits the pulse shaper setup underneath CCM2. The concave cylindrical mirrors are from Hellma Optik. The gratings made by Horiba / Jobin Yvon have 300 lines / mm and are blazed for 600 nm. An optional wire grid polarizer (P, Edmund Optics) is placed behind the shaper, for calibration, amplitude shaping, or power adjustment. A wire-grid polarizer was selected for this application due to its superior power handling capability

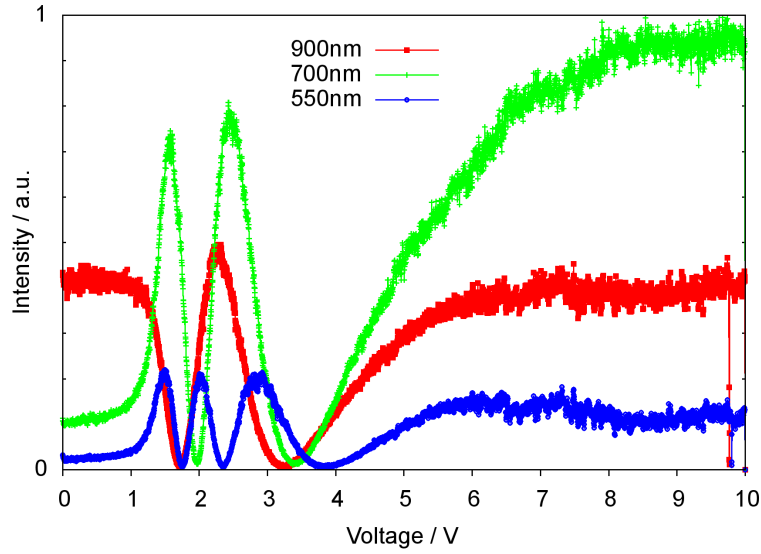


Figure 3.6: Phase retardation calibration measurements for 550 nm, 700 nm and 900 nm. The transmission through a polarizer placed behind the shaper setup is measured while the voltage applied to one array of the LC-SLM is scanned from 0 to 10 V. For details, see text.

and broad wavelength range. The transmission of the pulse shaper setup is approximately 33 %, a menial value attributed to the low efficiency of the gratings, which are not optimized for all wavelengths of the ultrabroadband spectrum.

3.4.1 Calibration of the LC-SLM

The voltage-dependent retardance of the two LC-arrays inside the LC-SLM is wavelength dependent. Due to the ultrabroad wavelength range, the retardance to voltage curves differ strongly from pixel to pixel. Hence, the retardance to voltage curve has to be calibrated for each pixel. The procedure, which was implemented in LabView by Waldemar Unrau in the framework of his diploma thesis and by Bruno E. Schmidt [47], is described below:

The voltage applied to all pixels of one array of the LC-SLM is scanned from minimum (0 V) to maximum (10 V), while the voltage applied to the other array is held constant. During scanning, the transmission through a polarizer placed behind the shaper setup is recorded with a spectrometer. This is done for both arrays. Fig. 3.6 shows the measured transmission curves for three specific wavelengths, while scanning the voltage applied to one array. The slow (y) and fast axes (x) of the LC in one array are oriented at -45° and 45° , respectively. The refractive index of the slow (y) axis is controlled by the applied voltage, thus regulating the phase retardance of the corresponding polarization. The transmission through the polarizer is described by the equation

$$T(V, \lambda) = \cos^2 \left(\frac{\Delta\phi_y(V) - \Delta\phi_x}{2} \right) \quad (3.1)$$

for a given wavelength λ . One oscillation cycle of the transmitted signal corresponds to a 180° rotation of the polarization and a relative phase retardation change of 2π between

ordinary and extraordinary ray. Thus, the transmission curves shown in fig. 3.6 indicate a maximum retardation of more than 6π for 550 nm, around 5π for 700 nm and nearly 4π for 900 nm. By means of equation 3.1, the relative phase retardation ($\Delta\phi_y(V) - \Delta\phi_x$) is calculated. The obtained phase retardation is ambiguous by multiples of 2π and hence it is unwrapped to obtain a steady phase retardation-to-voltage curve $\Delta\phi(V, \lambda)$. Once these curves are obtained for all wavelengths, due to the 2π -ambiguity, all curves $\Delta\phi(V, \lambda)$ have to be aligned, in order to ensure a well-defined retardance-to-wavelength calibration. The alignment of the curves is achieved by searching the voltage position V_{min} of the second last minimum in every transmission curve $T(V, \lambda)$, and subtracting the retardation $\Delta\phi(V_{min}, \lambda)$ from the entire retardation-to-voltage curve. The voltage position V_{min} of the second last minimum is used here, as it is assumed to correspond to an equal retardation, namely 3π , for all wavelengths. This should be the case, because for the maximum voltage (10 V) the retardation is (almost) zero, as the molecules forming the LC are (almost) tilted by 90° , leading to equal refractive indices along the x and y axes of the LC. This assumption is backed by observation, as the $T(V)$ curves remain fairly constant from 6 to 8 V onwards (see Fig. 3.6). The pixel-to-wavelength relation, or pixel-to-angular frequency relation, of the LC-SLM is measured by successively opening a single pixel while all other pixels are set to the voltage of integral minimum transmission. The pixel-to-angular frequency calibration and the resulting wavelength dependent shaping window of the shaper setup is shown in fig. 3.7. The measured angular frequencies were fit with the analytical function $\omega(x) = a / (x - x_0)$, with the pixel number x and parameters a and x_0 , which is a small-angle approximation of the projection of the spectrum onto the LC-SLM. Due to the very broad spectrum, the spectral resolution of the shaper setup varies significantly with wavelength, or light frequency. This, in turn, results in an equally strong variation of the shaping window across the spectrum (see section 2.2.3). Here, to be able to plot a function, the shaping window $\tau(x)$ is defined as $\tau(x) = \pi / \delta\omega = \pi / \omega'(x)$, with the bandwidth transmitted through a single pixel $\delta\omega$. Usually, it is required that $\tau(x) \ll \pi / \delta\omega$ [49, 61, 68]. The definition of the shaping window used here corresponds to the Nyquist sampling limit and its full exploitation would lead to the generation of strong, undesired sampling replica pulses [71]. The shaping window ranges from more than 1000 fs at 900 nm to less than 350 fs at 500 nm, as shown in Fig. 3.7. Hence, to avoid strong artifacts when tailoring pulses, the temporal shift should be restricted to a maximum of 600 fs for wavelengths around 800 nm and to a maximum of 300 fs at 550 nm. The formation of replica pulses is investigated and further discussed in section 3.7.1.

3.5 TG-FROG Setup

For characterization, the pulses are steered to the dispersion-free TG-FROG setup [46, 110]. The TG-FROG setup employs a three-hole spatial filter (I3) as a dispersion-free beam splitter, which is depicted in Fig. 3.8 a). The spatial filter is made from a piece of paper and the holes (1 mm diameter) are stitched with a pin in the corners of a square

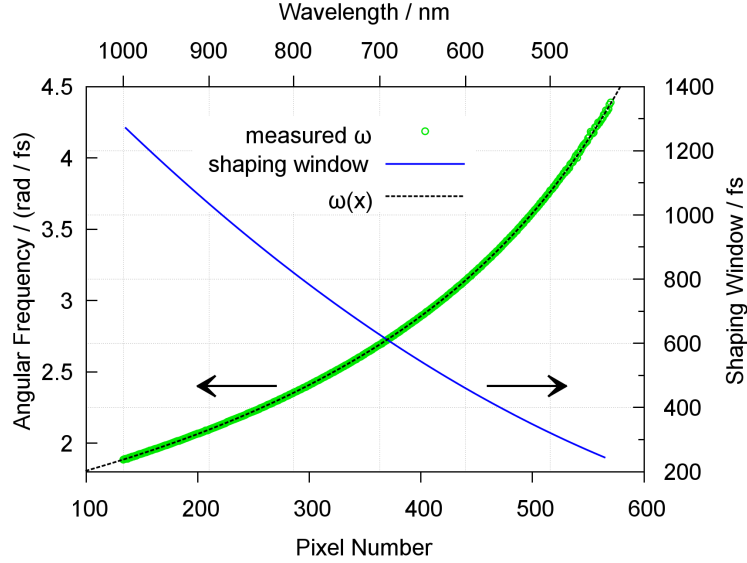


Figure 3.7: Green, left y-axis: Measured pixel-to-angular frequency calibration of the shaper setup. Black dashed: fit function $\omega(x)$ of the pixel-to-angular frequency calibration. Blue, right y-axis: Shaping window versus wavelength (top x-axis). Note that the shaping window ranges from more than 1000 fs at 900 nm to less than 350 fs at 500 nm.

with 2.5 mm edge length. The three beams k_1 , k_2 and k_3 then hit the D-shaped mirrors FM1 and FM2 as shown in fig. 3.8 b). Here k_3 is variably delayed by moving FM2, which is mounted on a delay stage (PLS-85, MICOS). The three beams then go slightly downwards on parallel beam paths and hit a spherical mirror (SM5, $r = 500$ mm) which focuses all beams into a BK7 glass platelet with a thickness of $L = 0.17$ mm, for degenerate four-wave mixing in a BOXCAR geometry (see section 2.4.2). After four-wave mixing, the signal beam k_S arises in the fourth corner of the square. k_S is isolated by means of an iris (I4), as shown in Fig. 3.8 c), about 0.5 m behind the glass platelet. The signal beam is then focused by a lens (L , $f = 100$ mm) into an optical fiber connected to the spectrometer (S, Ocean Optics USB 2000), to record the spectrum of k_S .

As discussed in section 2.4.2, a variation of the relative delay between pulses arises from the finite intersection angle θ between beams. With a beam separation of 2.5 mm and the focal length of 250 mm one obtains $\theta \approx 0.57^\circ$. The beam diameter in the focus is approximately $d_f \approx f\lambda/d_i \approx 200 \mu\text{m}$, considering the input beam diameter $d_i = 1$ mm and $\lambda = 800$ nm and assuming a Gaussian input beam. With these values, according to Eq. 2.52, the transversal variation of the delay amounts to $\Delta\tau_{trans} \approx 6.67$ fs. The longitudinal variation of the delay obtained from Eq. 2.53 is $\Delta\tau_{long} \approx 1.4 \cdot 10^{-17}$ s, which is negligible. According to Eq. 2.54, with the estimated $\Delta\tau_{trans} \approx 6.67$ fs, the minimal temporal width of the measured signal, measured for an infinitesimally short pulse, would be 8.6 fs. However, the shortest signals measured with this TG-FROG setup had a duration of 6.0 fs (corresponding to a deconvoluted pulse duration of 4.9 fs), indicating that $\Delta\tau_{trans}$ is largely overestimated by Eq. 2.52 (see also [87, p.148]).

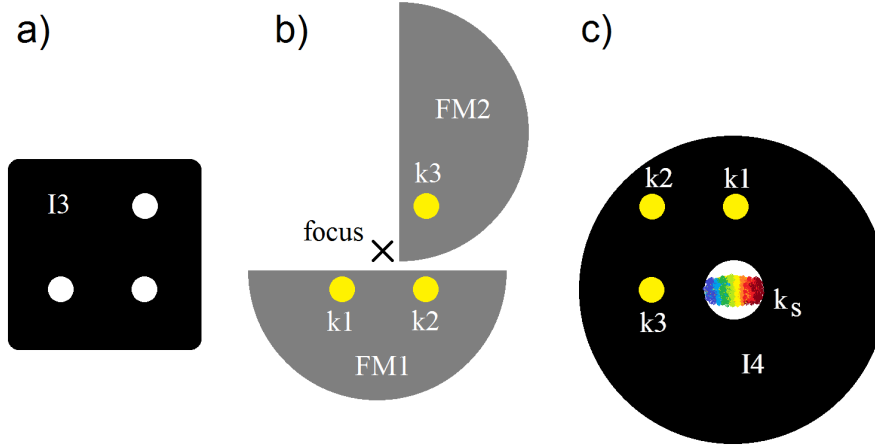


Figure 3.8: Details of the TG-FROG setup. a) spatial filter (I3). The holes have a diameter of 1 mm and are located in the corners of a square with 2.5 mm edge length. b) Arrangement of the D-shaped mirrors FM1 and FM2, spots of the beams k_1 , k_2 and k_3 and the position of the focus, which lies in the glass platelet (BK7) about 15 mm behind the D-shaped mirrors. FM2 is mounted on a delay stage. c) Selection of the signal beam k_s by means of iris I4.

3.6 Pulse Compression

To compress the pre-compressed pulse shown in fig. 3.5 b), a three-part spectral phase function $\phi_{off}(\omega)$, which corrects the varying chirp of the pre-compressed pulse, was compiled with the help of the TG-FROG trace of the pre-compressed pulse and was refined by trial and error. The spectral phase function $\phi_{off}(\omega)$ consists of a quadratic function with positive curvature in the range of 500 - 600 nm to compensate the negative chirp observed in this range, a quadratic function with negative curvature in the range of 600 - 714 nm to compensate for the positive chirp in this range and a function with positive curvature in the range of 714 - 950 nm to compensate for the negative chirp in the NIR range. The explicit phase functions are given in Table 3.1, and $\phi_{off}(\omega)$ is depicted in fig. 3.9 b), together with the spectrum of short pulses measured after the pulse shaper setup.

With this simple approach it was possible to compress the supercontinuum pulses to 4.9 ± 0.4 fs reproducibly. A typical TG-FROG trace of a short pulse is shown in fig. 3.9 a).

3.7 Supercontinuum Pulse Shaping

Beyond the capability of a refined spectral phase compensation for pulse compression, the pulse shaper allows for the generation of complex pulse shapes.[48, 102, 111] A very short compressed pulse is the prerequisite for the controlled generation of complex pulse shapes with few-cycle subpulses. To generate complex pulse shapes, an additional spectral phase function $\phi_a(\omega)$ is added to the phase function $\phi_{off}(\omega)$ required for pulse compression.

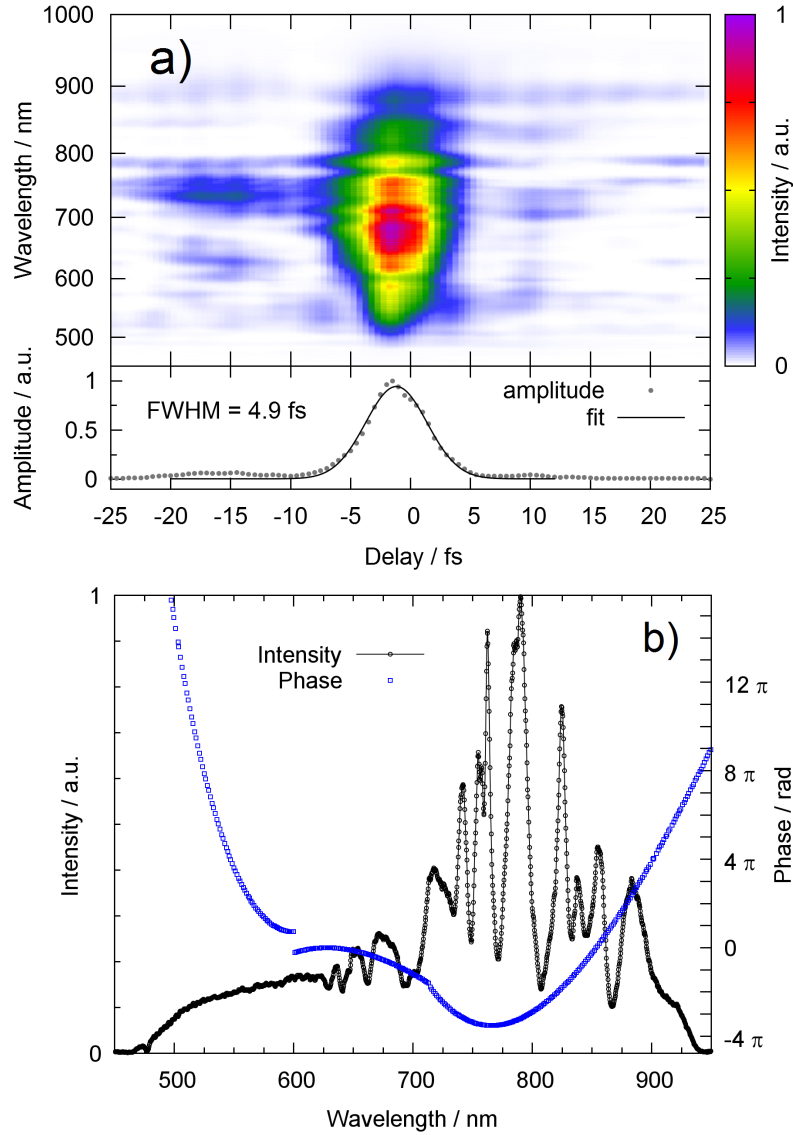


Figure 3.9: a) Typical TG-FROG trace of a 4.9 fs pulse compressed by a combination of dispersion compensation using a pair of ultrabroadband chirped mirrors and refined spectral phase compensation using the pulse shaper. b) Pulse spectrum (black, left y-axis) after the shaper and spectral phase function ϕ_{off} (blue, right y-axis) applied for pulse compression.

3.7.1 Fourier Shifts

Fourier shifting a part of the spectrum with a linear phase function is a simple way for generating double pulse sequences. These can be used for pump-probe experiments and they are a good calibration test. Furthermore, Fourier shifts are a means for evaluating the limits of the pulse shaper setup, imposed by the discrete sampling of the spectral phase function. A spectral phase function for pulse compression $\phi_{off}(\omega)$, similar to the function given in Table 3.1, was the starting point for the generation of double pulse sequences. By adding a linear phase function $\phi_a(\omega)$ for a part of the spectrum, the respective part of the pulse is shifted in time. The explicit additional spectral phase

Spectral Range	$\phi_{off}(\omega)$	Coefficients, b_n
500-600 nm	$b_1(\omega - \omega_0)^2 + b_2\omega$	$b_1 = +113 \text{ fs}^2$ $b_2 = -32 \text{ fs}$
600-714 nm	$b_1(\omega - \omega_0)^2$	$b_1 = -39 \text{ fs}^2$
714-950 nm	$b_1(\omega - \omega_0)^2 + b_2\omega$	$b_1 = +173 \text{ fs}^2$ $b_2 = +187 \text{ fs}$

Table 3.1: Spectral phase function $\phi_{off}(\omega)$ for compression of the pre-compressed pulses. $\omega_0 = 3.0 \text{ rad/fs}$.

functions $\phi_a(\omega)$ are given in Table 3.2. Fig. 3.10 shows TG-FROG traces of double pulse sequences, where the NIR part of the spectrum above 724 nm was shifted by $\pm 600 \text{ fs}$. The TG-FROG traces show, that the intended sub-pulse delay of 600 fs is met with a high accuracy and the shifted sub-pulse remains unchirped. This is a good confirmation of the proper calibration of the LC-SLM, as an incorrect calibration would result in a distorted phase of the shifted pulse and / or a wrong delay. A 600 fs shift of the NIR part is approaching the limit of the shaping window, as the Nyquist limit at 724 nm is around 670 fs.

Fig.	Spectral Range	$\phi_a(\omega)$
3.10 a)	500-724 nm	0
	724-950 nm	$-600 \text{ fs} \cdot \omega$
3.10 b)	500-724 nm	0
	724-950 nm	$+600 \text{ fs} \cdot \omega$
3.11 a)	500-700 nm	$-400 \text{ fs} \cdot \omega$
	724-950 nm	0
3.11 d)	500-725 nm	$-200 \text{ fs} \cdot \omega$
	726-950 nm	0

Table 3.2: Explicit additional spectral phase functions $\phi_a(\omega)$ for the generation of double pulse sequences by temporal shifting of a part of the spectrum.

For the VIS part of the spectrum, the attainable temporal shift is smaller, as the shaping window shrinks with descending wavelength. Fig. 3.11 a) shows a TG-FROG trace of a double pulse sequence, where the VIS part of the spectrum ($\lambda < 700 \text{ nm}$) was shifted by 400 fs to negative times. This TG-FROG trace also shows a sampling replica pulse in the region between +300 and +800 fs, stemming from the insufficient sampling of the spectral phase function and the desired sub-pulse at -400 fs suffers from a high intensity

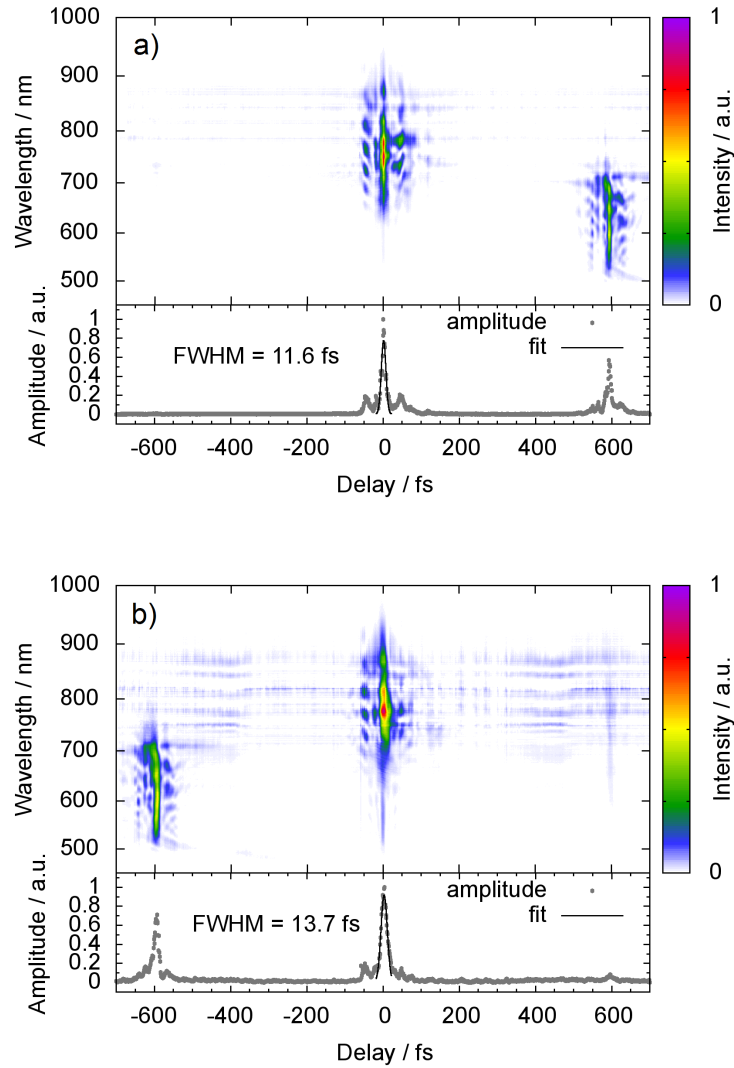


Figure 3.10: Double pulse sequences generated by temporal shifting of a part of the spectrum with a linear phase function. a) NIR part of the spectrum ($\lambda > 724$ nm) shifted by 600 fs to negative times. b) NIR part of the spectrum ($\lambda > 724$ nm) shifted by 600 fs to positive times. The explicit additional spectral phase functions are given in Table 3.2.

loss. Fig. 3.11 b) is a zoom-in on the VIS part of the TG-FROG trace better showing the sampling replica pulse. Since the resolution of the pulse shaper decreases with the wavelength, the replica pulse has a strong negative chirp. For a better understanding of the formation of the replica pulse, a section of the phase function written on the LC-SLM around 3.05 rad / fs is depicted in Fig. 3.11 c) in wrapped representation. The points of the phase function sampled by the LC-SLM are shown with errorbars indicating the spectral width covered by the pixels. The equivalent spectral phase function causing the replica pulse is shown as well. Due to the dispersion in the spectral resolution, the sampled points of the phase function can be interpreted as a second order phase function with varying positive slope [71] (for the sake of simplicity, higher order terms are neglected here). The parameters for this second order phase function can be extracted

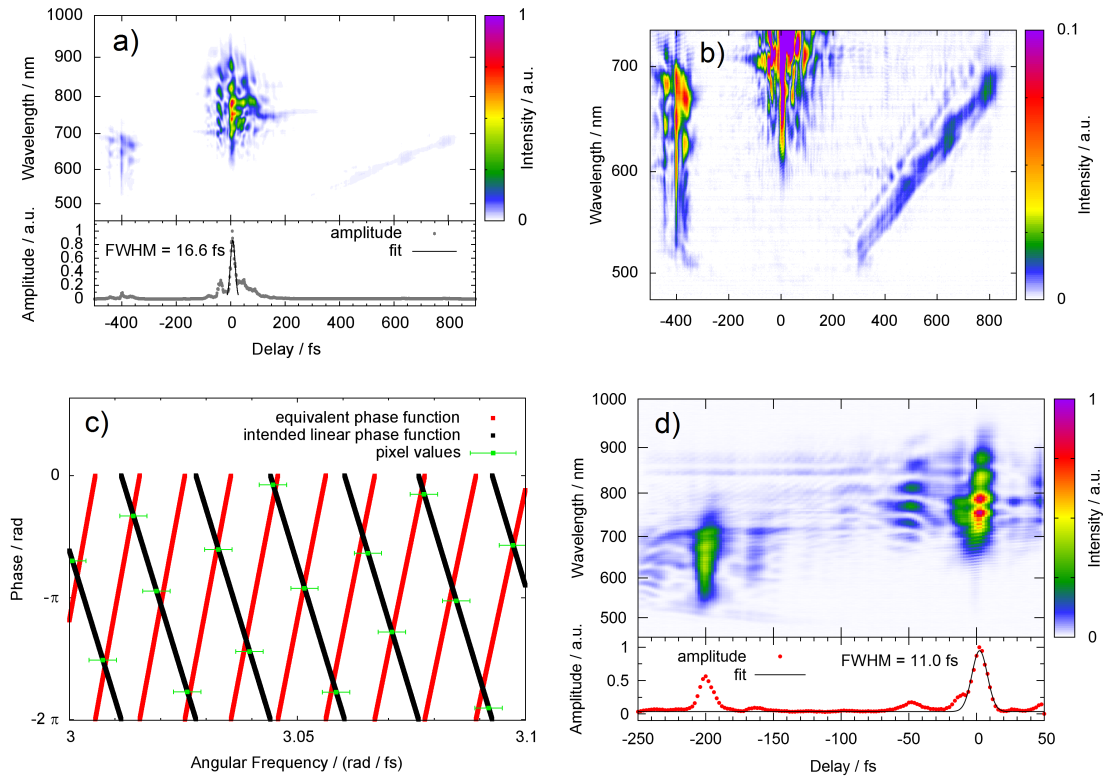


Figure 3.11: a) TG-FROG trace of a double pulse sequence where the VIS part of the spectrum ($\lambda < 700$ nm) is shifted by 400 fs to negative times. The trace shows a sampling replica pulse in the region between +300 fs and +800 fs. b) Zoom-in on the VIS part of the spectrum. The intensity scale is reduced to 0.1 of the maximum intensity, to better show the sampling replica pulse. c) Detailed illustration of the phase function written on the LC-SLM in wrapped representation around 3.05 rad / fs. The green points are the values of the intended linear phase function (black line) sampled by the LC-SLM and the errorbars indicate the spectral width covered by the pixels. An equivalent quadratic phase function (red line, see Table 3.2) is constructed from the parameters of the sampling artifact shown in b). d) TG-FROG trace of a double pulse sequence where the VIS part of the spectrum ($\lambda < 725$ nm) is shifted by 200 fs to negative times. The additional phase functions $\phi_a(\omega)$ for the generation of these pulses are given in Table 3.2.

directly from the replica pulse in the FROG trace, which shows a temporal shift of about +600 fs at 3.05 rad/fs (≈ 617 nm), a shift of 700 fs at 2.89 rad/fs (≈ 650 nm) and a shift of 550 fs at 3.13 rad/fs (≈ 600 nm). From these points, a phase function with the form $\phi(\omega) = b_1(\omega - \omega_0)^2 + b_2(\omega - \omega_0) + b_3$ can be formulated with the parameters $b_1 = -625$ fs², $b_2 = 600$ fs, $b_3 = 0$ and $\omega_0 = 3.05$ rad/fs. The parameters were adjusted slightly to match the function to the points sampled by the LC-SLM, resulting in $b_1 = -550$ fs², $b_2 = 585$ fs, $b_3 = 4.25$. Both functions equivalently represent the spectral phase function written by the LC-SLM and the correspondence to the observed replica pulse illustrates the effects that occur when operating at the limit of the shaping window of the pulse shaper. Fig. 3.11 d) shows a double pulse sequence, where the VIS part of the spectrum ($\lambda < 725$ nm) is shifted by 200 fs to negative times. In this case, the spectral phase function is sampled much better, resulting in a higher intensity

of the shifted part of the pulse. Summarizing it can be stated, that the white-light setup allows for the generation of two-color double pulse sequences with sub-pulse durations below 15 fs and a high accuracy of the sub-pulse delay ($\pm 2\%$). When the IR part of the spectrum is shifted, sub-pulse delays of ± 600 fs are possible. When the VIS part of the spectrum is shifted, the sub-pulse delay should not exceed 200 fs, to avoid sampling problems.

3.7.2 Linearly Chirped Pulses

Fig.	Spectral Range	$\phi_a(\omega)$
3.12 a)	all wavelengths	$+10 \text{ fs}^2 \cdot (\omega - \omega_0)^2$
3.12 b)	all wavelengths	$+100 \text{ fs}^2 \cdot (\omega - \omega_0)^2$
3.12 c)	all wavelengths	$-150 \text{ fs}^2 \cdot (\omega - \omega_0)^2$

Table 3.3: Explicit additional spectral phase functions $\phi_a(\omega)$ for the generation of linearly chirped pulses. $\omega_0 = 3.0 \text{ rad / fs}$.

Linearly chirped pulses are one of the more frequently used pulse shapes in coherent control [21, 112, 113] and were employed for charge reversal experiments on Cu_3 and Al_4 in this work (see sections 6.4 and 7.4). Hence, the performance of the laser setup in generating linearly chirped pulses was tested. The TG-FROG traces of the generated pulses are shown in Fig. 3.12. To show that these pulses are actually linearly chirped, the traces are plotted versus angular frequency, rather than wavelength. Depicted in this way, TG-FROG traces of linearly chirped pulses ideally should look like tilted straight lines or ellipses (see simulation in Fig. 2.12 d)). Fig. 3.12 a) shows a pulse with a positive linear chirp of $\phi'' = +20 \text{ fs}^2$. Even at this small chirp rate, leading to a FWHM duration below 20 fs, the FROG trace shows that the pulse is linearly chirped. Fig. 3.12 b) shows a pulse with a positive linear chirp of $\phi'' = +200 \text{ fs}^2$. The pulse endures for approximately 300 fs and the trace clearly shows the linear chirp. The occurrence of several parallel lines in the trace is a result of the pulses' modulated spectrum, which leads to multiple intensity peaks in the generated pulse. These peaks act as the predominant optical gates and hence each draws its own line in the frog trace. Fig. 3.12 c) depicts a pulse with a negative linear chirp of $\phi'' = -300 \text{ fs}^2$. Again, the trace nicely shows the linear chirp of the pulse. The explicit additional phase functions $\phi_a(\omega)$ employed for the generation of the chirped pulses are given in Table 3.3. Summarizing, it can be stated that the laser setup produces decent linearly chirped pulses.

3.7.3 Pulse Trains

Pulse trains utilize the entire spectrum over the complete duration of the waveform, featuring multiple short sub-pulses, that can be as short as the compressed pulse used as the starting point. Hence, pulse trains are a good test for the temporal resolution and

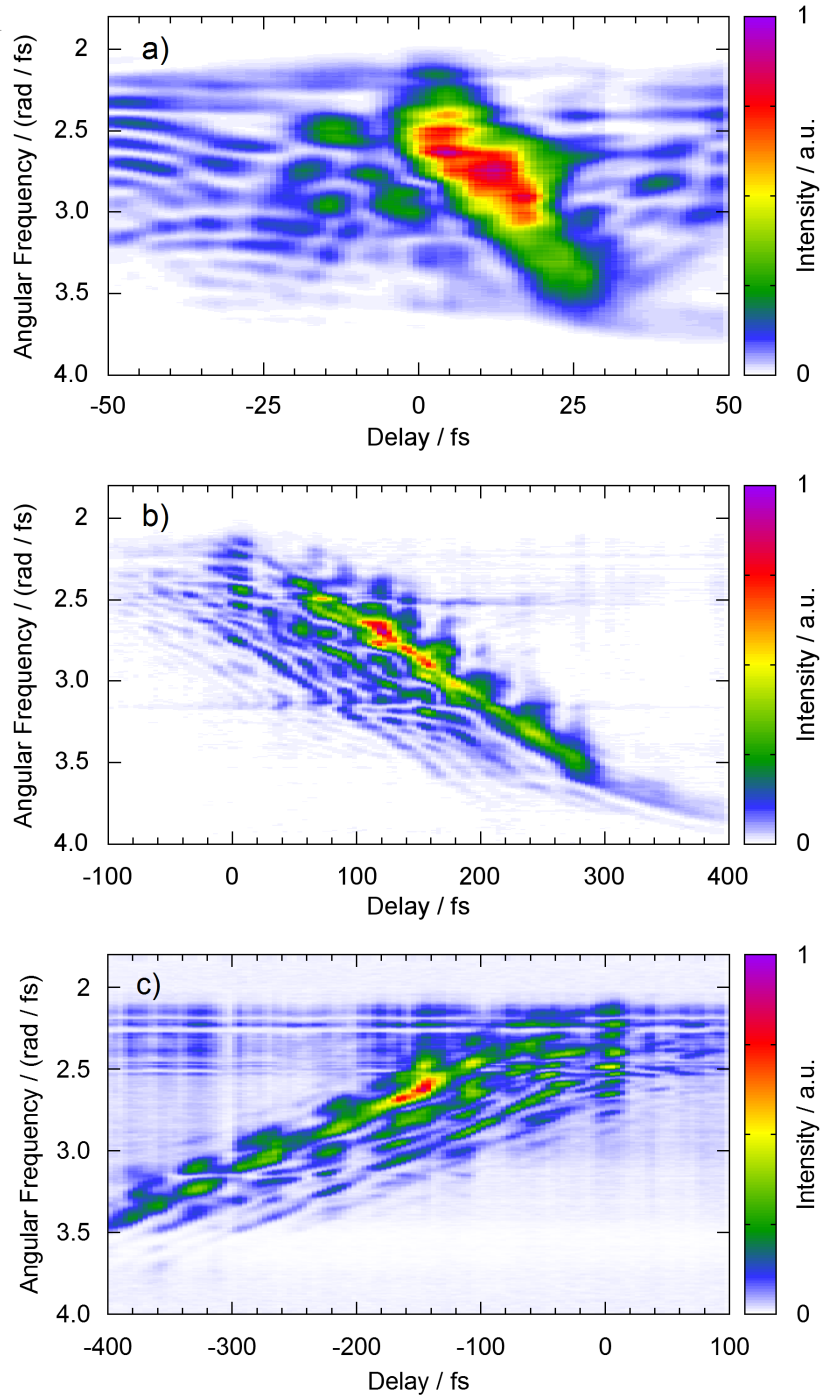


Figure 3.12: TG-FROG traces of linearly chirped pulses. a) Pulse with a positive linear chirp of $+20 \text{ fs}^2$. b) Pulse with a positive linear chirp of $+200 \text{ fs}^2$. c) Pulse with a negative linear chirp of -300 fs^2 . The additional phase functions $\phi_a(\omega)$ for the generation of these pulses are given in Table 3.3.

contrast that can be attained when complex pulses are generated with the pulse shaper. The starting point for pulse train generation was a short pulse compressed using an offset spectral phase function $\phi_{off}(\omega)$ similar to the function given in Table 3.1. Here, pulse-trains are generated via sinusoidal phase modulation, rather than amplitude modulation. The explicit additional spectral phase functions $\phi_a(\omega)$ for pulse train generation are given in Table 3.4. Fig. 3.13 a) shows a TG-FROG trace of a pulse train with a subpulse delay ΔT of 20 fs, generated by applying a sinusoidal spectral phase function with a spectral modulation period ΔT^{-1} of 50 THz. The central peak in the trace, which is the simultaneous correlation of each subpulse with itself, has a FWHM duration of 6.9 fs and the pulse-to-gap contrast is still very good. Some subpulse delays deviate by a few femtoseconds from the intended 20 fs, which might be due to the fact, that the spectrum is modulated and the sinusoidal spectral phase function has only a few periods over the entire bandwidth. Fig. 3.13 b) shows a TG-FROG trace of a pulse train with a subpulse delay ΔT of 50 fs, generated by applying a sinusoidal spectral phase function with a spectral modulation period ΔT^{-1} of 20 THz. For equalizing the spectral intensity, the spectrum of the pulse train in Fig. 3.13 b) ($\Delta t = 50$ fs) was filtered by means of a custom-made beam splitter (Layertec GmbH), which attenuates the most intense part of the spectrum between 750 and 850 nm by 80 % while leaving the rest of the spectrum unaffected, resulting in the spectrum depicted in fig. 3.13 c). The central peak in the trace, which is the simultaneous correlation of each subpulse with itself, has a FWHM duration of 6.3 fs and the pulse-to-gap contrast is very good. The intended 50 fs subpulse delay is met very well.

Summarizing, it can be stated, that for both pulse trains shown, the sub-pulse duration remains below 7 fs, the intended subpulse delays are met and even for a sub-pulse delay of 20 fs the contrast is still very good, confirming the high accuracy of the pulse shaper's calibration.

Fig.	Spectral Range	$\phi_a(\omega)$
3.13 a)	all wavelengths	$2.0 \cdot \sin (20 \text{ fs} \cdot \omega + 4)$
3.13 b)	all wavelengths	$2.2 \cdot \sin (50 \text{ fs} \cdot \omega)$

Table 3.4: Explicit additional spectral phase functions $\phi_a(\omega)$ for the generation of pulse trains.

3.7.4 Summary

An improved white-light laser setup, employing twofold filamentation in air at atmospheric pressure for supercontinuum generation and a pulse shaper for the generation of arbitrary pulse shapes, within the sampling limit of the LC-SLM, and a TG-FROG setup for pulse analysis has been set up. The twofold filamentation spectral broadening section yields a spectrum ranging from 550 nm to above 900 nm at 10 % of the maximum intensity, and runs very stable without the need for frequent readjustments.

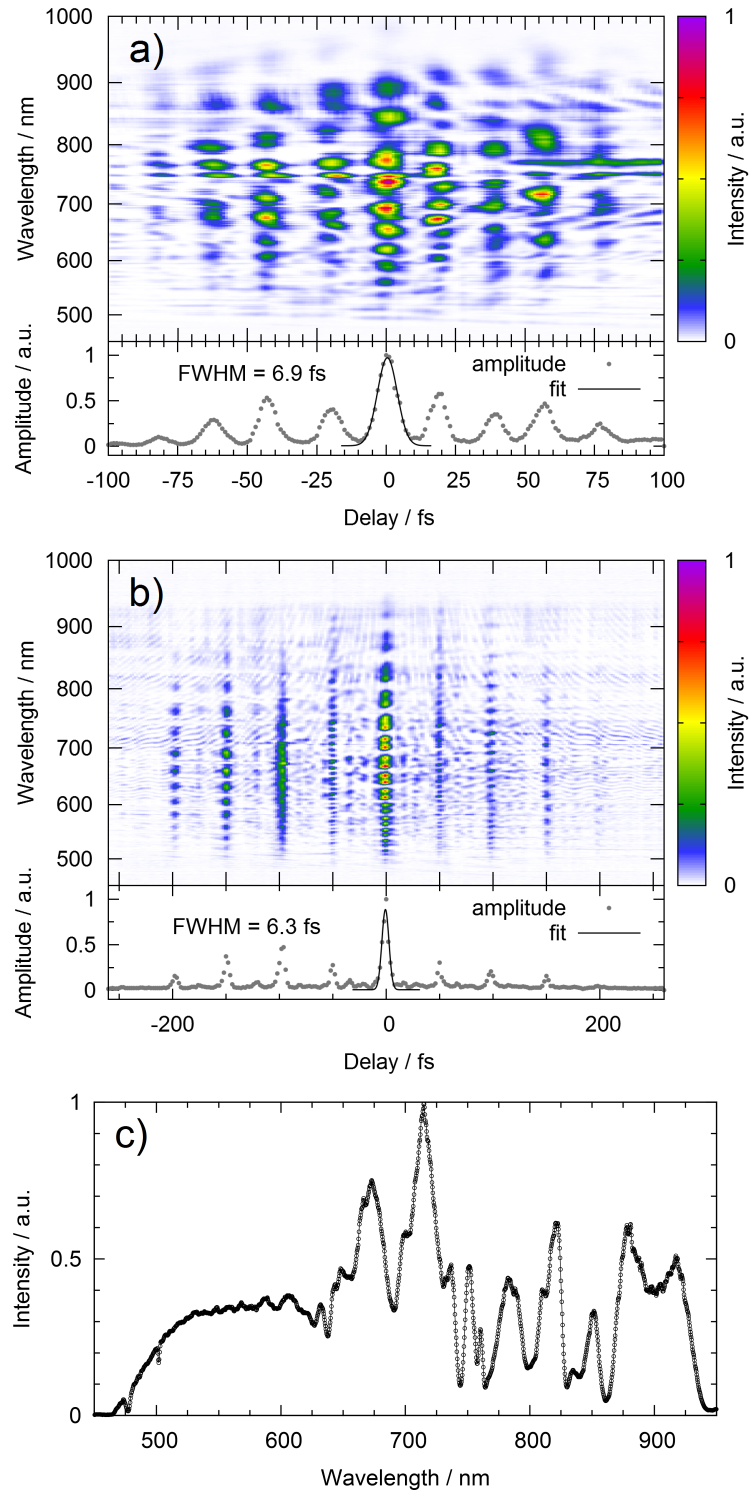


Figure 3.13: TG-FROG traces of pulse trains. a) Pulse train with a sub-pulse delay of 20 fs. b) Pulse train with a sub-pulse delay of 50 fs. c) Spectrum of the pulse train shown in b), where the most intense part of the spectrum (750-850 nm) was reduced by 80 %. The explicit additional spectral phase functions $\phi_a(\omega)$ are given in Table 3.4.

The generated supercontinuum pulses have been compressed to 4.9 fs by means of ultra-broadband chirped mirrors and a pulse shaper setup. For the first time, the generation of a variety of complex supercontinuum pulses featuring few-cycle substructures has been demonstrated. The setup is complemented by a TG-FROG setup that allows for the correlation of supercontinuum pulses extending over hundreds of femtoseconds and feature substructures in the few-cycle regime.

Molecular Beam Apparatus

4

4.1 Overview

All spectroscopic experiments presented in this work have been performed in a home-built molecular beam apparatus [114]. It consists of two parts, the source chamber and the main chamber, that can be separated by a gate valve, to be able to vent the source chamber separately for servicing or exchanging the source. The main chamber houses a hexadecapole ion trap flanked by two quadrupole mass spectrometers. This setup allows for the mass-selection of a desired ionic molecule, storing it in the ion trap to increase the number density for performing an experiment, and mass analysis of the ionic products. Different ion sources can be mounted to the source chamber. Metal clusters are generated in a magnetron sputtering source and biomolecules can be generated by electrospray ionization.

4.2 Ion Guiding Tandem Mass Spectrometer

A scheme of the main vacuum chamber housing the ion optics is depicted in Fig. 4.1. In the main chamber, high vacuum is generated by four turbo molecular pumps (Pfeiffer

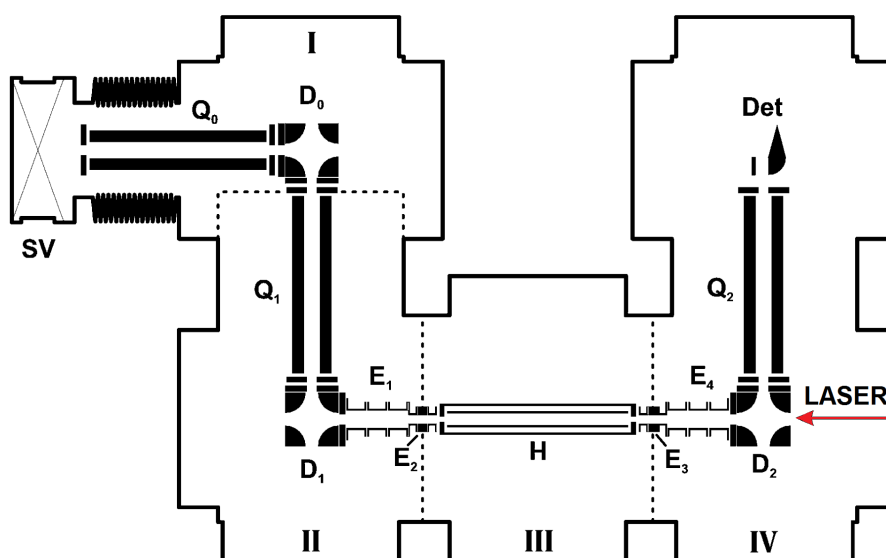


Figure 4.1: Scheme of the main vacuum chamber and the ion optics. The dashed lines indicate internal subdivisions which, to some degree, prevent diffusion of inlet gases to other parts of the chamber. Q_0 : decapole, D_0 : quadrupole deflector, Q_1 : quadrupole mass filter, D_1 : quadrupole deflector, E_{1-4} : einzel lenses, H : hexadecapole ion trap, D_2 : quadrupole deflector, Q_2 : quadrupole mass filter, Det : conversion dynode and channeltron detector. Image adapted from [114].

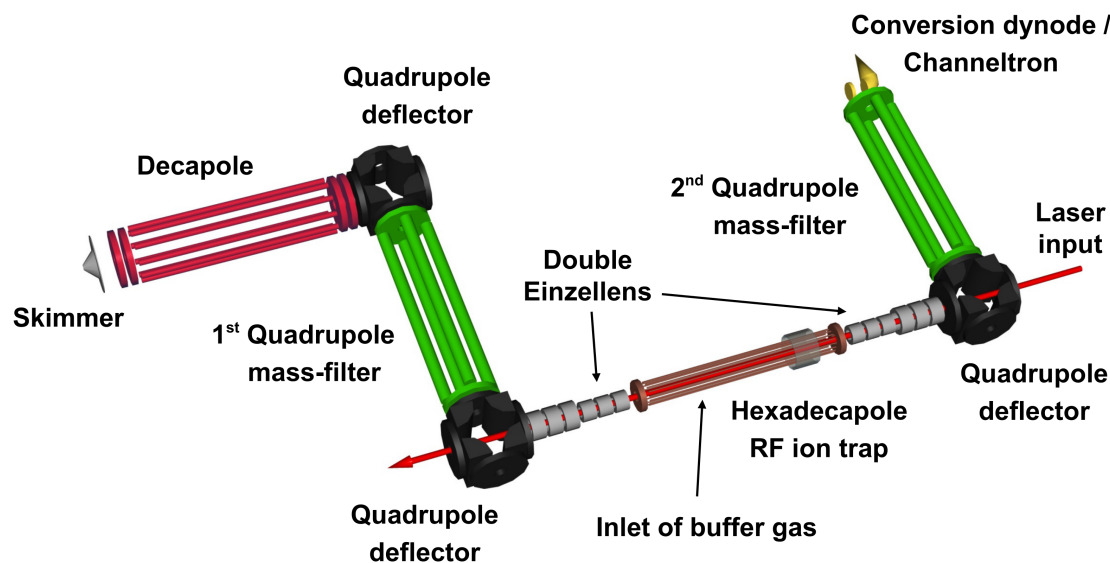


Figure 4.2: 3D rendering of the ion optics of the ion guiding tandem mass spectrometer. See text for details.

Vacuum TMU 521 P, 520 l/s), which are backed by a large rotary vane pump (Pfeiffer Vacuum DUO 65, 65 m³/h). The pressure is around $1 \cdot 10^{-8}$ mbar under non-operating conditions. Ion sources are connected to the source chamber via a large flange. The source chamber is located behind the source chamber gate valve (SV). To cope with the large gas flows injected into the source, the chamber is pumped by a large turbo molecular pump (Pfeiffer Vacuum TMH 1601, 1380 l/s) backed by a rotary vane pump (Edwards E2M18). Under non-operating conditions, the pressure in the source chamber is around $5 \cdot 10^{-7}$ mbar. Ions as well as neutrals generated in the source enter the main chamber via a skimmer. For anions, the skimmer is held on a positive potential by a home-built power supply employing a brandenburg Type 4479-107 photomultiplier module. The ions are then guided by a RF decapole (Q_0) to the first quadrupole deflector (D_1). The decapole can be filled with buffer gas, to act as a phase space compressor [115, 116], which narrows the kinetic energy distribution of the ion beam. The first quadrupole deflector (D_1) deflects ions of the desired charge state 90° and filters out neutrals and ions of the opposite charge. The ions are then guided into the first quadrupole mass filter (Q_1 , ABB Extrel, 880 kHz), where the desired species is selected. The ions are then steered into the RF hexadecapole ion trap via the second quadrupole deflector. The ion trap is powered by a 1.2 MHz power supply (ABB Extrel). The trap is cooled by a cryostat and the ions are thermalized in a helium atmosphere and trapped by repelling potentials applied to the entrance and exit lenses. In the trap, various experiments like chemical reactions or laser irradiation can be performed. After extraction from the trap, the ions are again deflected 90° and are mass-filtered by the second quadrupole mass filter (Q_3 , ABB Extrel, 880 kHz). The detection of the ions is performed by a conversion dynode and a channeltron multiplier (Burle, Model 4873). The conversion dynode is held on a potential of +4 kV for the detection of anions, and on -4 kV for cations (power supply: Extranuclear Laboratories), while the channeltron is held at -2.4 kV (power supply: Fug

HCN14-3500). The output current of the channeltron is amplified by a low noise current amplifier (Femto, DLCPA-200), and ions are counted by means of a counting card (Meilhaus Electronic, ME-14). Laser irradiation of the reactants is achieved by focusing the laser beam into the ion trap. The laser enters the vacuum chamber via a window, passes the trap parallel to the trap axis and exits the vacuum chamber via a second window. For all experiments presented in this work, a 3 mm thick fused silica entrance window was used.

4.3 Hexadecapole Ion Trap

In the ion beam, the ion density is very low. To enable an efficient laser irradiation, the ion density has to be increased, which is achieved by trapping. The home-built trap consists of a hexadecapole made of 16 rods with a diameter of 2 mm and 20 cm length and an entrance and exit lens, housed in a cylindrical enclosure retaining the buffer gas. The trap's housing is attached to the head of a closed-cycle helium cryostat (CTI-Cryogenics, Head 350 CP; Compressor 8200) for cooling. The temperature of the trap can be adjusted from approximately 17 K to 330 K, by means of the cryostat and a heating with temperature controller (Lakeshore). A scheme of the trap is depicted in Fig. 4.3. The upper panel shows a cross section of the trap. The lower panel illustrates the trapping mechanism. Trapping is achieved by applying an RF potential and an attractive DC bias voltage (pole bias) to the hexadecapole rods and repelling electrostatic potentials to the entrance and exit lenses. The potential of the entrance lens is chosen such that the incoming ions have just enough kinetic energy to enter the trap and the exit lens is held at a higher electrostatic potential. After passing the entrance lens, the ions are decelerated by a multitude of collisions with the buffer gas atoms. After being repelled by the exit lens, the ions cannot exit the trap via the entrance lens, as their kinetic energy is too low. The buffer gas flow injected into the trap is controlled by a mass flow controller (1179B, MKS Instruments) to ensure a high stability of the buffer gas pressure and the associated ion signal. The pressure inside the trap is measured with a capacitance manometer (Baratron 627B, MKS Instruments), which measures the pressure directly by means of an Inconel diaphragm. The Baratron controls its temperature at 318 K and is connected to the ion trap enclosure via a thin tube. Due to the temperature difference between trap and Baratron, the pressure measured by the baratron has to be corrected for thermal transpiration according to [118]

$$P_{trap} = P_{Baratron} \cdot \sqrt{\frac{T_{trap}}{T_{Baratron}}}. \quad (4.1)$$

Thermalization of trapped clusters requires a few thousand collisions with the buffer gas atoms, which takes less than 10 ms under common operating conditions where the buffer gas pressure is around 0.01 to 0.03 mbar [117, 119].

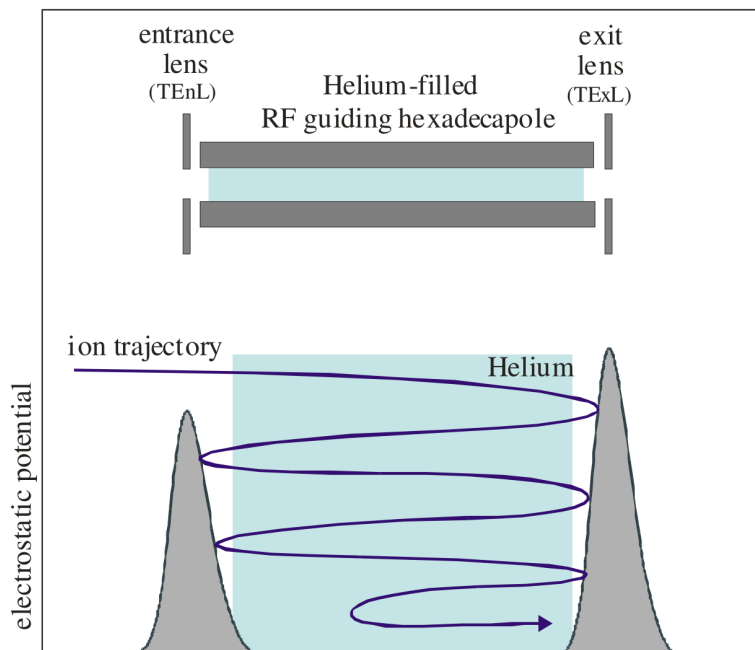


Figure 4.3: Scheme of the home-built RF hexadecapole ion trap. The upper panel shows a cross section of the trap which is filled with helium buffer gas. The lower panel illustrates the trapping mechanism. The entrance lens is held at a repelling electrostatic potential chosen such that the incoming ions have just enough kinetic energy to enter the trap and the exit lens is held at a higher electrostatic potential. After passing the entrance lens, the ions are decelerated by a multitude of collisions with the buffer gas atoms. After being repelled by the exit lens, the ions cannot exit the trap via the entrance lens, as their kinetic energy is too low. Image taken from [117].

4.4 Magnetron Sputtering Source

The generation of metal clusters investigated in the framework of this thesis was performed in a newly built magnetron sputtering source. The sputter head (Torus 2" with strong magnet option) and the high voltage DC power supply (DC01BP) are from Kurt J. Lesker. The sputter head is housed in a home-built enclosure built according to Haberland [121]. The sputter head resides in a cooling cylinder, which can be cooled by liquid nitrogen. The cooling cylinder also retains the injected gases, argon for sputtering and optionally helium for aggregation, to maintain an acceptably low pressure in the source chamber. The sputter head is water-cooled and features a set of bar magnets, a target holder and a ring shaped inlet for the sputter gas. A cross section scheme of the sputter head, illustrating the sputtering process, is depicted in Fig. 4.4. The sputter gas is injected via a mass flow controller (1179B, MKS Instruments) for improved signal stability. Argon is used as sputter gas, as it is inert and contains natural ions due to its relatively low ionization energy (15.8 eV). These ions are needed to initiate the sputtering process. The target is held on a negative potential by the high voltage power supply which accelerates the argon cations onto the target. Upon impact, the argon atoms knock atoms and clusters of the target material and secondary electrons out of the target. Below the target, bar magnets arranged in a ring, together with a central magnet of opposing

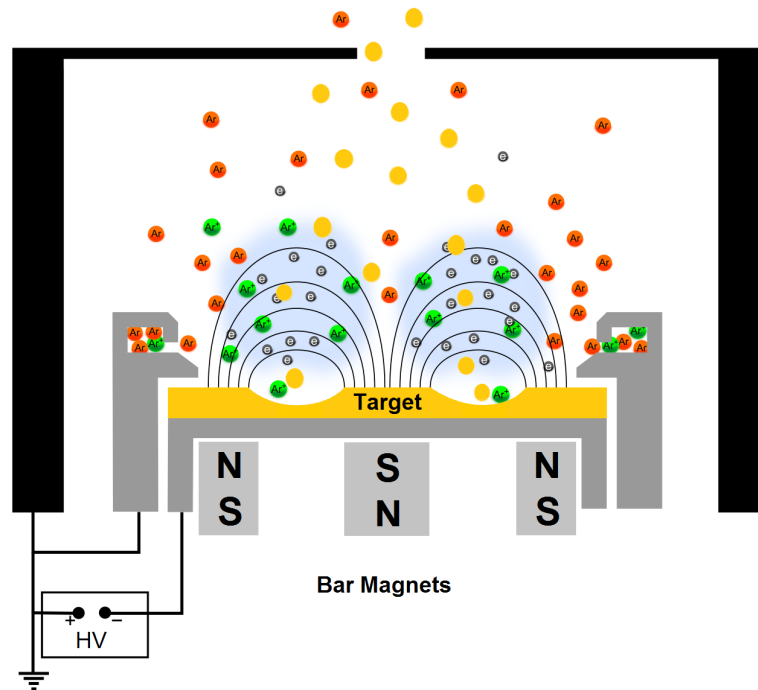


Figure 4.4: Cross section scheme of the sputter head inside the cooling cylinder (black). Bar magnets arranged in a ring, together with a central magnet of opposing orientation, generate a magnetic field indicated by black lines. The sputter target is mounted above the magnets and is connected to the negative pole of a high voltage power supply (HV). From the sides, argon is injected, which contains neutral (red) and some positively charged atoms (green). The argon cations are accelerated onto the target by the high voltage and, upon impact, knock out atoms or clusters of the target material (yellow). Secondary electrons, which enhance the production of more Ar cations, are produced in this process as well. The magnetic field traps the electrons in a region close to the target. Areas of high electron density are indicated by blue color. Image adapted from [120].

orientation, generate a magnetic field that traps the secondary electrons. Hence, a region of high electron density forms close above the target. Neutral argon atoms and sputtered target material atoms and clusters are ionized by collisions with the electrons, further enhancing the sputtering process [122].

Integrated Optimal Control Setup

5

5.1 Temporal Resolution

The white-light laser setup presented in chapter 3 generates 5 fs pulses and, via subtle changes of the spectral phase, the chirp of these pulses can be altered by very small amounts, which is easily detectable with the TG-FROG. Of course, the white-light laser setup was developed for performing coherent control experiments with very high temporal resolution. In order to assess the temporal resolution that can be achieved when performing experiments in the ion trap, pulse shaper-based cross-correlations were performed in the ion-trap, using the multiphoton ionization of xenon as the nonlinear process. Xenon was chosen for these experiments because it does not feature molecular dynamics which could affect the measurement and due to its low ionization energy. Xenon has an ionization energy of 12.1 eV, corresponding to an energy requirement of seven 700 nm photons or eight 750 nm photons. Hence, in a direct nonresonant multiphotonic ionization, the ion signal should increase by a factor of $2^7 = 128$ to $2^8 = 256$ at zero delay during a pump-probe scan, for a 1:1 pulse energy splitting ratio. Although high Rydberg states of xenon atoms have radiative lifetimes in the μs regime [123], long-lived states seem not to play a significant role in these measurements. However, such long-lived states could reduce the observed factor of signal increase at zero delay.

For multiphoton ionization of xenon, the laser was focused into the ion trap by means of a spherical mirror with a focal length of $f = 0.75$ m, and xenon gas was injected into the trap via a mass flow controller. The generated xenon cations were mass-selected by means of the second quadrupole mass filter (Q_2). The cross-correlation scans were performed using only the shaper setup to generate and delay two laser pulses, by Fourier shifting the NIR part of the spectrum. Fig. 5.1 shows a xenon ionization pump-probe scan where the wavelengths above 695 nm were Fourier shifted by means of the pulse shaper with a stepsize of 400 as. The peak at $\Delta\tau = 0$ shows deep fringes due to constructive and destructive interference of pump and probe pulses. The deep, clean fringes show that a stepsize of 400 as is well within the capabilities of the pulse shaper setup. Achieving a perfect spatial overlap of pump and probe pulses is not an issue with shaper-based pump-probe scans and consequently the signal increases by a factor of approximately 100 at $\Delta\tau = 0$. The Xe^+ ion yield was fit with a function of the form

$$f(x) = A \cdot \sin^2(c \cdot (x - d)) \cdot \exp\left(-\frac{(x - m)^2}{2\sigma^2}\right) + o \quad (5.1)$$

with the amplitude A , an oscillating \sin^2 term with the frequency c and phase d , a Gaussian envelope with the center m and standard deviation σ and an offset o . The FWHM of the Gaussian envelope is 9.7 fs. However, this multiphoton ionization cross-correlation

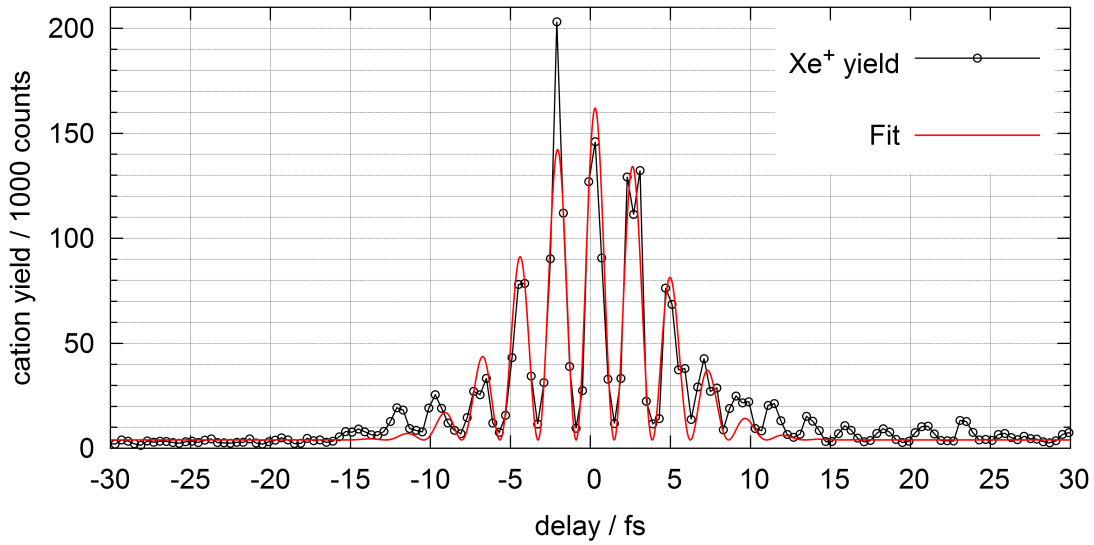


Figure 5.1: Cross-correlation of two laser pulses generated with the pulse shaper setup. The multiphoton ionization of xenon is used as the nonlinear process. Scanning of the delay is performed with the pulse shaper setup by Fourier shifting of the wavelengths above 695 nm with a stepsize of 400 as. The peak at $\Delta\tau = 0$ shows deep fringes due to constructive and destructive interference of the two pulses.

trace is not a common intensity autocorrelation and hence the usual deconvolution factor of $\sqrt{2}$ does not apply here. Assuming that n photons from the first pulse I_1 and m photons from the second pulse I_2 contribute to the multiphoton ionization of a xenon atom, the higher order cross-correlation trace is [49]

$$S_{IntCC}^{higher\ order}(\tau) = \int_{-\infty}^{\infty} I_1^n(t) I_2^m(t + \tau) dt, \quad (5.2)$$

with the delay τ . The FWHM duration of a higher order intensity cross-correlation trace relates to the FWHM durations of the pulses I_1 and I_2 according to

$$\Delta t_{IntCC}^{higher\ order} = \frac{1}{n} \Delta t_1^2 + \frac{1}{m} \Delta t_2^2. \quad (5.3)$$

For the case of an eight-photon process, and if each pulse contributes four photons ($m=n=4$), the observed FWHM duration of the envelope corresponds to a FWHM duration of the pulses I_1 and I_2 of 14 fs. Unequal contributions from both pulses (for example $m=3$, $n=5$), or a seven-photon process (for example $m=3$, $n=4$) would result in shorter durations for the pulses I_1 and I_2 . This result is in line with the pulse durations observed in the double pulse sequences shown in Fig. 3.10. The slightly longer durations are probably due to the longer air path and the vacuum chamber window. As the cross-correlation depicted in Fig. 5.1 actually is interferometric, this analysis is somewhat simplified, however a thorough analysis of a higher order interferometric cross-correlation is beyond the scope of this work.

Summarizing it can be stated, that the pulse shaper setup allows for variations of the pulse shape with an accuracy of 400 as, and this temporal resolution is preserved by the entire experimental setup.

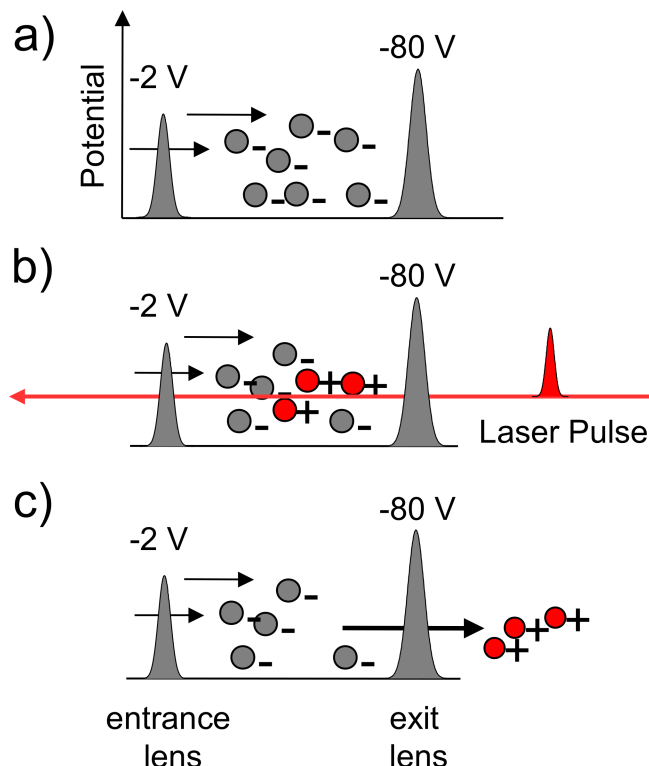


Figure 5.2: Illustration of the charge reversal process. The ion trap potentials remain unchanged. a) The ion trap is continuously filled with anions. The potential of the entrance lens is chosen such that relatively slow anions can enter the trap, but just high enough so that no significant amount of anions can re-exit the trap the same way. b) The laser is focused into the ion trap. Upon excitation by a laser pulse, some anions are converted into cations. c) Cations are extracted via the exit lens, which, for cations, is on a strongly attractive potential.

5.2 NeNePo / Charge Reversal

A main subject of this work is the optimal control of charge reversal, or NeNePo (Negative to Neutral to Positive) processes. Charge reversal refers to a process during which an anion is converted into a cation by laser irradiation. Mostly, a charge reversal process is regarded as a subsequent electron photodetachment and multi photonic ionization. Through vertical electron photodetachment, the neutral ground as well as excited states can be accessed without limitations by spin and symmetry selection rules [48, 124, 125]. Hence, charge reversal is a femtosecond spectroscopy technique spanning three charge states, allowing one to probe the wave packet dynamics of mass-selected neutral clusters on the ground- as well as excited-state potential energy surfaces. The photodetachment can be single photonic or multi photonic, depending on the detachment energy and available photon energies. Fig. 5.2 illustrates how a charge reversal experiment is performed in the ion trap (see section 4.3). As shown in Fig. 5.2 a), the trap is continuously filled with anions of interest via the entrance lens, which is on a repulsive potential of -2 V relative to the pole bias, the DC bias voltage applied to the hexadecapole rods. The pole bias usually is around +10 V during charge reversal experiments. As shown in Fig. 5.2

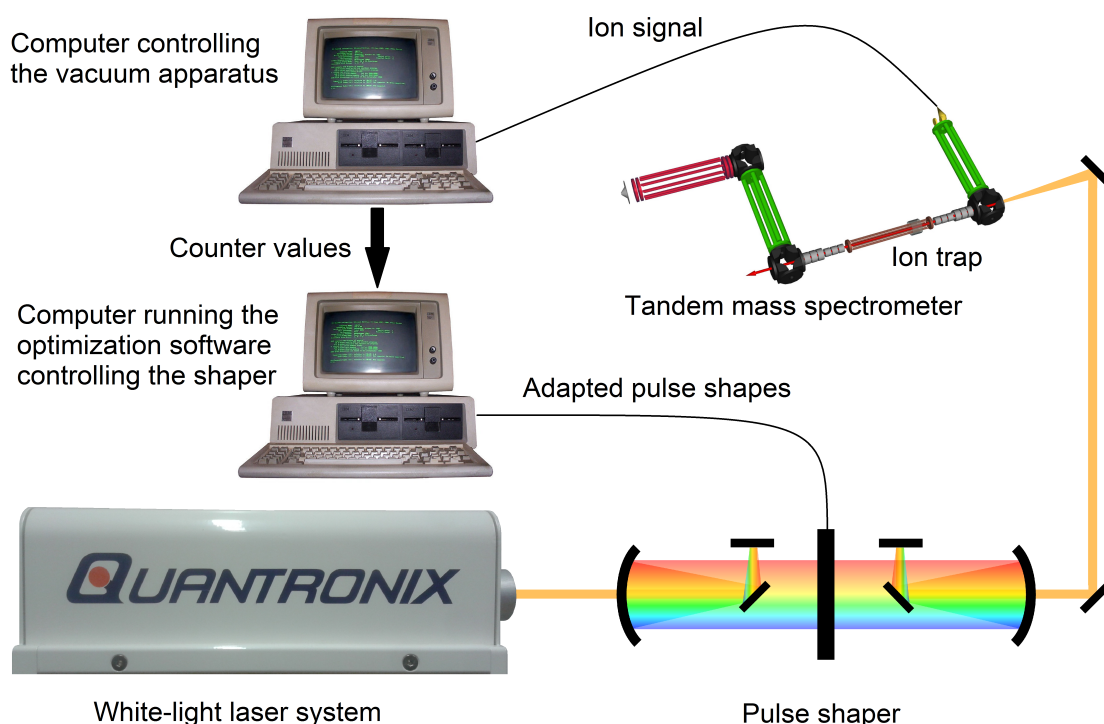


Figure 5.3: Scheme of the optimal control loop. One computer controls the tandem mass spectrometer, counts the ions of one or several masses and passes the counter values to the computer running the optimization software. The optimization software evaluates the fitness of the laser pulses and generates spectral phases of adapted pulses, which are written onto the LC-SLM in the pulse shaper. The pulse shaper shapes the white-light pulses generated by the laser setup. The shaped pulses are focused into the ion trap inside the tandem mass spectrometer, generating the ion signal. The generated ions are mass-analyzed and detected.

b), the laser is focused into the ion trap and each laser pulse converts some anions into cations. The generated cations are extracted via the exit lens, which, for cations, is on a strongly attractive potential of around -80 V relative to the pole bias (see Fig. 5.2 c)). After extraction, the generated cations are mass analyzed in the second quadrupole mass filter.

5.3 Optimal Control Loop

For performing optimal control experiments, the pulse shaper inside the white-light laser setup, the tandem mass spectrometer and the computers controlling the tandem mass spectrometer and the pulse shaper are integrated into an adaptive feedback loop as shown in Fig. 5.3. The computer controlling the optimization software also controls the LC-SLM in the pulse shaper setup. The optimization software generates spectral phase functions and writes them onto the LC-SLM. White-light pulses generated in the white-light laser setup are shaped in the pulse shaper setup and are focused into the ion trap inside the tandem mass spectrometer. Upon laser irradiation, atoms or molecules in the

ion trap are ionized. Molecules can be fragmented as well. Product ions are extracted from the trap for mass analysis in the second quadrupole mass filter and detection. If the ratio of two product ions is supposed to be optimized, the second quadrupole mass filter is switched between the two respective masses, such that the signal of both product ions is measured for each generated laser pulse. The ion signal is passed to the computer controlling the tandem mass spectrometer, where the ions are counted. The obtained counter values are passed to the computer running the optimization software, so the fitness of each generated laser pulse can be evaluated. Based on the fitness values of all laser pulses of one generation, the optimization software creates a new generation of laser pulses.

5.4 GDD+GD Parametrization

In order to perform an efficient evolutionary optimization, it is very advantageous to have a routine that generates only useful laser pulses, featuring a peak intensity sufficient for producing a well measurable charge reversal cationic signal. At the same time, the routine should be able to provide near-arbitrary pulses with no more constraints than necessary. These goals were achieved with the development of the GDD+GD parametrization routine, described in more detail below. It provides steady phase functions complying with the sampling limit of the pulse shaper setup, by limiting the slope of the phase function such that the phase difference of two adjacent pixels $\delta\phi \ll \pi$. These phase functions are generated by the following algorithm: the pixel range of the SLM is divided into 30 equal divisions and two independent parameters, one for group delay (GD) and one for group delay dispersion (GDD), are assigned to each division, as shown in figure 5.4 a). Both parameter functions are numerically singly (GD) and doubly (GDD) integrated in order to obtain two steady phase functions ϕ_{GD} and ϕ_{GDD} , respectively, shown in figure 5.4 b). Summation of both phase functions yields a new phase function, also depicted in figure 5.4 b), that contains information on both the GD and GDD of the output pulse. In order to avoid optimization artifacts stemming from the irregular phase caused by the ultra-broadband chirped mirrors, the offset phase $\phi_{off}(\omega)$ required for pulse compression is added to each generated phase function. $\phi_{off}(\omega)$, $\phi_{GD} + \phi_{GDD}$ as well as their sum are shown in figure 5.4 c). Finally, to optimize the sampling of the generated phase function, i.e. to minimize the phase difference of adjacent pixels $\delta\phi$, the maximum slope of the phase function is minimized by subtracting a linear fit of the phase function from it (see figure 5.4 d)). The 60 pulse parameters obtained in this way are optimized using an evolutionary algorithm as described in the Ph.D thesis of Stefan Weber [126] considering 30 individuals per generation.

5.5 Offset Phase Correction

Numerous attempts to optimize the charge reversal of Al_3^- were performed prior to the implementation of the offset phase correction. Al_3^- anions were generated in the magnetron sputtering source, mass-selected in the first quadrupole mass filter, and stored in

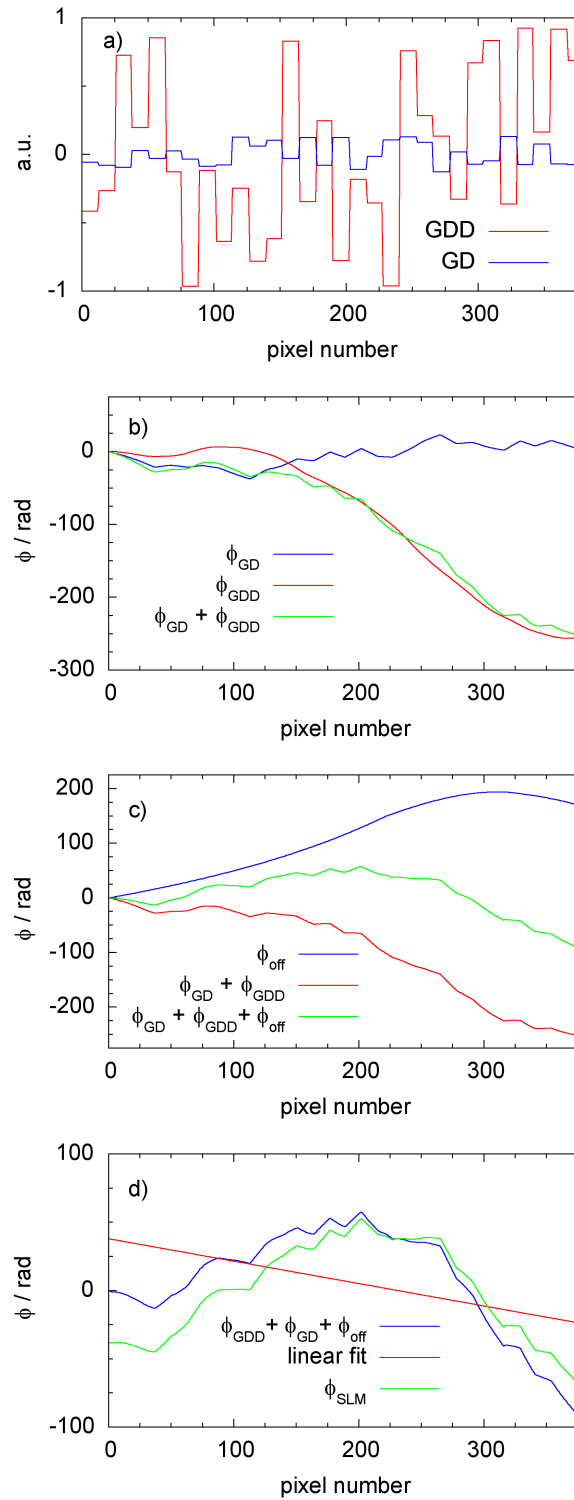


Figure 5.4: Example for the generation of a phase function by the GDD+GD-algorithm. a) Independent GD and GDD assigned to each of the 30 divisions of the pixel range. b) Phase functions ϕ_{GD} and ϕ_{GDD} obtained by numerical single and double integration of the GD and GDD parameter functions shown in a). Both phase functions are summed up. c) The offset phase ϕ_{off} and $\phi_{GD} + \phi_{GDD}$ are summed up. d) Finally the phase function $\phi_{off}(\omega) + \phi_{GD} + \phi_{GDD}$ is fit with a linear function and the linear fit function is subtracted to optimize the sampling, which yields the final phase function ϕ_{SLM} .

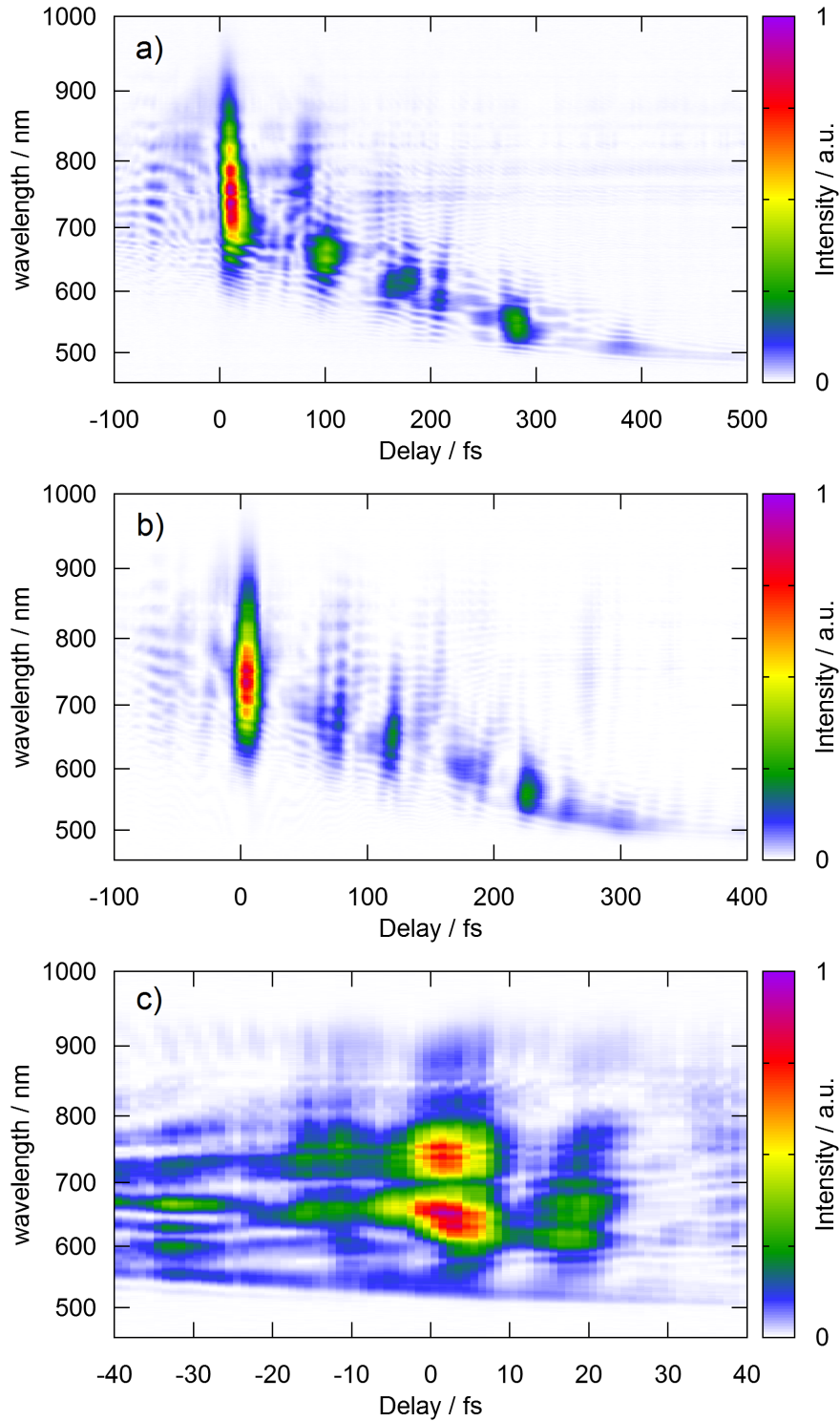


Figure 5.5: Pulses optimized for the charge reversal of Al_3^- featuring artifacts. a) and b) The optimized pulses feature three sub-pulses (disregarding the sub-pulse at 175 fs) which have roughly the same wavelength ranges as the three parts of the offset phase function ϕ_{off} . c) The pulse has an intensity dip at 700 nm, where the pre-compressed pulse changes its chirp (see Fig. 3.5 b)).

the ion trap which was cooled to 20 K. The intense NIR part of the laser spectrum from 750 to 850 nm was attenuated by means of an 800 nm 66 % beam splitter and the laser pulses were focused into the ion trap with a concave mirror ($f=0.75$ m). The optimizations were performed using the GVD+GD parametrization, prior to the implementation of the correction of the offset phase.

TG-FROG traces of three pulses optimized for the charge reversal of Al_3^- are depicted in Fig. 5.5. At first glance, these pulse shapes seemed interesting, but often the sub-pulses had about the same wavelength ranges as the three parts of the offset phase function $\phi_{\text{off}}(\omega)$ given in Table 3.1. The pulses shown in Figs. 5.5 a) and b), look very similar, featuring a short, strong NIR pulse and two more sub-pulses, one between 600 and 700 nm and one between 500 and 600 nm at later times. Both pulses also feature some lesser sub-pulses. Fig. 5.5 c) shows a TG-FROG trace of a pulse optimized for the charge reversal of Al_3^- , which is more or less compressed into one short pulse, but it features a pronounced intensity dip slightly above 700 nm, where the chirp of the pre-compressed pulse, shown in Fig. 3.5 b), changes strongly. These and many more similar optimized pulses led to the conclusion, that a correction of the irregular spectral phase of the pre-compressed pulses has to be performed, in order to run the optimization routine undisturbed by these irregularities in the spectral phase. Hence, the addition of the offset phase $\phi_{\text{off}}(\omega)$, needed for compression of the pulses in the ion trap, was implemented, as described in section 5.4.

After the implementation of the addition of the offset phase $\phi_{\text{off}}(\omega)$, optimized pulses as shown in Fig. 5.5 did not reoccur. Rather, optimizations of the charge reversal of Al_3^- thereafter yielded relatively clean, short pulses as shown in Fig. 5.6, which is a plausible result for a highly nonlinear process and considering that the Al_3^- , Al_3 and Al_3^+ clusters feature near-identical triangular ground-state geometries [127]. The charge reversal of Al_3^- requires at least 7.8 eV or five 700 nm photons, as Al_3^- has an electron affinity of at least 1.4 eV and the ionization potential (IP) of Al_3 is at least 6.42 eV [128, 129, 130]. This led to the conclusion, that the pulse shapes shown in Fig. 5.5 likely are artifacts caused by the irregular phase of the pre-compressed pulses.

5.6 Optimal Pulse Electric Field Determination

Simulation and understanding of the interaction of the optimized pulses with the molecular systems under investigation requires the knowledge of the optimized pulse's electric field $E(t)$. The measurement of the electric field $E(t)$ for such complex pulses with nearly octave-spanning bandwidths is very difficult. However, due to the proper calibration of the pulse shaper setup, demonstrated in section 3.7 and the knowledge of the offset phase $\phi_{\text{off}}(\omega)$, the spectral phase of the optimized pulses $\phi_{\text{opt}}(\omega)$ can be calculated. For this purpose, the offset phase $\phi_{\text{off}}(\omega)$ has to be subtracted from the phase written on the LC-SLM, $\phi_{\text{SLM}}(\omega)$:

$$\phi_{\text{opt}}(\omega) = \phi_{\text{SLM}}(\omega) - \phi_{\text{off}}(\omega). \quad (5.4)$$

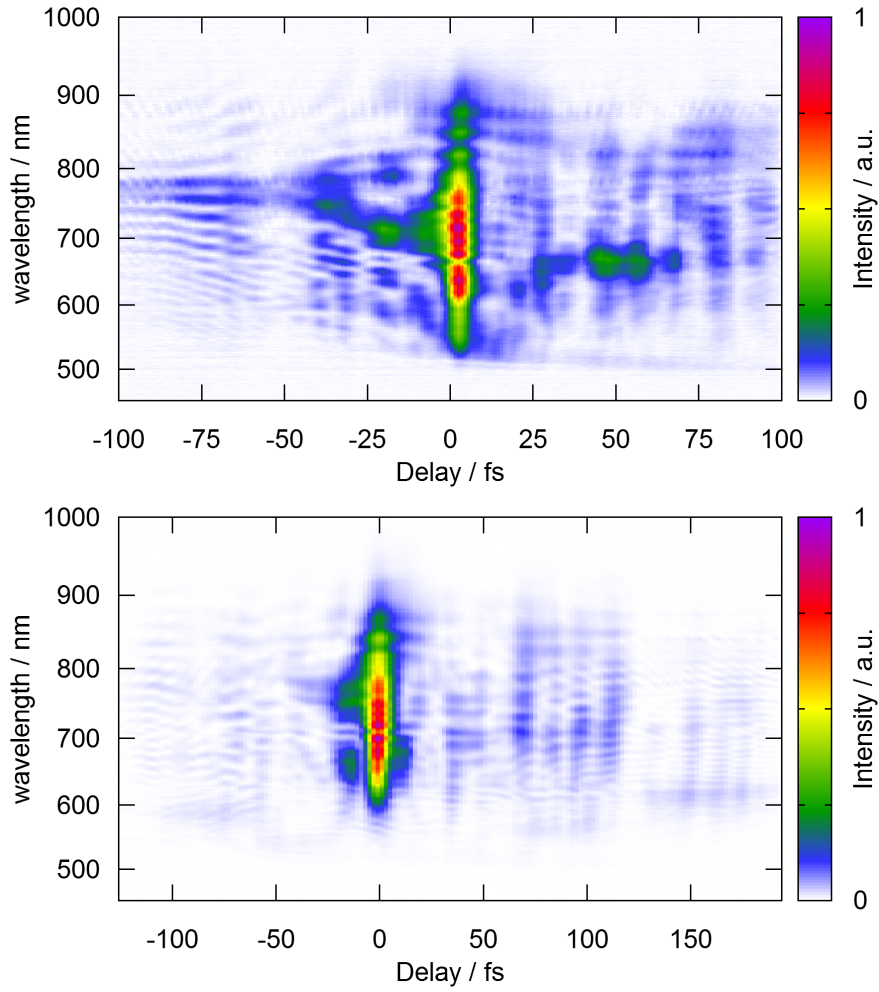


Figure 5.6: Pulses optimized for the charge reversal of Al_3^- , after implementation of the offset phase correction.

Hence, together with the measurement of the spectrum $I(\omega)$, the electric field of the optimized pulse in the frequency domain $\tilde{E}^+(\omega)$ can be calculated by [49]:

$$\tilde{E}^+(\omega) = \sqrt{\frac{\pi}{\varepsilon_0 c n}} \sqrt{I(\omega)} e^{-i\phi_{opt}(\omega)}. \quad (5.5)$$

The temporal electric field $E^+(t)$ can be obtained by Fourier transforming $\tilde{E}^+(\omega)$ according to:

$$E^+(t) = \frac{1}{2\pi} \int_{-\infty}^{\infty} \tilde{E}^+(\omega) e^{i\omega t} d\omega. \quad (5.6)$$

As plots of $E(t)$ are unspecific in showing the occurrence of different light frequencies over time, these are not shown in this work. Rather, the calculated intensity $I(t) = E(t)E^*(t)$ and calculated TG-XFROG traces[106] of the optimized pulses are shown. To obtain the latter, the electric field $E^+(t)$ is multiplied with a gate function $G(t - \tau)$, Fourier transformed, and the square of the absolute value is calculated to obtain the spectrum $I(\omega, \tau)$ at time τ :

$$I(\omega, \tau) = \left| \int_{-\infty}^{\infty} E^+(t) \cdot G(t - \tau) e^{-i\omega t} dt \right|^2. \quad (5.7)$$

In order to resolve the short features of the optimized pulses obtained for the charge reversal and fragmentation of Cu_3^- and Al_4^- , a Gaussian function with a FWHM duration of 8 fs was chosen as the gate function $G(t - \tau)$ for those pulses.

Experiments on the Copper Trimer

6

6.1 Introduction

To survey the potential of the new white-light laser setup described in chapter 3 in the optimal control of photo-induced processes, the charge reversal of Cu_3^- anions with tailored white-light pulses is investigated. Specifically, the ratio ($\text{Cu}_2^+ / \text{Cu}_3^+$) of the yields of the product cations Cu_2^+ and Cu_3^+ is maximized by an EA in a closed feedback loop experiment as described in section 2.5.1. As delineated in the introduction (chapter 1), the white-light laser setup is expected to widen the range of control mechanisms available for optimal control; with the broad range of wavelengths, the population of multiple low-lying electronic states is possible, enabling the initiation of electronic wavepackets comprised of these states. Moreover, due to the few-cycle duration of tailored subpulses in conjunction with the precise control of the spectral phase (see section 5.1), probing of electronic wavepackets becomes feasible. The density functional theory (DFT)-calculated structures of the Cu_3^- anion, the neutral Cu_3 cluster and the Cu_3^+ cation are depicted in Fig. 6.1. The Cu_3^- anion has a linear structure, while the neutral Cu_3 cluster and the Cu_3^+ cation have a triangular structure [131]. Owing to the largely different structures of the Cu_3^- anion and the neutral Cu_3 cluster, the neutral Cu_3 cluster will not be in its ground state after electron photodetachment of the Cu_3^- anion as the instable linear structure of the neutral cluster will lead to molecular dynamics. However, no literature on this process is available at the time being.

6.2 Cu_3^- Cluster Preparation

Cu_3^- cluster anions are generated by sputtering a copper target in the magnetron sputtering source described in section 4.4. The argon gas used for sputtering is injected via a mass flow controller at a flow rate of approximately 8 sccm. The sputtering power usually is around 20 W. The generated ions enter the main chamber via the skimmer

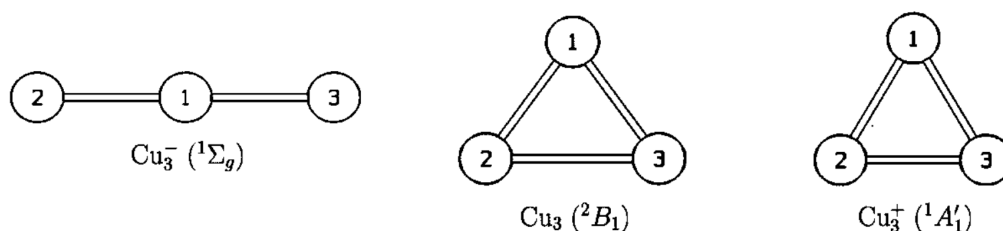


Figure 6.1: Structures of the copper trimer anion, the neutral copper trimer and the copper trimer cation. Image taken from [131]

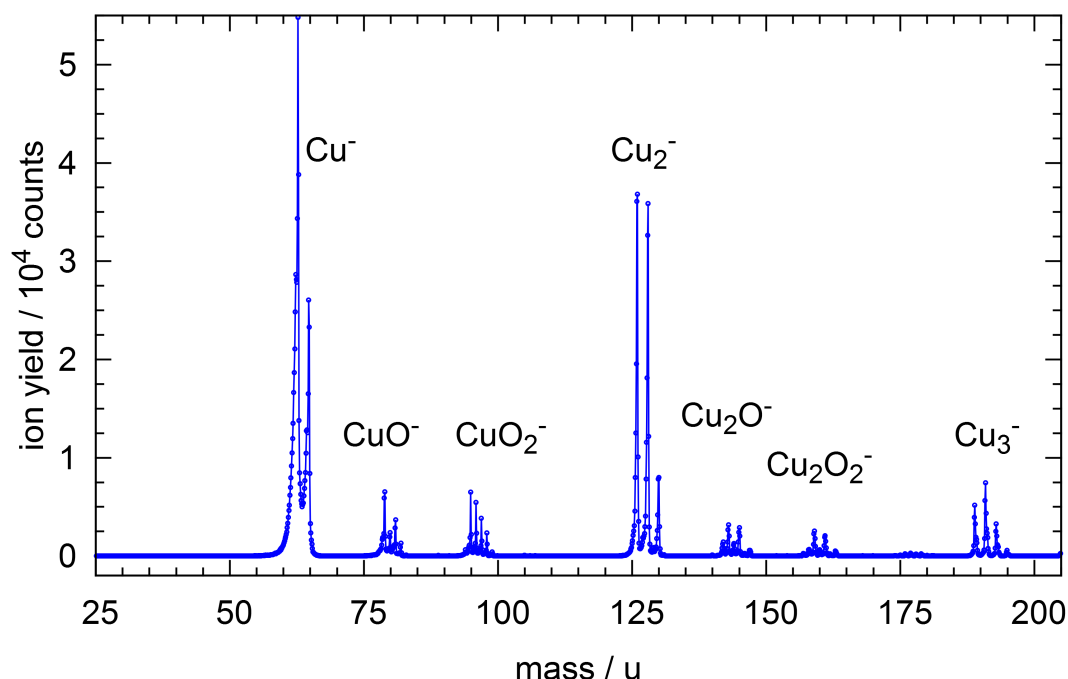


Figure 6.2: High resolution mass spectrum of copper cluster anions and their oxides generated in the magnetron sputtering source. Some oxides contain a hydrogen atom as well. The mass scan was performed in the first quadrupole mass filter Q_1 (see Fig. 4.1).

which is held at an attractive potential of +200 to +300 V. Fig. 6.2 shows a high resolution mass spectrum of the anionic clusters generated under these conditions. Cu^- (63 and 65 u), Cu_2^- (126, 128 and 130 u) and Cu_3^- (189, 191, 193 and 195 u) are observed and their isotope distributions are well resolved. The oxides CuO^- , CuO_2^- , Cu_2O^- and Cu_2O_2^- are observed as well. Some oxides also contain a hydrogen atom, most probably due to contamination of the source chamber with water caused by a previous unrelated experiment. More importantly, the Cu_3^- clusters do not contain hydrogen, which would be difficult to filter out.

For performing charge reversal experiments (see section 5.2), the Cu_3^- cluster anions are mass selected in the first quadrupole mass filter and trapped in the ion trap. The trap is filled with helium buffer gas (6.0, Linde AG) at a pressure of 0.03 mbar and is cooled to 20 K. Cooling increases the number of ions that can be trapped and ensures that the ions are in their vibrational ground state after thermalization. Fig. 6.3 shows a mass scan of Cu_3^- cluster anions which were trapped in, and extracted from the ion trap. For this, Cu_3^- cluster anions were mass-selected in the first quadrupole mass filter Q_1 (see Fig. 4.1) and the mass scan was performed in the second quadrupole mass filter Q_2 . The mass scan shows that no fragmentation of the Cu_3^- cluster anions occurs during trapping or extraction from the trap.

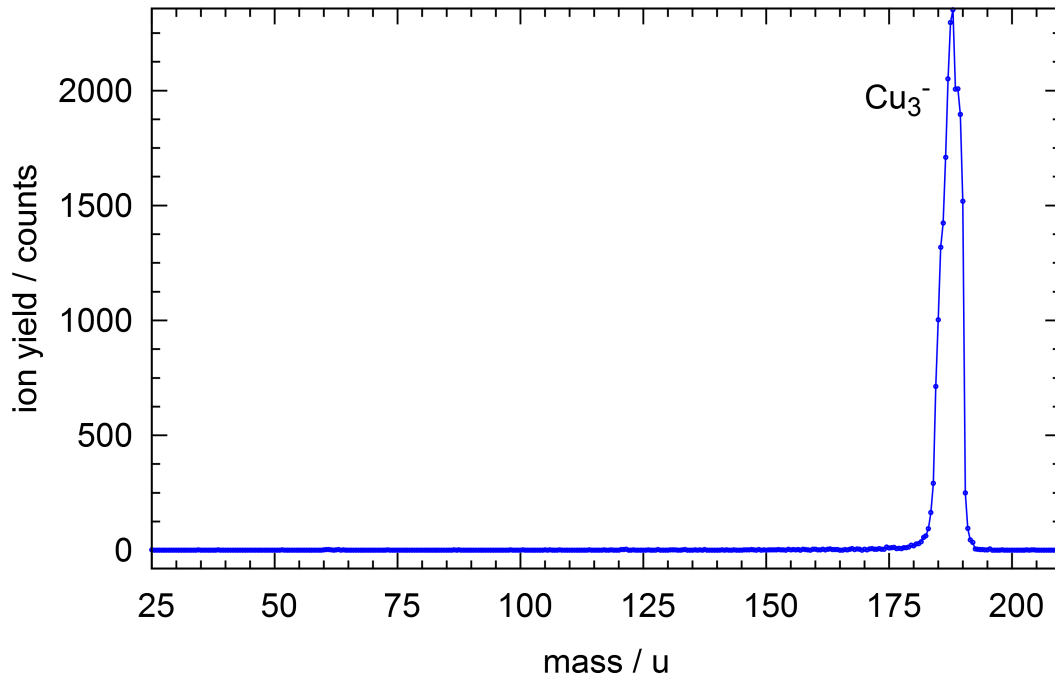


Figure 6.3: Mass spectrum of Cu_3^- cluster anions trapped in the ion trap at 20 K. No fragmentation occurs during trapping or extraction from the trap.

6.3 White-Light Pulse Generation

The White-light laser pulses employed for charge reversal experiments are generated with the setup described in chapter 3. In order to equalize the intensity of the spectral components, the high intensity in the NIR region from 750 to 850 nm is attenuated by means of a 66 % 800 nm beam splitter. A typical spectrum obtained after two filamentation stages in air at atmospheric pressure and attenuation of the NIR spectral region measured after the pulse shaper setup is shown in Fig. 6.4 a). The white-light pulses were always compressed to 7 fs FWHM or less. The pulse energy was 20 μJ for all charge reversal experiments and the pulses are focused into the ion trap with a concave mirror with a focal length of 0.75 m. This results in an approximate peak intensity of $5 \cdot 10^{13} \text{ W/cm}^2$. A TG-FROG trace of a typical short pulse compressed for experiments in the ion trap, measured after propagation through an equivalent air path and vacuum chamber window, is shown in Fig. 6.4 b). The offset phase ϕ_{off} written on the LC-SLM for compression of the pulses at the location of the ion trap is slightly readjusted on a daily basis, as small variations of the spectral phase can occur due to minor temperature changes, shifts in the central wavelength of the oscillator or atmospheric pressure changes.

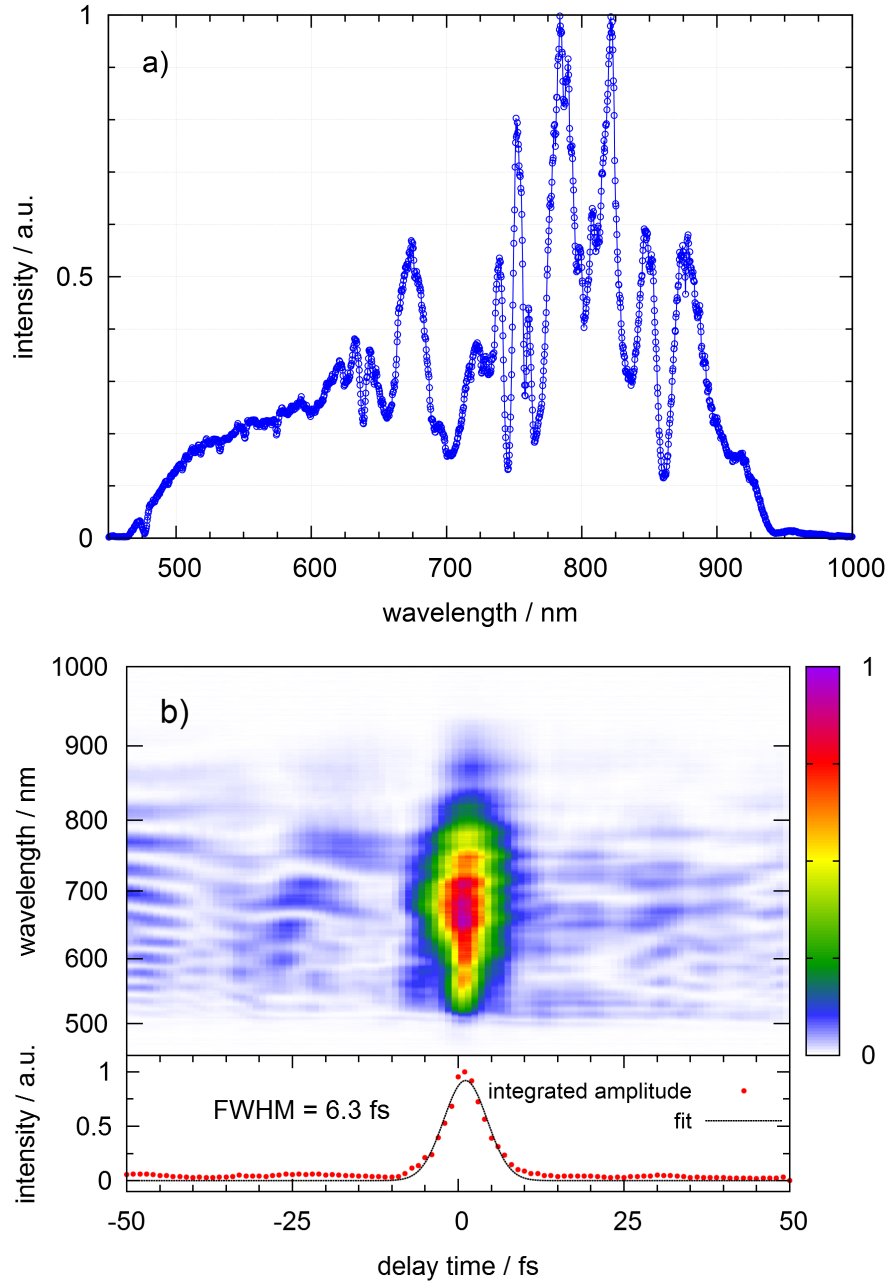


Figure 6.4: a) Typical spectrum obtained after two filamentation stages in air at atmospheric pressure and attenuation of the NIR spectral region measured after the pulse shaper setup. b) TG-FROG trace of a typical short pulse compressed for experiments in the ion trap, measured after propagation through an equivalent air path and vacuum chamber window.

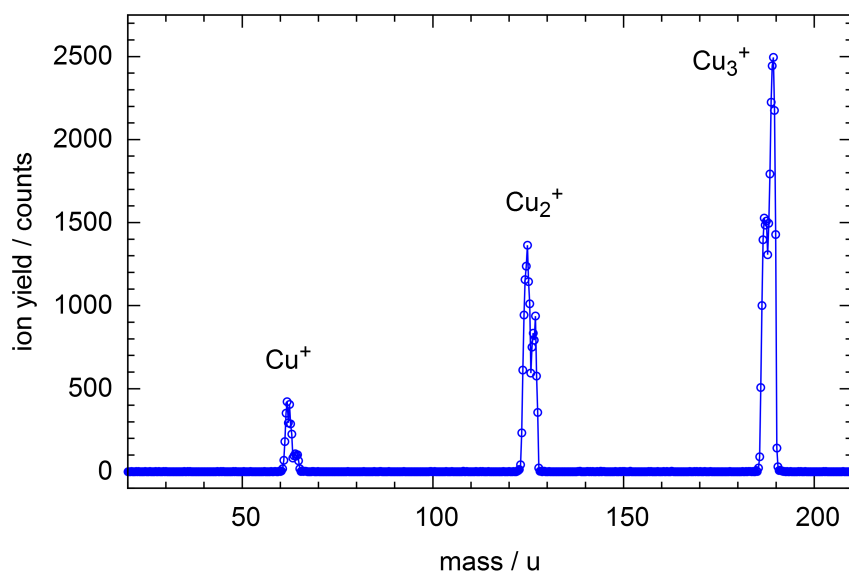


Figure 6.5: Mass spectrum of the Cu_n^+ ($n = 1-3$) product cations generated in a charge reversal experiment, starting from Cu_3^- anions that were irradiated with $20 \mu\text{J}$, 7 fs white-light laser pulses.

6.4 Cu_3^- Charge Reversal Experiments

The charge reversal experiments on Cu_3^- anions were performed by irradiating the trapped and thermalized anions with short as well as shaped white-light pulses. The trap temperature was always kept at 20 K. Laser induced decomposition (LID) measurements (see section 6.7) revealed that Cu_3^- anions fragment into Cu^- anions when irradiated with pulses containing wavelengths shorter than 540 nm. In order to make sure that the charge reversal process always starts with a Cu_3^- anion, wavelengths shorter than 540 nm were blocked for all the charge reversal experiments on the Cu_3^- anion, to avoid photo-fragmentation of the parent anion into Cu^- . A typical cationic mass spectrum obtained by irradiating the trapped Cu_3^- anions with 7 fs short white-light laser pulses is shown in Fig. 6.5. The strongest mass peak is observed for the Cu_3^+ cations generated through direct charge reversal of the Cu_3^- anions. Significant ion yields are also observed for the Cu_2^+ and Cu^+ fragment cations resulting from the photodissociation of the trimer.

For exploring the fragmentation mechanism, a linear chirp scan, where ϕ'' was scanned from -400 fs^2 to 400 fs^2 while monitoring all three cationic photo-product signals, was performed and is depicted in Fig. 6.6. As the charge reversal is a highly nonlinear process (vertical electron detachment energy (VDE) $\text{Cu}_3^- = 2.37 \text{ eV}$ [132], IP $\text{Cu}_3 = 5.8 \text{ eV}$ [133]), the strongest ion yield is observed for $\phi'' = 0 \text{ fs}^2$ where the peak intensity of the pulses is highest and decreases with ascending negative and positive chirp, owing to the lower peak intensities. Interestingly, the $(\text{Cu}_2^+ / \text{Cu}_3^+)$ ratio changes considerably with the chirp. As observed in Fig. 6.6, this ratio equals 0.6 for $\phi'' = 0 \text{ fs}^2$ and it changes to 1.0 for negative chirps larger than $\phi'' = -70 \text{ fs}^2$, while the ion yield remains on a fairly

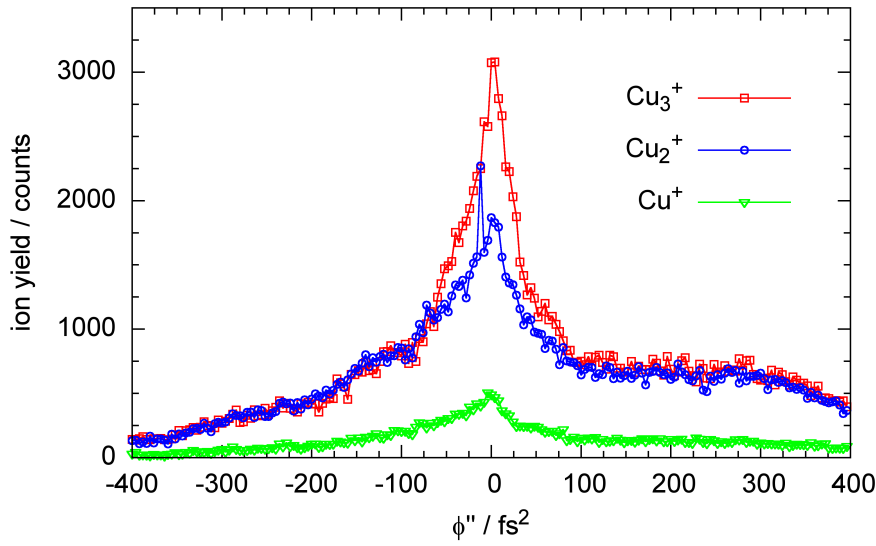


Figure 6.6: Cu_3^- charge-reversal linear chirp scan from -400 to +400 fs^2 . The Cu_3^+ (red line with square symbols), Cu_2^+ (blue line with circles), and Cu^+ (green line with triangles) cation yields are monitored.

high level. A similar ($\text{Cu}_2^+ / \text{Cu}_3^+$) ratio of 1.0 is also observed for positive chirps larger than 100 fs^2 .

6.5 Optimal Control of the Cu_3^- Charge Reversal Process

In order to survey the possibilities in attaining selectivity within the Cu_3^- charge reversal process, maximizing the ($\text{Cu}_2^+ / \text{Cu}_3^+$) product ion yield ratio was chosen as the target for an evolutionary optimization. The optimizations were performed using the optimal control loop described in section 5.3 and the GDD+GD parametrization described in section 5.4. During the optimizations, the ion yields of Cu_2^+ and Cu_3^+ were measured for each individual pulse shape and the fitness F of the pulses was determined either by the formula:

$$F = (\text{Cu}_2^+ - \text{Cu}_3^+) \cdot (\text{Cu}_2^+) \quad (6.1)$$

or by the routine:

$$\begin{aligned} \text{if } \text{Cu}_2^+ > T \quad F &= \text{Cu}_2^+ / \text{Cu}_3^+ \\ \text{else } F &= (\text{Cu}_2^+ / \text{Cu}_3^+) / 10, \end{aligned} \quad (6.2)$$

with the threshold T set to 700 or 800 counts. The fitness functions F were chosen such that not only a higher ($\text{Cu}_2^+ / \text{Cu}_3^+$) ratio is favored, but also a higher total signal level (especially with the first fitness function), such that the signal to noise ratio is sufficient for a successful optimization. It seems that optimal pulses obtained using formula 6.1 achieve higher ion yields, while optimal pulses obtained using the routine

6.2 achieve slightly higher optimization factors but lower ion yields. The optimizations were usually terminated after about 30 generations, determined by a very small mutation parameter indicating the infeasibility of significant further optimization. In the four best runs, optimization factors of 2.7 to 3.0 with respect to the short laser pulse were achieved. Even when compared to the -100 fs² chirped pulse, where the same ion yields are measured as with the optimal pulse, the optimization yields factors of 1.64 to 1.82. Figs. 6.7 through 6.10 show the comparison measurements of the optimal pulses and a short pulse together with the corresponding calculated TG-XFROG traces and intensity profiles of the optimal pulses obtained from the four best optimization runs. The TG-XFROG traces are calculated according to Eq. 2.55, as described in section 2.4.2. For this, the electric field of an optimal pulse is determined as described in section 5.6. During the comparison measurements, the Cu₃⁺ and Cu₂⁺ ion yields are monitored while switching between the optimized and the short white-light pulses. The optimization factors were calculated from the ion yields observed in the comparison measurements. The cationic mass spectra obtained with the fourth optimal pulse and a short 7 fs pulse are depicted in Fig. 6.11. The mass spectra show that the relative yields of Cu₂⁺ and Cu₃⁺ are significantly changed in favor of Cu₂⁺ by the optimal pulse. At the same time, the relative yield of Cu⁺ stays approximately the same for both pulses.

As observed from Figs. 6.7 through 6.10, the optimization algorithm does not lead to the compression of the supercontinuum to one few-cycle white-light laser pulse. The obtained nontrivial optimal pulse shapes suggest a complicated excitation mechanism involving a multitude of electronic states, in which the sub-pulses act in a cooperative manner, such that a higher fragmentation ratio is achieved. Analysis of the four optimized pulses reveals a very complex structure with several discrete short sub-pulses of variable intensities and wavelengths, with some sub-pulses spanning over the entire spectrum from the visible to NIR range. All four optimal pulses feature similar but also individual characteristics; common to all is a sequence of intense short sub-pulses with descending wavelength at the leading edge followed by less intense pulses with longer wavelengths at later times. However, the timings, the bandwidths and the number of sub-pulses vary. Considering only the sub-pulses with high intensity, the temporal delay between sub-pulses ranges from approximately 10 fs (Fig. 6.8 b) and 6.9 b)) to 115 fs (Fig. 6.9 b)) and the number of sub-pulses from three (Fig. 6.9 b)) to four or more (Fig. 6.8 b)). The trailing sequence of NIR pulses also features different numbers of sub-pulses and endures for 150 fs (Fig. 6.7 b)) to about 250 fs (Fig. 6.9 b)). In order to be able to elucidate the molecular reaction pathway effected by an optimal pulse, it is important to consider the intensity of each individual sub-pulse which might result in a certain non-linearity degree as well as the time delays within the pulse sequence with regard to the dynamic response of the Cu₃ cluster. For an optimal excitation, dissociation and ionization pathway, the occurrence of the sub-pulses in the optimized laser pulse has to be synchronized with the dynamics of the molecular system [48]. The broad bandwidth of the white-light pulses allows for the resonant excitation of many different electronic states lying at the available photon energies or their multiples. Furthermore, simultaneous excitation of several electronically excited states leading to the formation of electronic wave packets is possible[134]. Thus, both vibronic as well as electronic

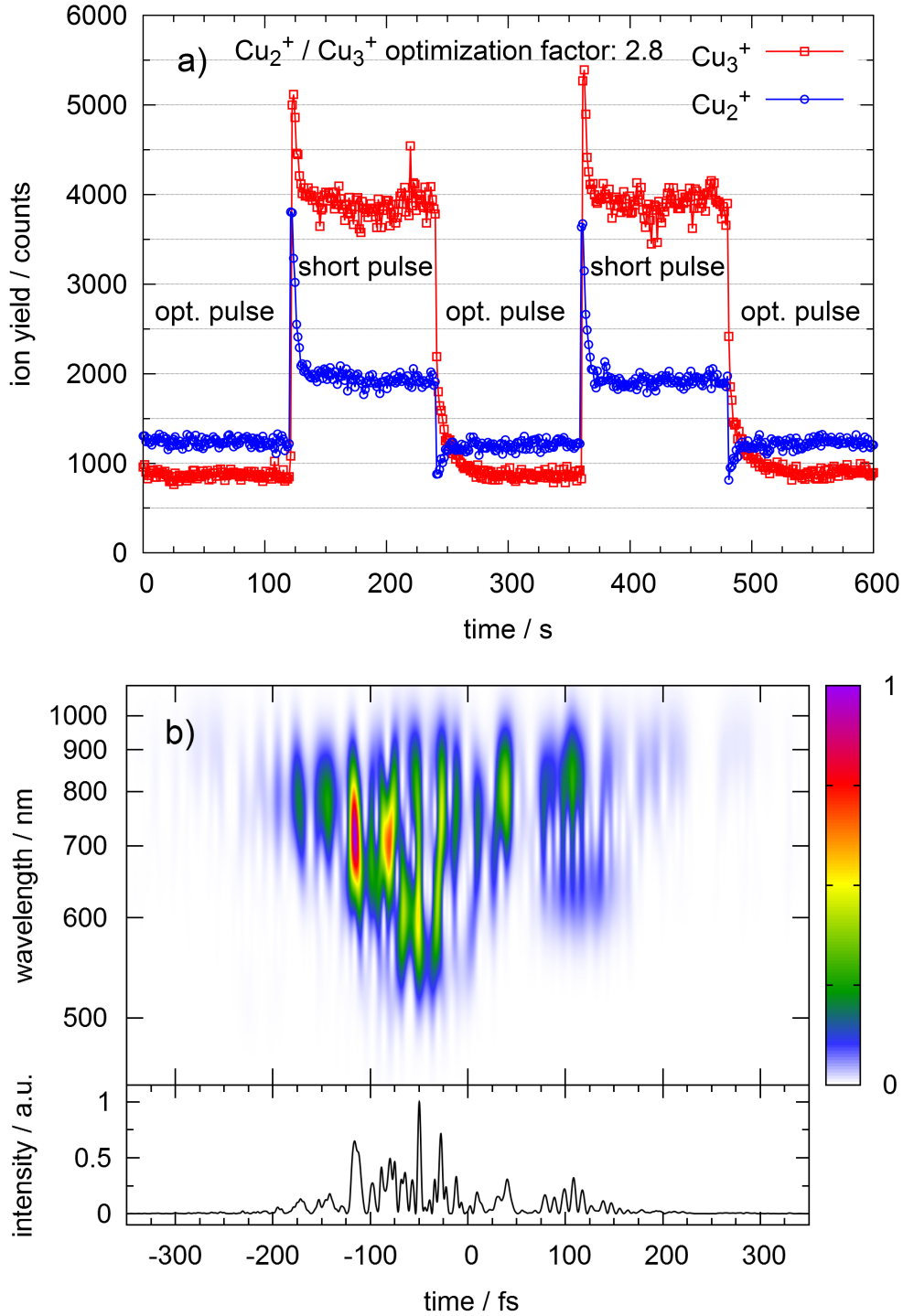


Figure 6.7: First optimization of the $(\text{Cu}_2^+ / \text{Cu}_3^+)$ ratio. a) Comparison of the ion yields generated with the optimized pulse and a short pulse, obtained by switching between the former and the latter. The ratio $(\text{Cu}_2^+ / \text{Cu}_3^+)$ has been improved by a factor of 2.8. b) Calculated TG-XFROG trace (top) and calculated intensity (bottom) of the optimized pulse. During this optimization run, the fitness was determined using the formula (6.1).

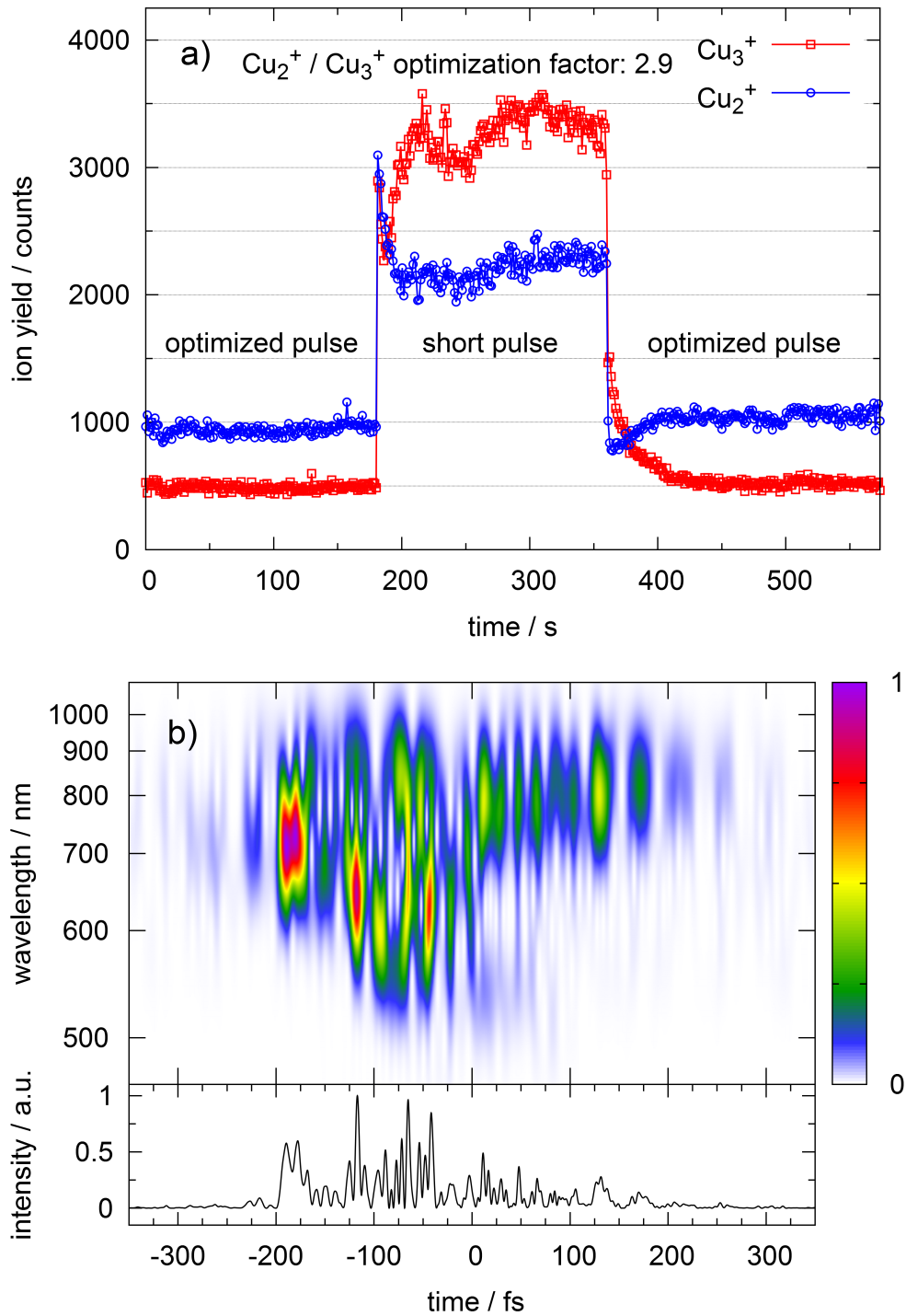


Figure 6.8: Second optimization of the ($\text{Cu}_2^+ / \text{Cu}_3^+$) ratio. a) Comparison of the ion yields generated with the optimized pulse and a short pulse, obtained by switching between the former and the latter. The ratio ($\text{Cu}_2^+ / \text{Cu}_3^+$) has been improved by a factor of 2.9. b) Calculated TG-XFROG trace (top) and calculated intensity (bottom) of the optimized pulse. During this optimization run, the fitness was determined using the routine (6.2).

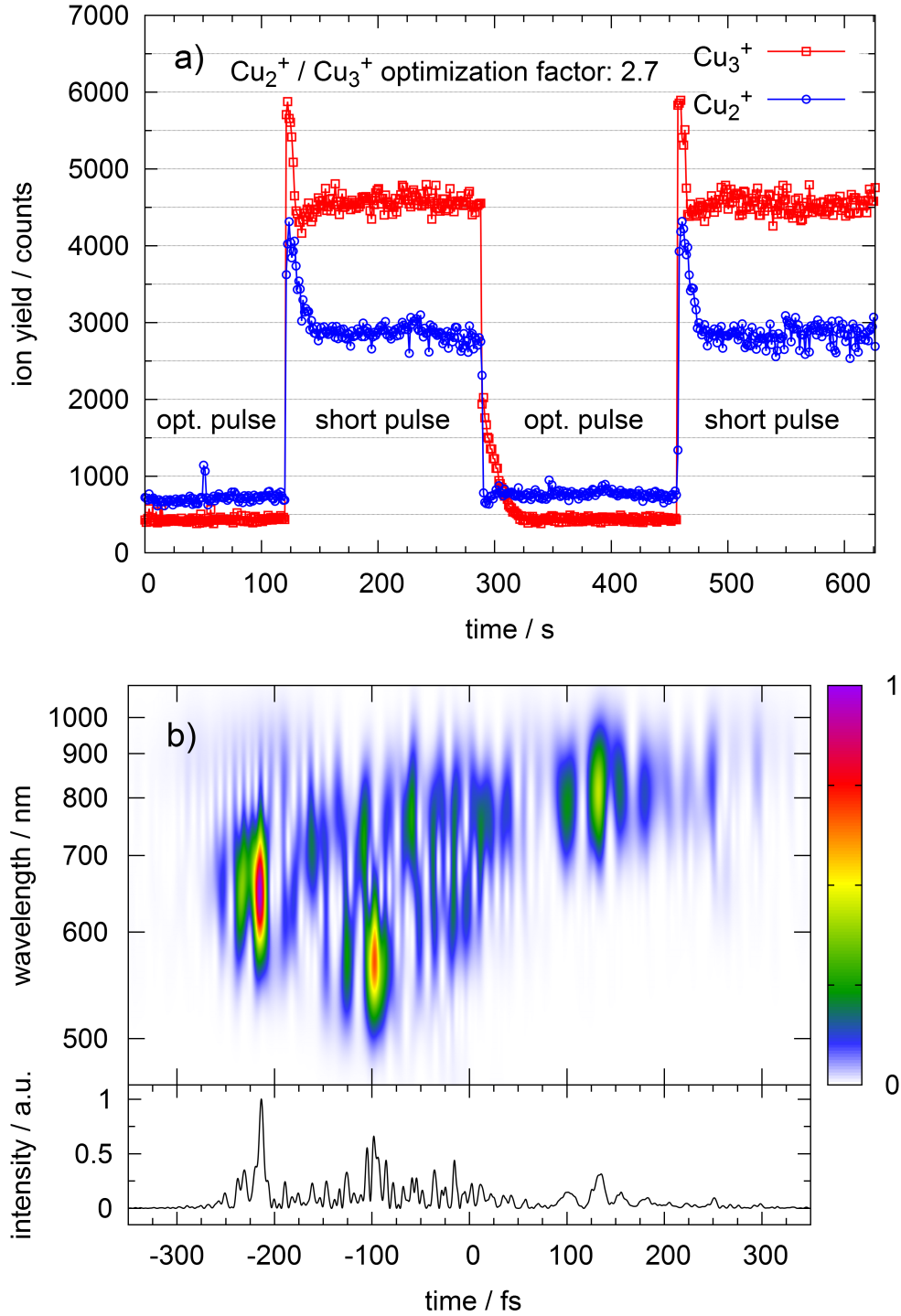


Figure 6.9: Third optimization of the $(\text{Cu}_2^+ / \text{Cu}_3^+)$ ratio. a) Comparison of the ion yields generated with the optimized pulse and a short pulse, obtained by switching between the former and the latter. The ratio $(\text{Cu}_2^+ / \text{Cu}_3^+)$ has been improved by a factor of 2.7. b) Calculated TG-XFROG trace (top) and calculated intensity (bottom) of the optimized pulse. During this optimization run, the fitness was determined using the routine (6.2).

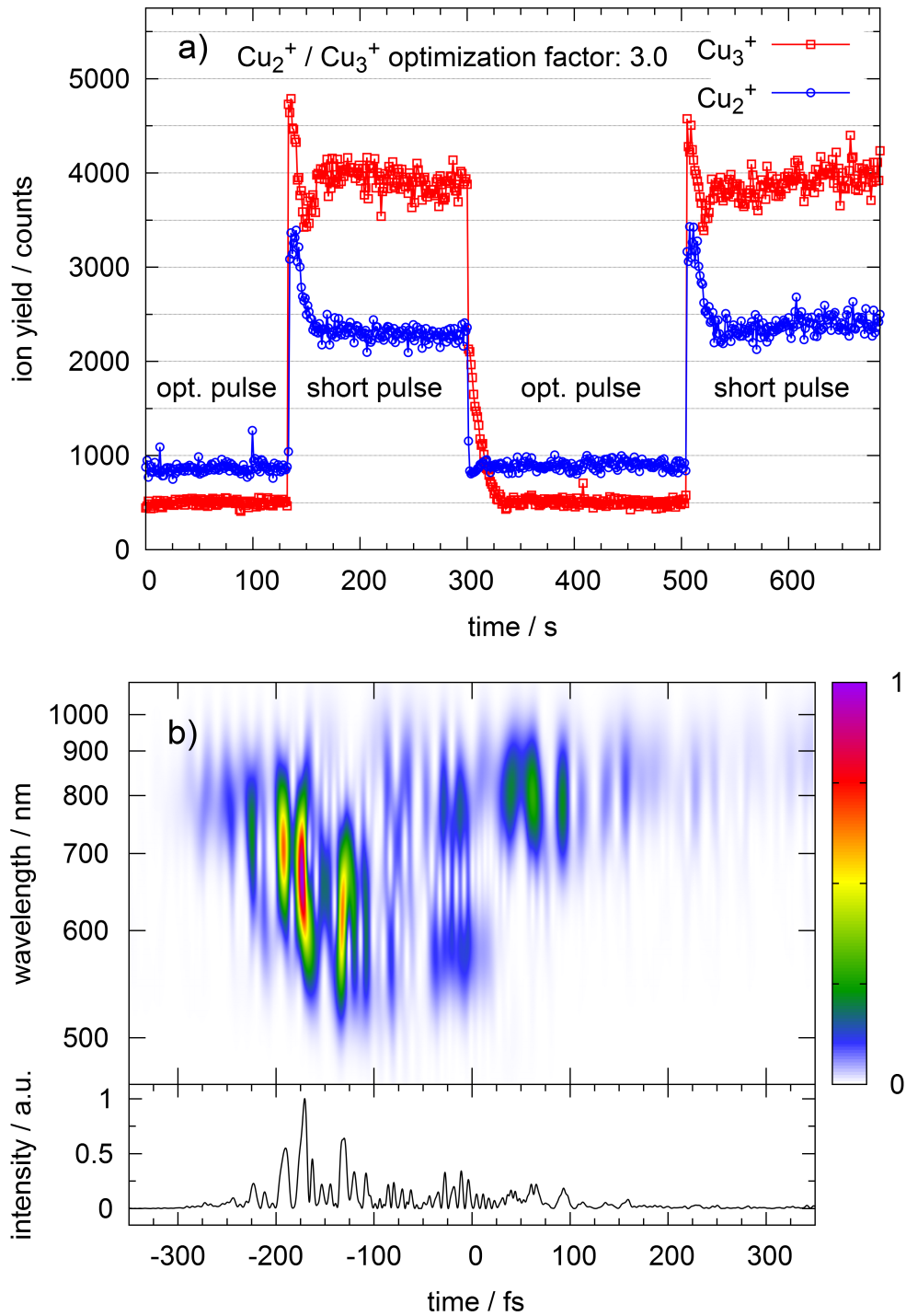


Figure 6.10: Fourth optimization of the ($\text{Cu}_2^+ / \text{Cu}_3^+$) ratio. a) Comparison of the ion yields generated with the optimized pulse and a short pulse, obtained by switching between the former and the latter. The ratio ($\text{Cu}_2^+ / \text{Cu}_3^+$) has been improved by a factor of 3.0. b) Calculated TG-XFROG trace (top) and calculated intensity (bottom) of the optimized pulse. During this optimization run, the fitness was determined using the routine (6.2).

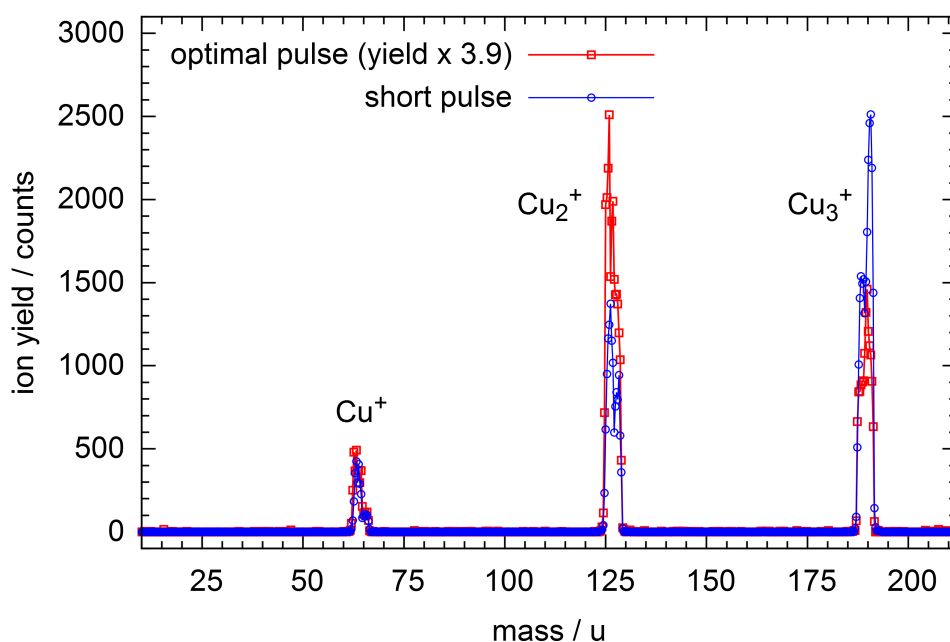


Figure 6.11: Cationic mass spectra obtained by irradiating Cu_3^- anions with the fourth optimized pulse and a short 7 fs pulse, respectively. The ion yield obtained with the optimal pulse is magnified 3.9 times for better comparability.

wave packets might play a role for the effective excitation and ionization of the desired fragment. The time-delays between the sub-pulses which range from ten up to a few hundred femtoseconds are too short to be addressing only vibrational dynamics [135], which for the triangular neutral Cu_3 feature periods between 115 and 284 fs [131, 136]. Thus, the short sub-pulse delays likely are the signature of electronic wave packets [38]. Such intramolecular electronic wave packets, formed by the simultaneous excitation of energetically close lying excited states, have been observed previously [36, 37] and more recently by means of attosecond pulses [38]. However, a more in-depth interpretation of the obtained optimal pulse shapes requires a rigorous computational treatment. In a qualitative manner, it can be stated that the complex pulse shapes in Figs. 6.7 b) through 6.10 b) suggest a stepwise excitation mechanism along various electronic states or their superpositions, with femtosecond time delays between the sub-pulses such that beneficial Franck-Condon windows and wave-packet interferences for the excitation are met, leading to the highly selective formation of Cu_2^+ fragment ions and minimization of the energetically more favorable direct photoionization of the Cu_3 trimer.

The fact that neither Cu_3^+ cations nor anions fragment when irradiated with the short or optimized laser pulses, with wavelengths below 540 nm blocked (see section 6.7), suggests that the fragmentation into Cu_2^+ during the charge reversal process has to occur in an excited state of the neutral Cu_3 cluster.

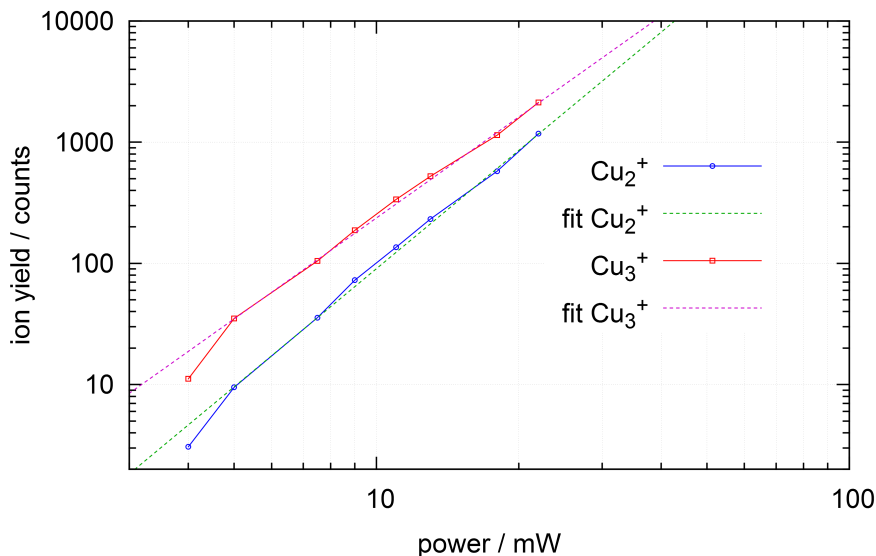


Figure 6.12: Cu_3^- charge reversal power dependence measurement. The trapped Cu_3^- anions are irradiated with 7 fs white-light pulses with variable pulse energy. Cu_3^+ and Cu_2^+ product cation yields are displayed on a bilogarithmic scale. The exponential fits yield a power dependence of $I^{2.9}$ for Cu_3^+ and $I^{3.3}$ for Cu_2^+ .

6.6 Power Dependence of the Cu_3^- Charge Reversal

To make sure that the optimization of the $(\text{Cu}_2^+ / \text{Cu}_3^+)$ ratio is not just a trivial intensity effect, and for investigating whether resonant intermediate states are involved, the power dependence of the Cu_3^- charge reversal was measured. The trapped Cu_3^- anions were irradiated with 7 fs white-light pulses and the power was adjusted by means of a polarizer (wire grid, Edmund Optics). The wavelengths below 540 nm were blocked. Fig. 6.12 shows the power dependence measurement. The yields of the Cu_3^+ and Cu_2^+ product cations are monitored with the second quadrupole mass filter. The power measurements yield a $I^{2.9}$ dependence for the formation of Cu_3^+ and a $I^{3.3}$ dependence for Cu_2^+ . The VDE for Cu_3^- is 2.37 eV and the ionization potentials for Cu_3 and Cu_2 are 5.8 eV [133] and 7.9 eV [137]. Hence, a minimum of four 600 nm photons or six 800 nm photons are necessary for the generation of Cu_3^+ cations and a minimum of five 600 nm photons or seven 800 nm photons are necessary for the formation of Cu_2^+ cations. Considering also the dissociation energy for the loss of Cu from neutral Cu_3 of approximately 1 eV [131], one more photon might be required for the formation of Cu_2^+ . The fact that the power dependence observed in the experiment is lower indicates that at least one resonant intermediate state, most probably an excited state of the neutral species, is involved in the charge reversal process.

6.7 Laser-Induced Decomposition of Cu_3^-

In order to elucidate the fragmentation mechanism during charge reversal experiments, LID experiments on the Cu_3^- anion were conducted. The trapped anions are irradiated

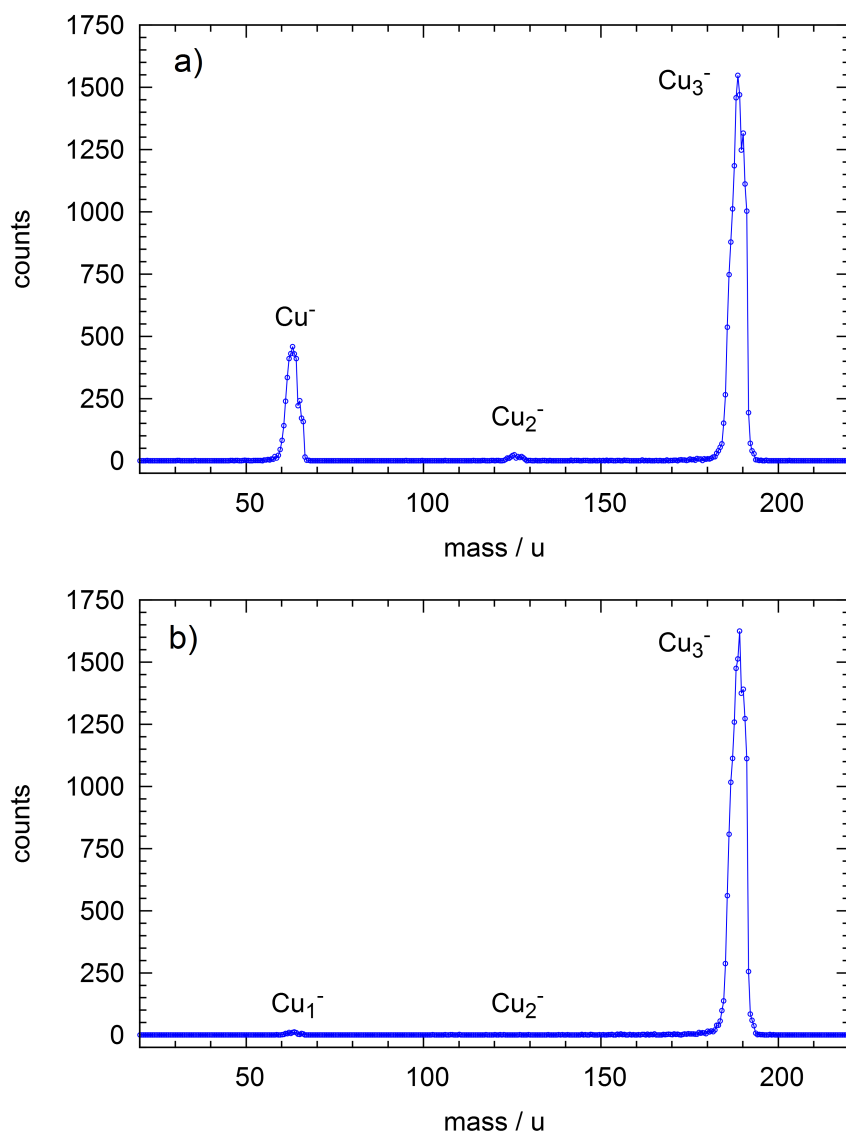


Figure 6.13: LID measurements of Cu_3^- anions. a) Mass spectrum of the product anions when irradiating Cu_3^- anions with 7 fs, 20 μJ white-light pulses featuring the full white-light spectrum as depicted in Fig. 6.4 a). b) Mass spectrum of the product anions of Cu_3^- anions irradiated with 7 fs, 20 μJ white-light pulses with the wavelengths shorter than 540 nm blocked.

with 7 fs, 20 μJ white-light pulses featuring the full white-light spectrum as depicted in Fig. 6.4 a) and a spectrum where the shortest wavelengths are blocked up to a variable cutoff wavelength. The parent ion and the LID products were analyzed with the second quadrupole mass spectrometer. Fig. 6.13 a) shows a mass spectrum of the product anions of Cu_3^- anions irradiated with 7 fs, 20 μJ white-light pulses featuring the full white-light spectrum as depicted in Fig. 6.4 a). A considerable amount (around one quarter) of the Cu_3^- anions fragments into Cu^- and a small amount of Cu_2^- is detected as well. Fig. 6.13 b) shows a mass spectrum of the product anions of Cu_3^- anions irradiated with 7 fs, 20 μJ white-light pulses with the wavelengths shorter than 540 nm blocked. The fragments observed when irradiating Cu_3^- anions with the full white-light

spectrum disappear almost completely when these wavelengths are blocked out. Only a tiny amount of Cu^- is detected.

For a better understanding of the influence of the shorter wavelengths on the LID of Cu_3^- anions, the wavelength dependency was investigated in detail. A measurement was performed, during which the wavelengths below 550 nm were gradually unblocked while the yield of the Cu_3^- anions and the yield of the fragments Cu_2^- and Cu^- were monitored with the second quadrupole mass filter Q_2 . The measurement is depicted in Fig. 6.14. No Cu^- anions are detected as long as the wavelengths below 540 nm are blocked. At a cutoff wavelength of 535 nm Cu^- ions start to appear. The Cu^- fragment ion signal shows an edge at 528 nm (2.35 eV), a value which is very close to the VDE of Cu_3^- (2.37 eV) [132], and remains steady for cutoff wavelengths below 520 nm. No Cu_2^- anions could be detected even when irradiating Cu_3^- anions with full bandwidth laser pulses. The Cu_3^- parent ion signal shows a constant depletion of about 500 counts independent of the cutoff wavelength, suggesting that the Cu^- fragment anions arise from the photo-depleted, neutralized portion. Although collision induced dissociation (CID) measurements on Cu_3^- of Spasov et al. [138], reveal the loss of Cu_2 , and thus the formation of Cu^- , as the favored fragmentation channel, this cannot be the case here, due to the wavelength-independent photodepletion of the parent ion. Cu^- fragment anions could thus result from the photodissociation on an excited state of the neutral Cu_3 cluster, for example a Cu^-Cu_2^+ ion pair state, or alternatively from the fragmentation of neutral Cu_3 into Cu_2 and Cu followed by an electron capture of the latter, facilitated by the enhanced generation of photoelectrons caused by the single-photon photodetachment of Cu_3^- .

6.8 Laser-Induced Decomposition of Cu_3^+

To gain more insight into the fragmentation during charge reversal, LID experiments on the Cu_3^+ cation were conducted by irradiating the trapped Cu_3^+ cations with 7 fs short white-light pulses or one of the four optimized pulses depicted in Fig. 6.15. The obtained mass spectra are shown in Fig. 6.15. Only a minuscule amount of Cu_2^+ is detected when Cu_3^+ is irradiated with 7 fs, 20 μJ white-light pulses with the wavelengths below 540 nm blocked. When Cu_3^+ is irradiated with one of the four best pulses optimized for the ratio ($\text{Cu}_2^+ / \text{Cu}_3^+$), hardly any Cu_2^+ is detected. Next to no Cu^+ is detected when irradiating Cu_3^+ with the short pulses and when irradiated with one of the optimized pulses, no Cu^+ is detected. As already shown by Jarrold et al. [139], fragmentation of internally cold Cu_3^+ cations requires wavelengths shorter than 440 nm which are not available in the experiments presented here.

6.9 Conclusion

The white-light optimal control of a photo-fragmentation in the context of a charge reversal process has been demonstrated for the first time by using an evolutionary algorithm and a pulse shaping setup. The use of shaped supercontinuum white-light pulses allows

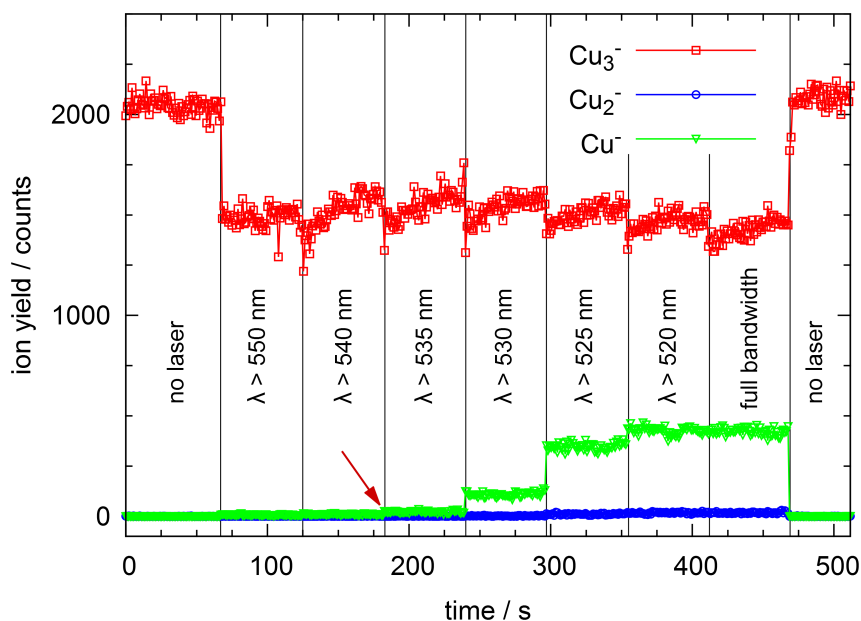


Figure 6.14: Measurement of the laser induced decomposition of Cu_3^- anions with 7 fs short white-light pulses versus the cutoff wavelength of the laser pulse spectrum. Both Cu_3^- parent ion as depletion spectrum as well as the Cu_2^- and Cu^- fragment ion channels were monitored. The red arrow marks the onset of the Cu^- ion signal at $\lambda > 535$ nm.

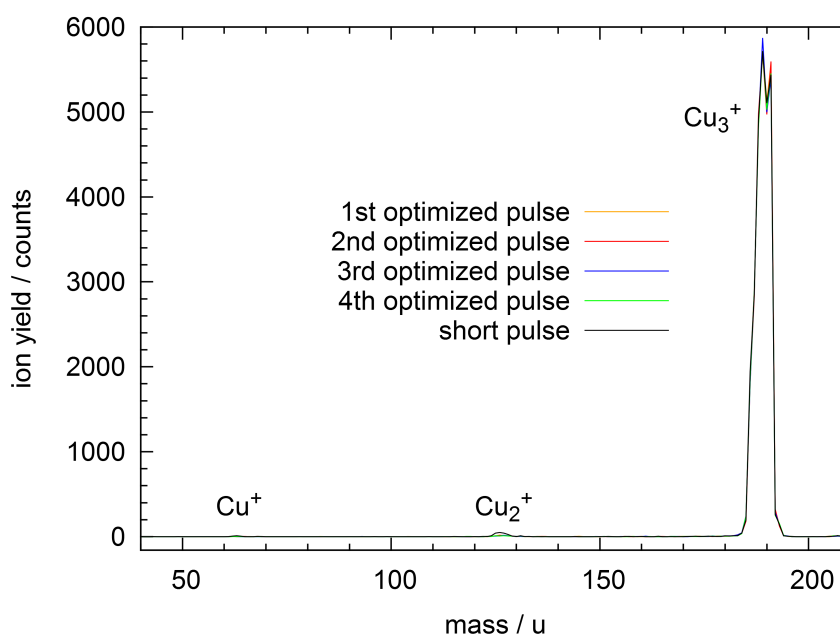


Figure 6.15: Measurement of the laser induced decomposition of Cu_3^+ cations with 7 fs short white-light pulses ($\lambda > 540$ nm) and the four best pulses optimized for the ratio ($\text{Cu}_2^+ / \text{Cu}_3^+$). For the short pulse, a very small amount of Cu_2^+ is detected. For the optimized pulses, no fragmentation of the Cu_3^+ cations is observed.

to address not only a series of vibrationally but also a multitude of electronically excited states for the investigated molecules, opening access to a high diversity of pathways to reach the target state. For an efficient optimization, the GDD+GD parametrization routine was developed, which generates only suitable laser pulses with peak intensities sufficient to produce acceptable charge reversal cationic signals. Optimization factors for the fragment to parent ion yield ratios of up to 3.0 relative to the short 7 fs white-light pulses are achieved. Such optimization factors demonstrate the high selectivity in populating specific points on the potential energy surface, attainable with the presented method. Investigation of the optimal pulse profiles suggests that not only vibronic, but also electronic wave packets are created and probed. The power dependence measurements performed with short white-light pulses indicate that at least one excitation step must be resonant for the formation of both parent and fragment cations.

Experiments on the Aluminum Tetramer

7.1 Introduction

To test the broad applicability of the experimental technique, the optimal control of the photofragmentation of Al_4 clusters during charge reversal is studied. Moreover, the results obtained for the copper trimer, especially the high probability of initiation and probing of electronic wavepackets by the optimally shaped few-cycle white-light pulses, should be tested and hopefully reproduce. DFT-calculated structures of the anionic and the neutral Al_4 cluster are depicted in Figs. 7.1 a) and b). Both, anion and neutral have nearly identical rhombus geometries (D_{2h} symmetry) [140]. Hence, the neutral Al_4 cluster could be present in the ground state after electron photodetachment of the Al_4^- cluster anion, as the tetrahedral ground state geometries are equal and the photoelectron may take away the excess energy. Fig. 7.1 c) shows the DFT-calculated possible structures of the Al_4^+ cluster cation, which might be tetrahedral, funnel-like, or rhombic similar to the neutral and anionic species [141].

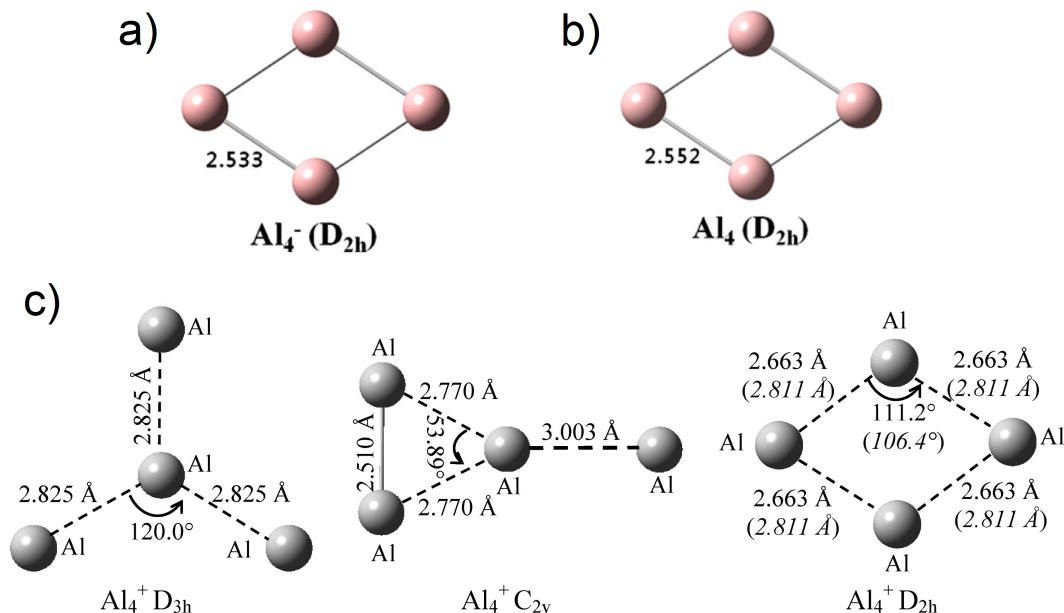


Figure 7.1: DFT-calculated structure for a) the Al_4^- anion and b) the neutral Al_4 cluster. Images taken from [140]. c) Calculated possible structures for the Al_4^+ cation. Image adapted from [141].

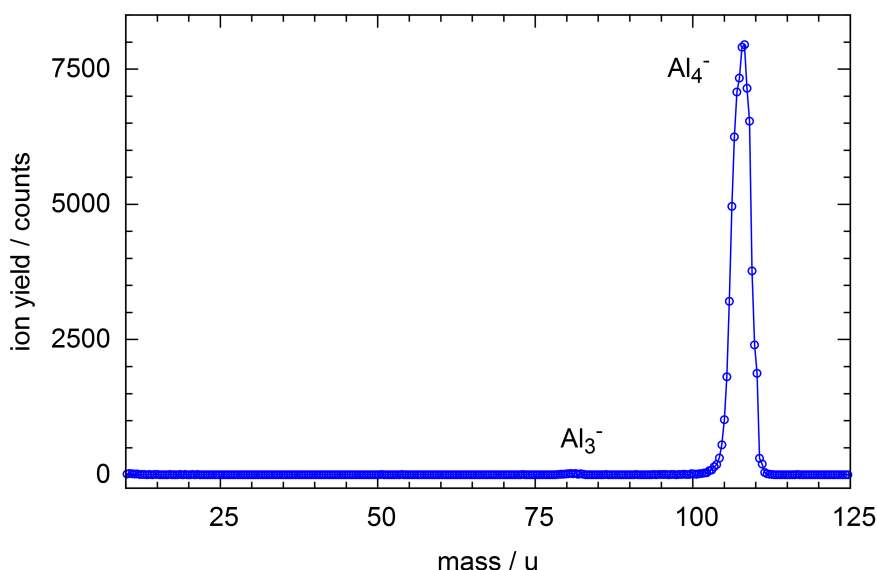


Figure 7.2: Mass spectrum of Al_4^- cluster anions trapped in the ion trap at 20 K. No fragmentation occurs during trapping or extraction from the trap.

7.2 Al_4^- Cluster Preparation

The Al_4^- cluster anions are prepared in a similar way as the Cu_3^- cluster anions (see section 6.2), namely by sputtering an aluminum target in the magnetron sputtering source described in section 4.4. The argon gas used for sputtering is injected via a mass flow controller at a flow rate of approximately 5.5 sccm. The sputtering power is around 17 W. The generated ions enter the main chamber via the skimmer which is held at an attractive potential of +200 to +300 V.

The Al_4^- cluster anions are mass-selected in the first quadrupole mass filter and trapped in the ion trap. The trap is filled with helium buffer gas (6.0, Linde AG) at a pressure of 0.03 mbar and is cooled to 20 K. Fig. 7.2 shows a mass spectrum of Al_4^- cluster anions which were trapped in, and extracted from the ion trap. The mass scan shows that nearly no fragmentation of the Al_4^- cluster anions into anionic products occurs during trapping or extraction from the trap, as only a miniscule amount of Al_3^- is detected.

7.3 White-Light Pulse Generation

Initial LID investigations on the Al_4^- anions indicated that no photofragmentation into anionic products occurs, even when the anions were irradiated with 7 fs pulses featuring the entire white-light spectrum. Fig. 7.3 shows a mass spectrum of Al_4^- cluster anions trapped in the ion trap at 20 K, irradiated with 20 μJ , 7 fs white-light laser pulses. Even though approximately 60 % of the Al_4^- anions are photo-depleted, almost no anionic fragments are detected. Hence, all experiments on Al_4^- were performed using the entire spectrum of the white-light laser pulses as depicted in Fig. 6.4 a). As for the experiments on the copper trimer, the short pulses were always compressed to 7 fs or less.

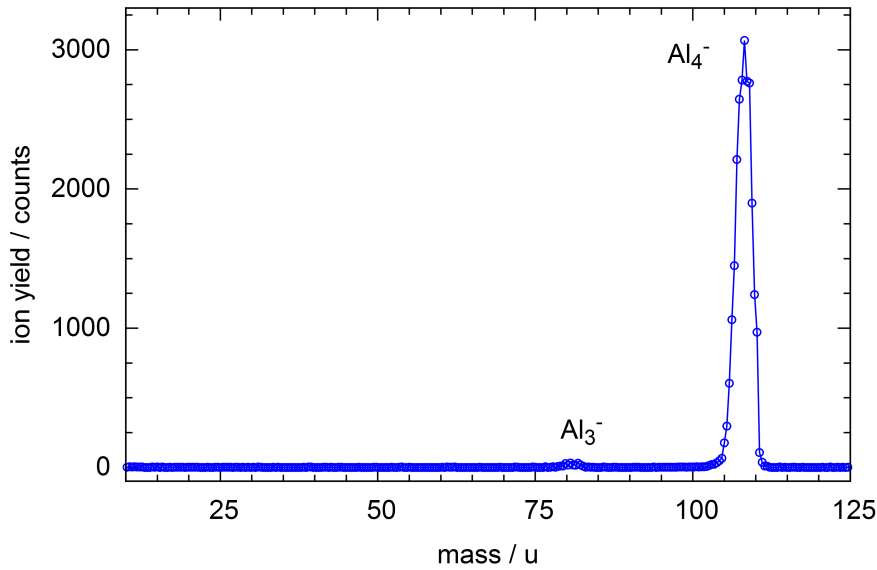


Figure 7.3: Mass spectrum of Al_4^- cluster anions trapped in the ion trap at 20 K, irradiated with 20 μJ , 7 fs white-light laser pulses. No fragmentation occurs during trapping or extraction from the trap while approximately 60 % of the anion yield is depleted.

7.4 Al_4^- charge reversal experiments

To investigate the abundance of cationic products, Al_4^- charge reversal experiments with short white-light pulses were performed. A typical cationic mass spectrum obtained by irradiating the trapped and thermalized Al_4^- anions with 7 fs white-light pulses is shown in figure 7.4. The highest cationic yield is observed for Al_4^+ , generated by multiphotonic excitation and ionization of the parent anions, followed by strong Al^+ , Al_3^+ , and Al_2^+ photofragment signals. Even a small amount of Argon tagged Al^+ ions (67 amu) is detected. Although such weakly bound complexes formed via three body collisions have already been observed in low temperature ion traps [142], the formation of the $\text{Al}^+\cdot\text{Ar}$ complex in this experiment is surprising and indicates that the Al^+ photofragments have sufficient time in the trap to thermalize and bind an Ar atom prior to their extraction from the trap. The Ar atoms required for tagging enter the trap through diffusion from the sputtering source region, where large amounts are used for the sputtering process.

In order to investigate the influence of the spectral phase of the pulses on the photofragmentation process upon charge reversal, a linear chirp scan between $\phi'' = -300 \text{ fs}^2$ and $\phi'' = +300 \text{ fs}^2$ was first performed while monitoring the parent and the photofragment cation yields, as shown in figure 7.5. As can be observed from Fig. 7.5, for $\phi'' = 0$ the Al_4^+ ion signal is higher than for the Al^+ photo-fragment, while this ratio strongly changes for stronger positive and negative chirps where the Al^+ yield is highest. The ion yields for the other two fragments are very low and are not considered further.

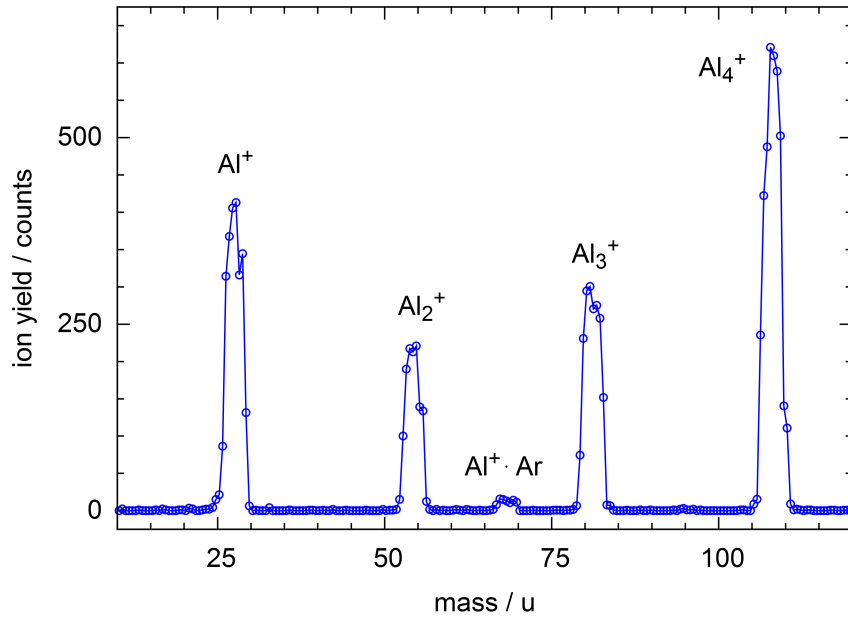


Figure 7.4: Mass spectrum of the Al_n^+ ($n = 1-4$) product cations generated in a charge reversal experiment, starting from Al_4^- anions that were irradiated with $20 \mu\text{J}$, 7 fs white-light laser pulses.

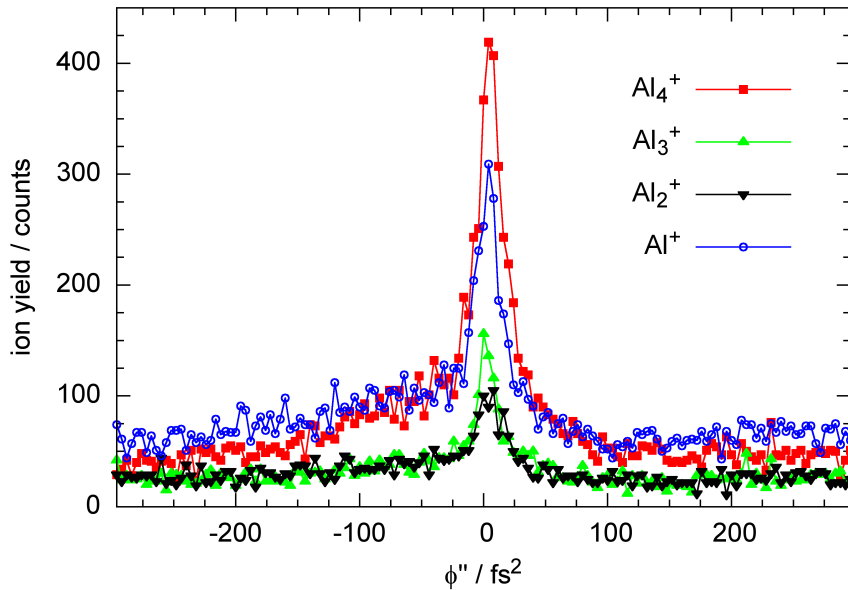


Figure 7.5: Al_4^- charge-reversal linear chirp scan from -300 to +300 fs^2 . The Al_4^+ , Al_3^+ , Al_2^+ and Al^+ cation yields are monitored.

7.5 Optimal control of the Al_4^- charge reversal process

Based on the results of the chirp scan (see Fig. 7.5), maximizing the $(\text{Al}^+/\text{Al}_4^+)$ ratio was chosen as an objective for optimization. As for the copper trimer, the optimizations were performed using the optimal control loop described in section 5.3 and the GDD+GD

parametrization described in section 5.4. For optimizing the $(\text{Al}^+/\text{Al}_4^+)$ ratio, the Al^+ and Al_4^+ ion yields were measured for each individual pulse shape. The yields obtained for the Al cluster cations are relatively low. Hence, in order to maintain a sufficient signal to noise ratio, the fitness F of the pulses was determined only by using formula

$$F = (\text{Al}^+ - \text{Al}_4^+) \cdot (\text{Al}^+), \quad (7.1)$$

which favors the signal level increase more than a threshold-based routine like Eq. (6.2), that was used for most copper trimer optimizations.

In the four best optimization runs, optimization factors of 2.7 up to 3.4 relative to a short 7 fs pulse were obtained for the $(\text{Al}^+/\text{Al}_4^+)$ ratio. Figs. 7.6 through 7.9 show the calculated TG-XFROG traces and intensity profiles of the optimal pulses obtained in the four best optimization runs and the comparison of the Al^+ and Al_4^+ cation yields for the optimal and the short laser pulses. The TG-XFROG traces are calculated according to Eq. (2.55), as described in section 2.4.2. For this, the electric field of an optimal pulse is determined as described in section 5.6. An improvement of the $(\text{Al}^+/\text{Al}_4^+)$ ratio is observed also during the linear chirp scan (see Fig. 7.5). The optimization factors calculated relative to a pulse with a chirp of -175 fs^2 are between 1.25 and 1.75. The cationic mass spectra obtained with the fourth optimal pulse and a short 7 fs pulse are depicted in Fig. 7.10. The mass spectra nicely show how the distribution is shifted towards smaller clusters with the optimal pulse. Most significant is the relative decrease in the Al_4^+ yield. The relative yields of Al^+ and Al_2^+ both increase while Al_3^+ stays at approximately the same relative yield. By analyzing the optimal pulse traces, a considerable difference is observed between the first and the other three traces (see Fig. 7.6 b) versus Figs. 7.7 to 7.9 b)). While the first optimized pulse features a sequence of many short pulses with descending wavelengths, the other three present sequences of short pulses with ascending wavelengths. This difference is attributed to two very different pathways which result, however, in similar optimization factors. All four optimal pulses feature very short sub-pulse delays on the order of 10 fs. As in the case of Cu_3 , such short sub-pulse delays cannot account solely for vibronic dynamics, which for neutral rhombus Al_4 feature periods between 99 and 498 fs [140], and thus likely are a signature of electronic wave packet propagation. The vertical electron affinity of Al_4^- extracted from photoelectron spectra is approximately 2.0 eV [128, 129, 143, 144]. Hence, single-photon photodetachment is possible with the employed laser spectrum. As both the anion and the neutral clusters have similar rhombus geometries (D_{2h} symmetry) [140], resulting in close values for the vertical and adiabatic electron affinities, the Al_4 clusters could be present in their neutral electronic ground state after electron photodetachment [127, 140, 141, 145]. Thus, fragmentation during the charge reversal probably occurs in an excited state of the neutral cluster.

The measured power dependences (see section 7.6) of $I^{2.9}$ for the generation of Al_4^+ and $I^{3.3}$ for the generation of Al^+ prove that the optimization of the $(\text{Al}^+/\text{Al}_4^+)$ ratio is not a trivial intensity effect, as the observed power dependence of the Al^+ yield is higher than the power dependence of the Al_4^+ yield.

Considering the above mentioned vertical electron affinity for Al_4^- of 2.0 eV in addition to the ionization potentials of 6.0 eV for Al and more than 6.5 eV for Al_4 [130], at least

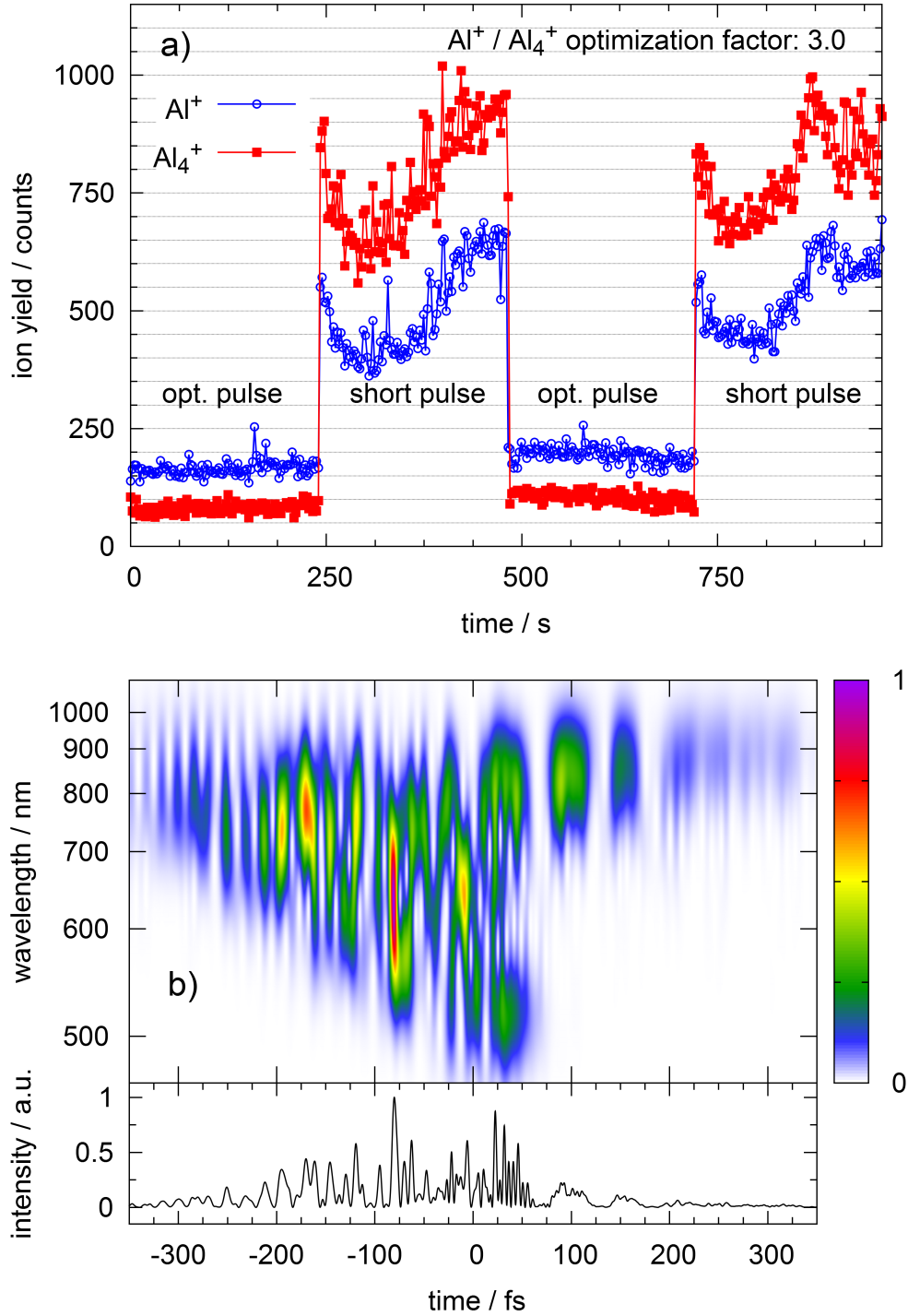


Figure 7.6: First optimization of the ($\text{Al}^+/\text{Al}_4^+$) ratio. a) Comparison of the ion yields generated with the optimized pulse and a short pulse, obtained by switching between the former and the latter. The ratio ($\text{Al}^+/\text{Al}_4^+$) has been improved by a factor of 3.0. b) Calculated TG-XFROG trace (top) and calculated intensity (bottom) of the optimized pulse.

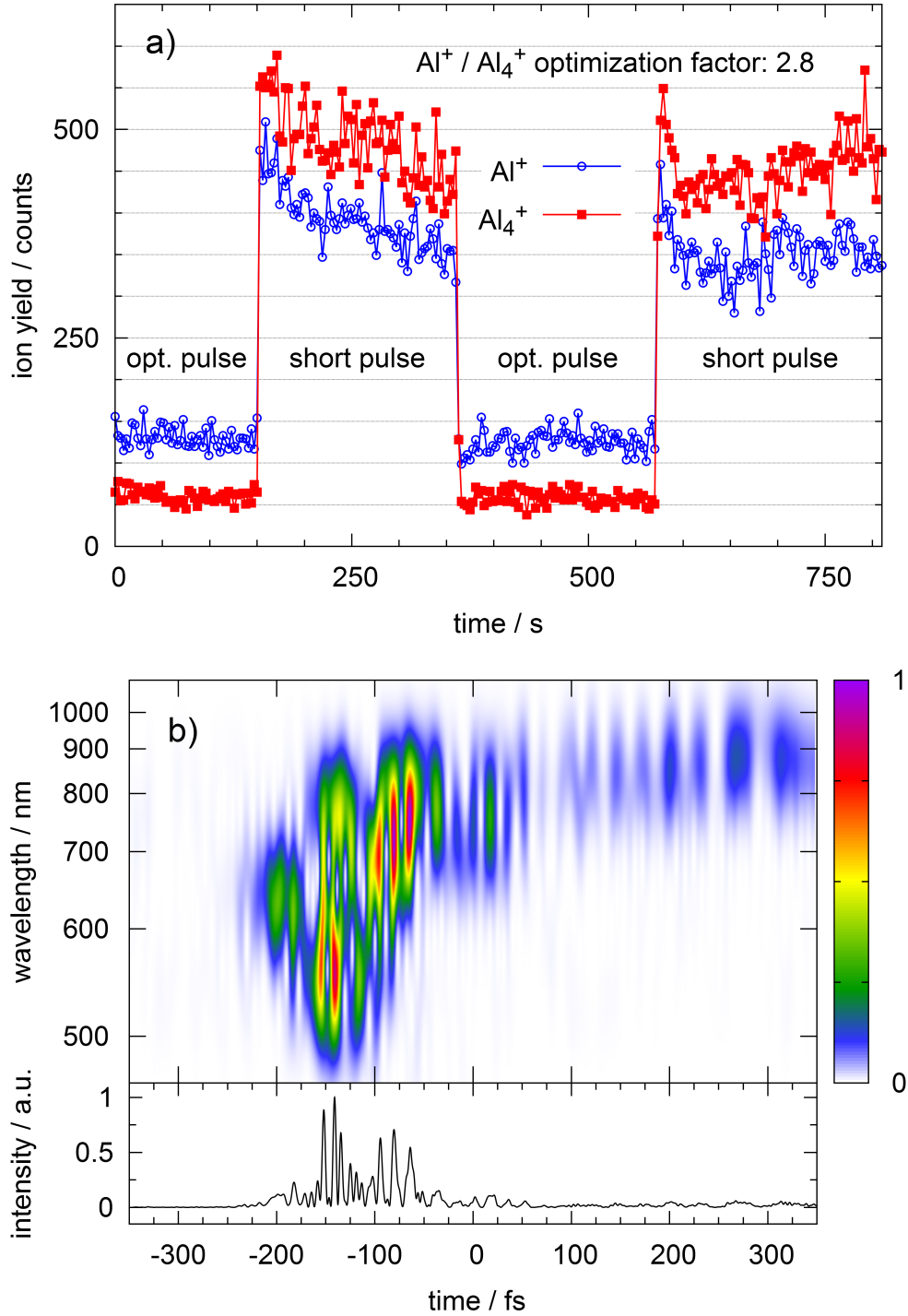


Figure 7.7: Second optimization of the $(\text{Al}^+/\text{Al}_4^+)$ ratio. a) Comparison of the ion yields generated with the optimized pulse and a short pulse, obtained by switching between the former and the latter. The ratio $(\text{Al}^+/\text{Al}_4^+)$ has been improved by a factor of 2.8. b) Calculated TG-XFROG trace (top) and calculated intensity (bottom) of the optimized pulse.

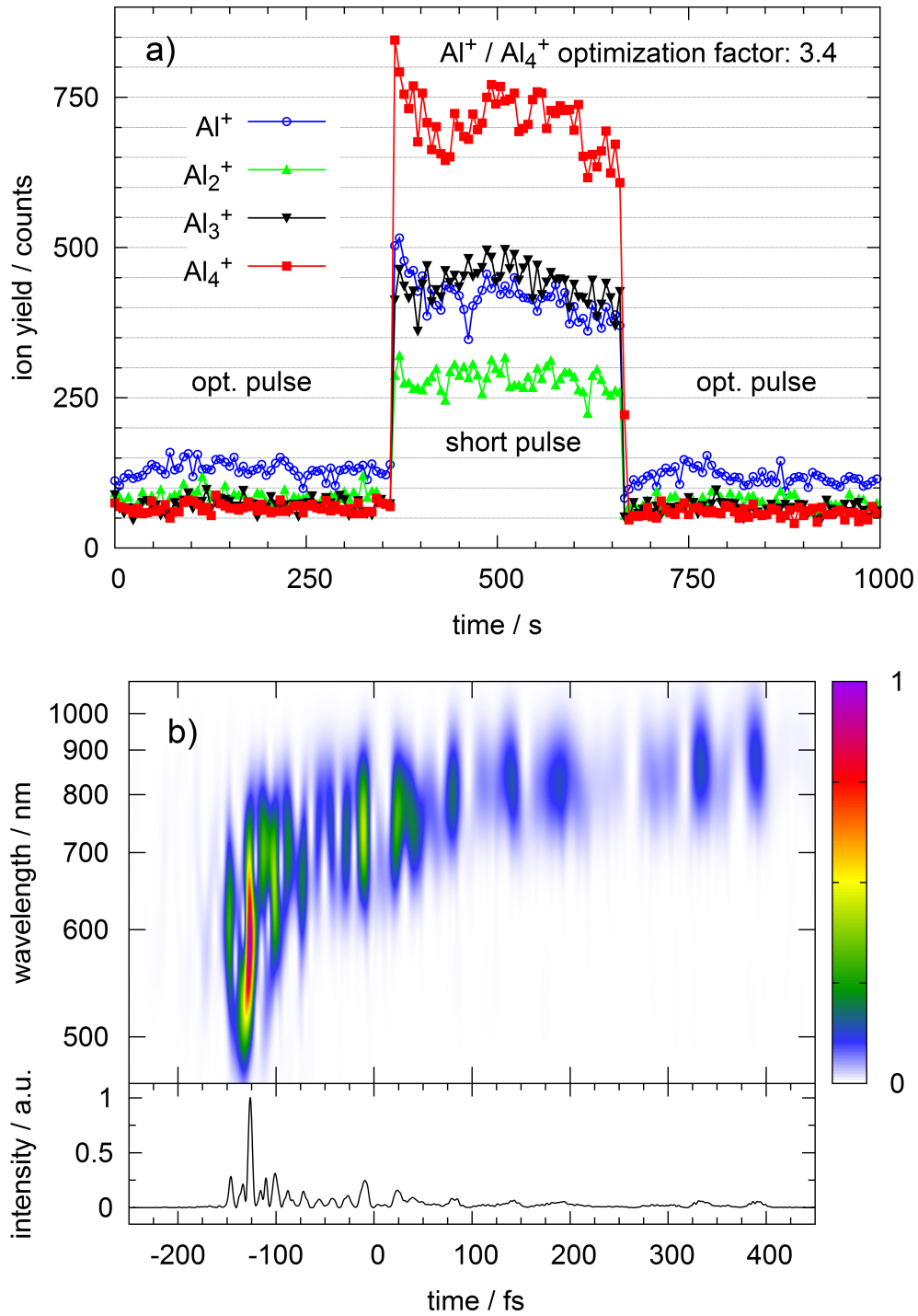


Figure 7.8: Third optimization of the ($\text{Al}^+/\text{Al}_4^+$) ratio. a) Comparison of the ion yields generated with the optimized pulse and a short pulse, obtained by switching between the former and the latter. The ratio ($\text{Al}^+/\text{Al}_4^+$) has been improved by a factor of 3.4. Al_2^+ and Al_3^+ are monitored as well. b) Calculated TG-XFROG trace (top) and calculated intensity (bottom) of the optimized pulse.

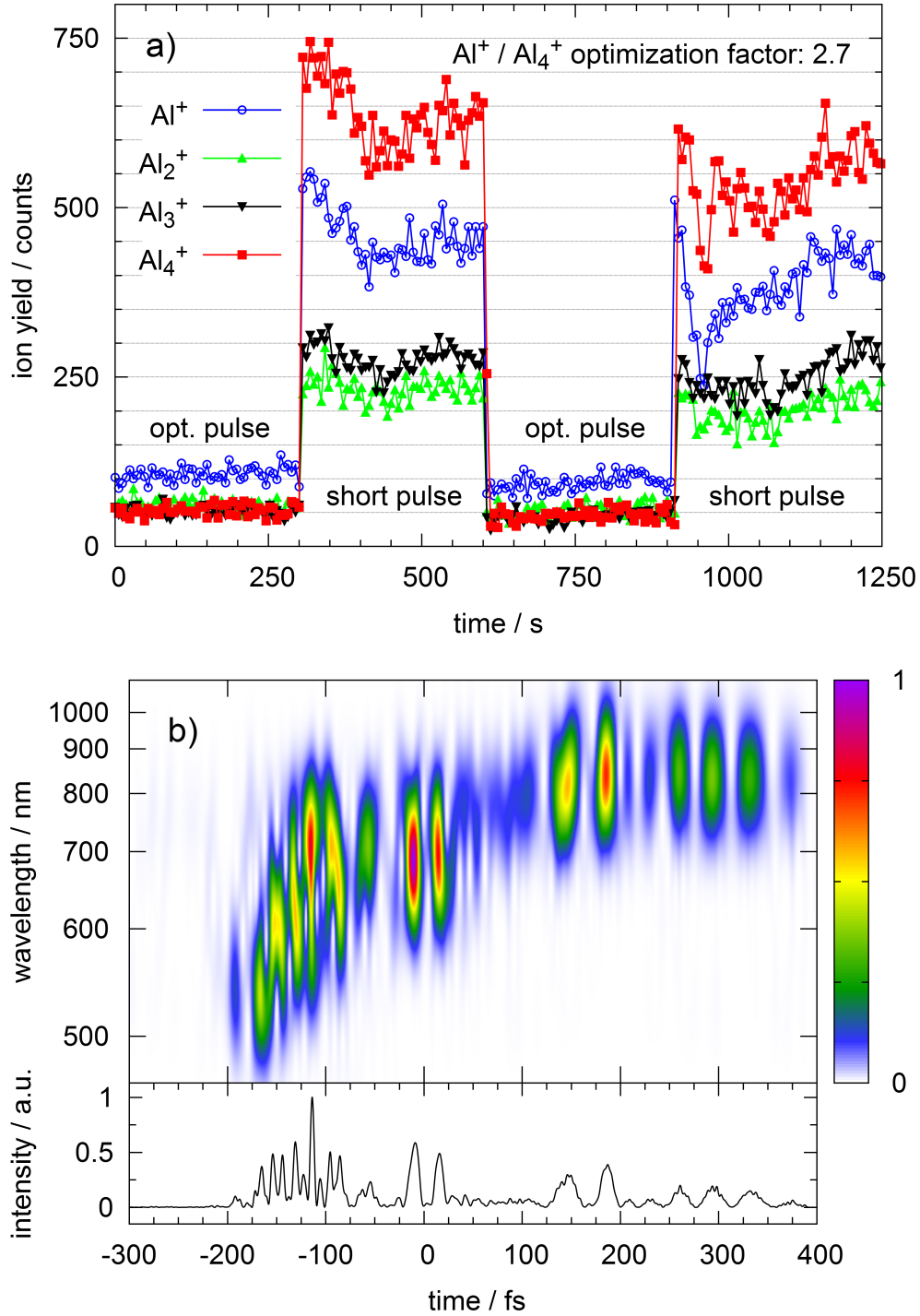


Figure 7.9: Fourth optimization of the $(\text{Al}^+/\text{Al}_4^+)$ ratio. a) Comparison of the ion yields generated with the optimized pulse and a short pulse, obtained by switching between the former and the latter. The ratio $(\text{Al}^+/\text{Al}_4^+)$ has been improved by a factor of 2.7. Al_2^+ and Al_3^+ are monitored as well. b) Calculated TG-XFROG trace (top) and calculated intensity (bottom) of the optimized pulse.

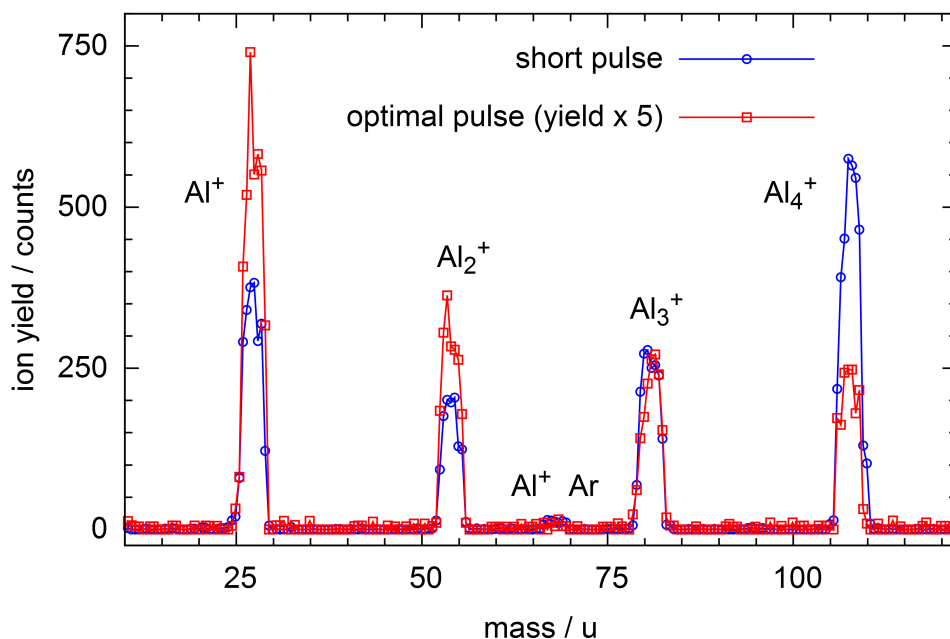


Figure 7.10: Cationic mass spectra obtained by irradiating Al_4^- anions with the fourth optimized pulse and a short 7 fs pulse. The ion yield obtained with the optimal pulse is magnified five times for better comparability.

8.0 eV and 8.5 eV are required for the generation of Al^+ and Al_4^+ , respectively. Hence, at least four 600 nm photons or six 800 nm photons are needed for the charge reversal process and fragmentation into Al^+ . Taking the dissociation energy of neutral Al_4 into Al of approximately 2.0 eV into account [140], an even higher number of photons might be required for the formation of Al^+ . As for Cu_3^- , the smaller observed power dependence indicates that at least one resonant intermediate electronic state is involved.

7.6 Power Dependence of the Al_4^- Charge Reversal

The power dependence measurements were conducted by trapping the Al_4^- anions in the ion trap and irradiating them with 7 fs white-light pulses of variable energy. The laser power was adjusted by means of a polarizer (wire grid, Edmund Optics) and the Al_4^+ and Al^+ yields were averaged for one minute for each power setting. A typical power measurement is depicted in Fig. 7.11. The power measurements yield a power dependence of $I^{2.9}$ for the generation of Al_4^+ and $I^{3.3}$ for the generation of Al^+ .

7.7 Conclusion

The white-light optimal control of the photo-fragmentation of Al_4^- clusters into Al^+ during charge reversal has been performed successfully, achieving optimization factors for the $(\text{Al}^+/\text{Al}_4^+)$ ratio of up to 3.4. These results confirm the wide applicability of the employed method and its high selectivity in populating specific points on the potential

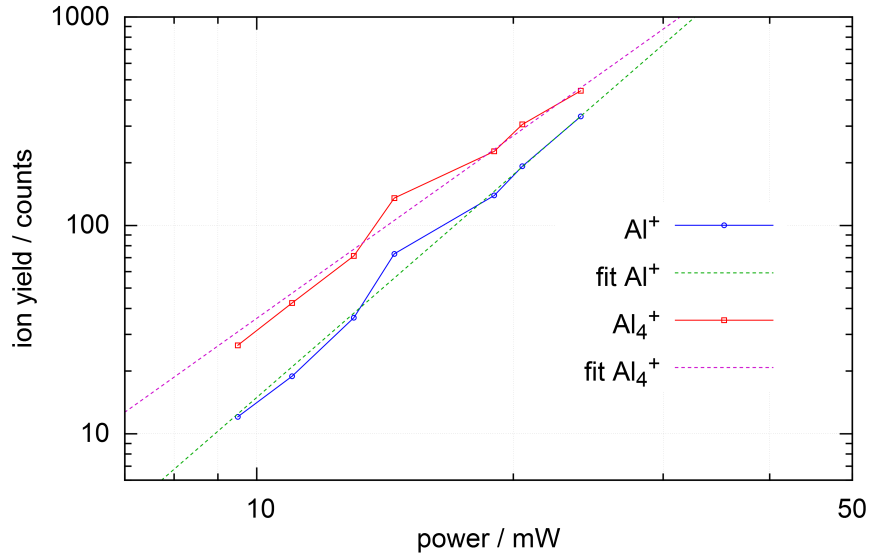


Figure 7.11: Al_4^- charge reversal power dependence measurement. The trapped Al_4^- anions are irradiated with 7 fs white-light pulses with variable pulse energy. Al_4^+ and Al^+ product cation yields are displayed on a bilogarithmic scale. The exponential fits yield a power dependence of $I^{2.9}$ for the generation of Al_4^+ and $I^{3.3}$ for Al^+ .

energy surface. As for the optimal control of the photo-fragmentation of Cu_3^- , the obtained optimal pulse shapes feature very short sub-pulse delays, suggesting that not only vibrational, but also electronic wavepackets are created and probed.

Summary and Outlook

8

8.1 Summary

This thesis set out to extend and improve the capabilities of supercontinuum laser light sources and to survey the potential of the new setup in the optimal control of small metal clusters.

A new white-light laser setup, incorporating twofold filamentation in air and ultrabroadband chirped mirrors for dispersion management, has been developed. The twofold filamentation leads to a very stable spectral broadening, supplying a significant contribution in the VIS range, leading to an output spectrum spanning from 550 nm to 900 nm at 10 % of the maximum intensity. By offset-phase correction with the pulse shaper, this spectrum is compressed to 4.9 fs pulses spanning from 510 to 950 nm, with pulse energies of up to 60 μ J and a peak power of 12 GW. These supercontinuum few-cycle pulses serve as a starting point for the tailoring of arbitrary supercontinuum pulses with few-cycle subpulses, within the sampling limit of the pulse shaper. Arbitrary tailoring of amplified supercontinuum pulses is demonstrated for the first time. The generation of 20 and 50 fs pulse trains (50 and 20 THz) is performed while maintaining sub 7 fs subpulse durations. Two-color double pulse sequences are generated with subpulse delays up to 600 fs. The desired delays in the double pulse sequences are met with high precision, confirming the accuracy of the LC-SLM's calibration, which is crucial for the determination of the electric field of optimal pulses obtained in optimal control experiments. A home-built TG-FROG apparatus allows for the characterization of pulse forms that endure several hundreds of femtoseconds with few-cycle substructures.

In a xenon multiphoton ionization experiment, the pulse shaping setup has been shown to have a temporal resolution of at least 400 as, that is preserved by the entire coherent control setup. In preliminary optimal control experiments, the setup was tested for artifacts. An offset phase correction was introduced to avoid artifacts stemming from the varying GDD of the ultrabroadband chirped mirrors in the obtained optimal pulses. The GD+GDD parametrization, which respects the limitations of the pulse shaping device, was developed and proved to be very efficient. When employing the GD+GDD parametrization, optimizations usually converged in 30 generations or less and unsuccessful optimizations occurred less frequently.

In the following, the highly versatile white-light laser system has been successfully deployed for the optimal control of two small metal clusters, the copper trimer and the aluminum tetramer. The charge reversal process of Cu_3^- anions was first investigated with 7 fs pulses, yielding the fragment product cations Cu^+ , Cu_2^+ and the charge reversed parent ion Cu_3^+ . The variation of the relative yields of the product cations was investigated during chirp scans, and the $(\text{Cu}_2^+ / \text{Cu}_3^+)$ ratio was found to increase substantially for negative and positive chirps. Hence, the $(\text{Cu}_2^+ / \text{Cu}_3^+)$ ratio was chosen as an objective for an evolutionary optimization, and was optimized by factors of up to three

when compared to the ion yields obtained with a short 7 fs pulse. The obtained nontrivial optimal pulse shapes suggest a complex excitation mechanism involving a multitude of electronic states, in which the subpulses act in a cooperative manner, such that a higher fragmentation ratio is achieved. The subpulse delays on the order of 10 fs are too fast to be probing vibrational dynamics, and thus likely are the signature of electronic wavepackets. CID experiments suggest that the fragmentation into Cu_2^+ occurs in an excited state of the neutral Cu_3 cluster, as neither Cu_3^+ nor Cu_3^- clusters fragment when irradiated with 7 fs pulses with wavelengths shorter than 540 nm blocked. Interestingly, Cu_3^- anions fragment into Cu^- anions, when irradiated with 7 fs pulses containing the shorter wavelengths, which could be a product of a decaying Cu^-Cu_2^+ ion pair state. To test the broad applicability of the experimental technique and to see whether the results obtained for the copper trimer reproduce for a markedly different model system, the optimal control of the photofragmentation of Al_4 clusters during charge reversal was studied. An initial charge reversal experiment on Al_4^- anions with 7 fs pulses was performed, yielding the fragment product cations Al^+ , Al_2^+ , Al_3^+ and the charge reversed parent ion Al_4^+ . As for Cu_3^- , the variation of the relative yields of the product cations was investigated during chirp scans, and the $(\text{Al}^+ / \text{Al}_4^+)$ ratio was found to increase substantially for negative and positive chirps. Hence, the $(\text{Al}^+ / \text{Al}_4^+)$ ratio was chosen as an objective for optimization, yielding optimization factors of up to 3.4. As for the copper trimer, the obtained optimal pulses are very complex and feature subpulse delays on the order of 10 fs, which likely are the signature of electronic wavepackets. In general, the high optimization factors obtained for two markedly different model systems, demonstrate the high selectivity in populating specific points on the potential energy surface, attainable by the presented method.

8.2 Outlook

First of all, future systems for the tailoring of supercontinuum pulses should be built with CEP stabilized laser system, as it is a well known fact that the effects of the CEP are not negligible for few-cycle pulses, but can be used for the precise control of electronic wavepackets [29, 34]. With the ability to fully control the initiation of electronic wavepackets, optimal control would be given a new powerful tool. Another great improvement to the present white-light laser system would be amplitude shaping, to enable the generation of fully parametric pulse sequences. With the current white-light spectrum (see Fig. 3.5 a)), performing amplitude shaping is not reasonable, as the strongly modulated and uneven spectrum would require the removal of excessive amounts of laser power to achieve, for instance, an ultrabroadband Gaussian spectrum. Hence, an even, unmodulated spectrum would be desirable to enable amplitude shaping, ideally with higher power. This might be achieved by filamentation in SF_6 , which can yield an almost unmodulated spectrum spanning from 400 to 900 nm [107]. Expanding the spectrum to shorter wavelengths is also desirable, for example to access the absorption bands of amino acids, proteins and nucleic acids. This could be achieved by filamentation of 800 nm pulses in air or argon, by filamentation of frequency-tripled 800 nm

pulses in argon or by filamentation of mid-IR pulses in air [146, 147, 148, 149]. Supercontinuum pulses extending into the UV could be shaped with AOMs, newly developed LC-SLMs and deep-UV pulses can be shaped with micro-electromechanical system (MEMS)-based SLMs or fused silica AOMs [32, 33, 43, 44, 150]. With the ability of tailoring parametric, CEP-stabilized supercontinuum pulses, theoretically determined pulse sequences, or waveforms, could be experimentally realized and tested. This could include quantum control incorporating the shaping of electronic wavepackets. Likewise, the active principle of experimentally determined optimal control pulses could be examined by theory, given the required processing power.

Bibliography

- [1] T. H. Maiman, "Stimulated Optical Radiation in Ruby." *Nature*, **187**:493–494, 1960.
- [2] K. Yamashita, T. Yamabe, and K. Fukui, "IRC approach to chemical dynamics: toward mode-selective chemical reactions," *Chemical Physics Letters*, **84**(1):123 – 126, 1981.
- [3] P. Felker, J. Syage, W. Lambert, and A. Zewail, "Direct observation of intramolecular energy transfer by selective picosecond laser excitation of a single chromophore in jet-cooled molecules," *Chemical Physics Letters*, **92**(1):1 – 3, 1982.
- [4] J. Perry, N. Scherer, and A. Zewail, "Picosecond pump-probe multiphoton ionization of isolated molecules: IVR and coherence," *Chemical Physics Letters*, **103**(1):1 – 8, 1983.
- [5] N. Bloembergen and A. H. Zewail, "Energy redistribution in isolated molecules and the question of mode-selective laser chemistry revisited," *The Journal of Physical Chemistry*, **88**(23):5459–5465, 1984.
- [6] D. J. Tannor and S. A. Rice, "Control of selectivity of chemical reaction via control of wave packet evolution," *The Journal of Chemical Physics*, **83**(10):5013–5018, 1985.
- [7] D. J. Tannor, R. Kosloff, and S. A. Rice, "Coherent pulse sequence induced control of selectivity of reactions: Exact quantum mechanical calculations," *The Journal of Chemical Physics*, **85**(10):5805–5820, 1986.
- [8] P. Brumer and M. Shapiro, "Control of unimolecular reactions using coherent light," *Chemical Physics Letters*, **126**(6):541 – 546, 1986.
- [9] C. K. Chan, P. Brumer, and M. Shapiro, "Coherent radiative control of IBr photodissociation via simultaneous (ω_1, ω_3) excitation," *The Journal of Chemical Physics*, **94**(4):2688–2696, 1991.
- [10] N. F. Scherer, R. J. Carlson, A. Matro, M. Du, A. J. Ruggiero, V. Romero-Rochin, J. A. Cina, G. R. Fleming, and S. A. Rice, "Fluorescence-detected wave packet interferometry: Time resolved molecular spectroscopy with sequences of femtosecond phase-locked pulses," *The Journal of Chemical Physics*, **95**(3):1487–1511, 1991.
- [11] N. F. Scherer, D. M. Jonas, and G. R. Fleming, "Femtosecond wave packet and chemical reaction dynamics of iodine in solution: Tunable probe study of motion along the reaction coordinate," *The Journal of Chemical Physics*, **99**(1):153–168, 1993.

- [12] J. Herek, A. Materny, and A. Zewail, "Femtosecond control of an elementary unimolecular reaction from the transition-state region," *Chemical Physics Letters*, **228**(1):15 – 25, 1994.
- [13] B. Kohler, V. V. Yakovlev, J. Che, J. L. Krause, M. Messina, K. R. Wilson, N. Schwentner, R. M. Whithell, and Y. Yan, "Quantum Control of Wave Packet Evolution with Tailored Femtosecond Pulses," *Phys. Rev. Lett.*, **74**:3360–3363, Apr 1995.
- [14] C. J. Bardeen, Q. Wang, and C. V. Shank, "Selective Excitation of Vibrational Wave Packet Motion Using Chirped Pulses," *Phys. Rev. Lett.*, **75**:3410–3413, Nov 1995.
- [15] D. Strickland and G. Mourou, "Compression of amplified chirped optical pulses," *Optics Communications*, **56**(3):219 – 221, 1985.
- [16] P. F. Moulton, "Spectroscopic and laser characteristics of Ti:Al₂O₃," *J. Opt. Soc. Am. B*, **3**(1):125–133, Jan 1986.
- [17] D. E. Spence, P. N. Kean, and W. Sibbett, "60-fsec pulse generation from a self-mode-locked Ti:sapphire laser," *Opt. Lett.*, **16**(1):42–44, Jan 1991.
- [18] S. Backus, C. G. Durfee, M. M. Murnane, and H. C. Kapteyn, "High power ultra-fast lasers," *Review of Scientific Instruments*, **69**(3):1207–1223, 1998.
- [19] A. M. Weiner, D. E. Leaird, J. S. Patel, and J. R. Wullert, "Programmable femtosecond pulse shaping by use of a multielement liquid-crystal phase modulator," *Opt. Lett.*, **15**(6):326–328, Mar 1990.
- [20] R. S. Judson and H. Rabitz, "Teaching lasers to control molecules," *Phys. Rev. Lett.*, **68**:1500–1503, Mar 1992.
- [21] C. J. Bardeen, V. V. Yakovlev, K. R. Wilson, S. D. Carpenter, P. M. Weber, and W. S. Warren, "Feedback quantum control of molecular electronic population transfer," *Chemical Physics Letters*, **280**(1-2):151 – 158, 1997.
- [22] A. Assion, T. Baumert, M. Bergt, T. Brixner, B. Kiefer, V. Seyfried, M. Strehle, and G. Gerber, "Control of Chemical Reactions by Feedback-Optimized Phase-Shaped Femtosecond Laser Pulses," *Science*, **282**(5390):919–922, 1998.
- [23] C. Daniel, J. Full, L. González, C. Lupulescu, J. Manz, A. Merli, t. Vajda, and L. Wöste, "Deciphering the Reaction Dynamics Underlying Optimal Control Laser Fields," *Science*, **299**(5606):536–539, 2003.
- [24] J. L. Herek, W. Wohlleben, R. J. Cogdell, D. Zeidler, and M. Motzkus, "Quantum control of energy flow in light harvesting," *Nature*, **417**:533–535, 2002.
- [25] T. Brixner, G. Krampert, T. Pfeifer, R. Selle, G. Gerber, M. Wollenhaupt, O. Graefe, C. Horn, D. Liese, and T. Baumert, "Quantum Control by Ultrafast Polarization Shaping," *Phys. Rev. Lett.*, **92**:208301, May 2004.

- [26] O. Kühn and L. Wöste (editors), *Analysis and Control of Ultrafast Photoinduced Reactions.*, Springer-Verlag, 2007.
- [27] T. Brixner, N. H. Damrauer, P. Niklaus, and G. Gerber, “Photoselektive Adaptive Femtosecond Quantum Control in the Liquid Phase.” *Nature*, **414**:57–60, 2001.
- [28] D. J. Jones, S. A. Diddams, J. K. Ranka, A. Stentz, R. S. Windeler, J. L. Hall, and S. T. Cundiff, “Carrier-Envelope Phase Control of Femtosecond Mode-Locked Lasers and Direct Optical Frequency Synthesis,” *Science*, **288**(5466):635–639, 2000.
- [29] A. Baltuska, T. Udem, M. Uiberacker, M. Hentschel, E. Goulielmakis, C. Gohle, R. Holzwarth, V. S. Yakovlev, A. Scrinzi, T. W. Hansch, and F. Krausz, “Attosecond control of electronic processes by intense light fields,” *Nature*, **421**(6923):611–615, February 2003.
- [30] J. Park, J. hwan Lee, and C. H. Nam, “Generation of 1.5 cycle 0.3 TW laser pulses using a hollow-fiber pulse compressor,” *Opt. Lett.*, **34**(15):2342–2344, Aug 2009.
- [31] G. Sansone, E. Benedetti, F. Calegari, C. Vozzi, L. Avaldi, R. Flammini, L. Polletto, P. Villoresi, C. Altucci, R. Velotta, S. Stagira, S. De Silvestri, and M. Nisoli, “Isolated Single-Cycle Attosecond Pulses,” *Science*, **314**(5798):443–446, 2006.
- [32] T. Tanigawa, Y. Sakakibara, S. Fang, T. Sekikawa, and M. Yamashita, “Spatial light modulator of 648 pixels with liquid crystal transparent from ultraviolet to near-infrared and its chirp compensation application,” *Opt. Lett.*, **34**(11):1696–1698, Jun 2009.
- [33] J. Extermann, S. M. Weber, D. Kiselev, L. Bonacina, S. Lani, F. Jutzi, W. Noell, N. F. de Rooij, and J.-P. Wolf, “Spectral phase, amplitude, and spatial modulation from ultraviolet to infrared with a reflective MEMS pulse shaper,” *Opt. Express*, **19**(8):7580–7586, Apr 2011.
- [34] M. F. Kling, C. Siedschlag, A. J. Verhoef, J. I. Khan, M. Schultze, T. Uphues, Y. Ni, M. Uiberacker, M. Drescher, F. Krausz, and M. J. J. Vrakking, “Control of Electron Localization in Molecular Dissociation,” *Science*, **312**(5771):246–248, 2006.
- [35] X. M. Tong and C. D. Lin, “Dynamics of Light-Field Control of Molecular Dissociation at the Few-Cycle Limit,” *Phys. Rev. Lett.*, **98**:123002, Mar 2007.
- [36] T. C. Weinacht, J. Ahn, and P. H. Bucksbaum, “Controlling the Shape of a Quantum Wavefunction.” *Nature*, **397**(6716):233–235, January 1999.
- [37] M. Noel and C. Stroud, “Shaping an Atomic Electron Wave Packet.” *Opt. Express*, **1**(7):176–185, Sep 1997.

- [38] F. Calegari, D. Ayuso, A. Trabattoni, L. Belshaw, S. D. Camillis, S. Anumula, F. Frassetto, L. Poletto, A. Palacios, P. Decleva, J. B. Greenwood, F. Martin, and M. Nisoli, "Ultrafast Electron Dynamics in Phenylalanine Initiated by Attosecond Pulses," *Science*, **346**:336–339, 2014.
- [39] P. Agostini, P. Breger, A. L'Huillier, H. G. Muller, G. Petite, A. Antonetti, and A. Migus, "Giant Stark shifts in multiphoton ionization," *Phys. Rev. Lett.*, **63**:2208–2211, Nov 1989.
- [40] R. J. Levis and H. A. Rabitz, "Closing the Loop on Bond Selective Chemistry Using Tailored Strong Field Laser Pulses," *The Journal of Physical Chemistry A*, **106**(27):6427–6444, 2002.
- [41] R. J. Levis, G. M. Menkir, and H. Rabitz, "Selective Bond Dissociation and Rearrangement with Optimally Tailored, Strong-Field Laser Pulses," *Science*, **292**(5517):709–713, 2001.
- [42] B. J. Sussman, D. Townsend, M. Y. Ivanov, and A. Stolow, "Dynamic Stark Control of Photochemical Processes," *Science*, **314**(5797):278–281, 2006.
- [43] A. Rondi, J. Extermann, L. Bonacina, S. Weber, and J.-P. Wolf, "Characterization of a MEMS-based pulse-shaping device in the deep ultraviolet," *Applied Physics B*, **96**(4):757–761, 2009.
- [44] M. Roth, L. Guyon, J. Roslund, V. Boutou, F. Courvoisier, J.-P. Wolf, and H. Rabitz, "Quantum Control of Tightly Competitive Product Channels," *Phys. Rev. Lett.*, **102**:253001, Jun 2009.
- [45] F. Hagemann, O. Gause, L. Wöste, and T. Siebert, "Supercontinuum pulse shaping in the few-cycle regime," *Opt. Express*, **21**(5):5536–5549, Mar 2013.
- [46] B. E. Schmidt, W. Unrau, A. Mirabal, S. Li, M. Krenz, L. Wöste, and T. Siebert, "Poor man's source for sub 7 fs: a simple route to ultrashort laser pulses and their full characterization," *Opt. Express*, **16**(23):18910–18921, Nov 2008.
- [47] B. E. Schmidt, "White Light Filamentation: Tailoring & Application for Charge Reversal of Ag_3^- ," Ph.D. thesis, Free University of Berlin, 2008.
- [48] B. E. Schmidt, O. Gause, F. Hagemann, S. Li, W. Unrau, L. Wöste, and T. Siebert, "Optimal White Light Control of the Negative to Neutral to Positive Charge Transition (NeNePo) in the Electronic Manifold of the Silver Trimer," *The Journal of Physical Chemistry A*, **116**(46):11459–11466, 2012.
- [49] M. Wollenhaupt, A. Assion, and T. Baumert, "Femtosecond Laser Pulses: Linear Properties, Manipulation, Generation and Measurement," in F. Träger (editor), "Springer Handbook of Lasers and Optics," pp. 937–983, Springer New York, 2007.

- [50] C. Rullière (editor), *Femtosecond Laser Pulses, 2nd Ed.*, Springer New York, 2005.
- [51] F. Hagemann, “Generation and Post-Amplification of Femtosecond Pulse Trains,” Diploma Thesis, Freie Universität Berlin, 2009.
- [52] A. Stingl, R. Szipöcs, M. Lenzner, C. Spielmann, and F. Krausz, “Sub-10-fs mirror-dispersion-controlled Ti:sapphire laser,” *Opt. Lett.*, **20**(6):602–604, Mar 1995.
- [53] U. Morgner, F. X. Kärtner, S. H. Cho, Y. Chen, H. A. Haus, J. G. Fujimoto, E. P. Ippen, V. Scheuer, G. Angelow, and T. Tschudi, “Sub-two-cycle pulses from a Kerr-lens mode-locked Ti:sapphire laser,” *Opt. Lett.*, **24**(6):411–413, Mar 1999.
- [54] G. Cheriaux, B. Walker, L. F. Dimauro, P. Rousseau, F. Salin, and J. P. Chambaret, “Aberration-free stretcher design for ultrashort-pulse amplification,” *Opt. Lett.*, **21**(6):414–416, Mar 1996.
- [55] E. Hecht, *Optics, 4th Ed.*, Addison Wesley, 2002.
- [56] K. Yamane, Z. Zhang, K. Oka, R. Morita, M. Yamashita, and A. Suguro, “Optical pulse compression to 3.4fs in the monocyte region by feedback phase compensation,” *Opt. Lett.*, **28**(22):2258–2260, Nov 2003.
- [57] S. Demmler, J. Rothhardt, A. M. Heidt, A. Hartung, E. G. Rohwer, H. Bartelt, J. Limpert, and A. Tünnermann, “Generation of high quality, 1.3 cycle pulses by active phase control of an octave spanning supercontinuum,” *Opt. Express*, **19**(21):20151–20158, Oct 2011.
- [58] A. Baltuška, T. Fuji, and T. Kobayashi, “Visible pulse compression to 4 fs by optical parametric amplification and programmable dispersion control,” *Opt. Lett.*, **27**(5):306–308, Mar 2002.
- [59] B. Schenkel, J. Biegert, U. Keller, C. Vozzi, M. Nisoli, G. Sansone, S. Stagira, S. D. Silvestri, and O. Svelto, “Generation of 3.8-fs pulses from adaptive compression of a cascaded hollow fiber supercontinuum,” *Opt. Lett.*, **28**(20):1987–1989, Oct 2003.
- [60] E. Matsubara, K. Yamane, T. Sekikawa, and M. Yamashita, “Generation of 2.6 fs optical pulses using induced-phase modulation in a gas-filled hollow fiber,” *J. Opt. Soc. Am. B*, **24**(4):985–989, Apr 2007.
- [61] A. M. Weiner, “Femtosecond pulse shaping using spatial light modulators,” *Review of Scientific Instruments*, **71**(5):1929–1960, 2000.
- [62] C. W. Hillegas, J. X. Tull, D. Goswami, D. Strickland, and W. S. Warren, “Femtosecond laser pulse shaping by use of microsecond radio-frequency pulses,” *Opt. Lett.*, **19**(10):737–739, May 1994.

- [63] M. Hacker, G. Stobrawa, R. Sauerbrey, T. Buckup, M. Motzkus, M. Wildenhain, and A. Gehner, "Micromirror SLM for femtosecond pulse shaping in the ultraviolet," *Applied Physics B*, **76**(6):711–714, 2003.
- [64] C. Radzewicz, P. Wasylczyk, W. Wasilewski, and J. S. Krasiski, "Piezo-driven deformable mirror for femtosecond pulse shaping," *Opt. Lett.*, **29**(2):177–179, Jan 2004.
- [65] P. Tournois, "Acousto-optic programmable dispersive filter for adaptive compensation of group delay time dispersion in laser systems," *Optics Communications*, **140**(4-6):245 – 249, 1997.
- [66] F. Weise, "Entwicklung der Pulsformung in Phase, Amplitude und Polarisation sowie kohärente Kontrolle in der MOT", Diploma thesis, Free University of Berlin, 2006.
- [67] F. Weise, "Parametric polarization pulse shaping methods and control of excitation dynamics in ultracold rubidium," Ph.D. thesis, Free University of Berlin, 2010.
- [68] A. Präkelt, M. Wollenhaupt, A. Assion, C. Horn, C. Sarpe-Tudoran, M. Winter, and T. Baumert, "Compact, robust, and flexible setup for femtosecond pulse shaping," *Review of Scientific Instruments*, **74**(11):4950–4953, 2003.
- [69] A. Bartelt, "Steuerung der Wellenpaketdynamik in kleinen Alkaliclustern mit optimierten Femtosekundenpulsen," Ph.D. thesis, Free University of Berlin, 2002.
- [70] A. M. Weiner, "Femtosecond optical pulse shaping and processing," *Progress in Quantum Electronics*, **19**(3):161–237, 1995.
- [71] J. Vaughan, T. Feurer, K. Stone, and K. Nelson, "Analysis of replica pulses in femtosecond pulse shaping with pixelated devices," *Opt. Express*, **14**(3):1314–1328, Feb 2006.
- [72] C. Hauri, W. Kornelis, F. Helbing, A. Heinrich, A. Couairon, A. Mysyrowicz, J. Biegert, and U. Keller, "Generation of intense, carrier-envelope phase-locked few-cycle laser pulses through filamentation," *Applied Physics B*, **79**(6):673–677, 2004.
- [73] J. Odhner and R. Levis, "Optical Spectroscopy Using Gas-Phase Femtosecond Laser Filamentation," *Annual Review of Physical Chemistry*, **65**(1):605–628, 2014.
- [74] M. Hercher, "Laser-induced damage in transparent media," in "Journal of the Optical Society of America," , volume 54p. 563, 1964.
- [75] R. Y. Chiao, E. Garmire, and C. H. Townes, "Self-Trapping of Optical Beams," *Phys. Rev. Lett.*, **13**:479–482, Oct 1964.

- [76] A. Couairon and A. Mysyrowicz, “Femtosecond filamentation in transparent media,” *Physics Reports*, **441**(2-4):47 – 189, 2007.
- [77] J. E. Rothenberg, “Space-time focusing: breakdown of the slowly varying envelope approximation in the self-focusing of femtosecond pulses,” *Opt. Lett.*, **17**(19):1340–1342, Oct 1992.
- [78] H. Ward and L. Bergé, “Temporal Shaping of Femtosecond Solitary Pulses in Photoionized Media,” *Phys. Rev. Lett.*, **90**:053901, Feb 2003.
- [79] L. Bergé, S. Skupin, R. Nuter, J. Kasparian, and J.-P. Wolf, “Ultrashort filaments of light in weakly ionized, optically transparent media,” *Reports on Progress in Physics*, **70**(10):1633, 2007.
- [80] A. Braun, G. Korn, X. Liu, D. Du, J. Squier, and G. Mourou, “Self-channeling of high-peak-power femtosecond laser pulses in air,” *Opt. Lett.*, **20**(1):73–75, Jan 1995.
- [81] G. Méchain, A. Couairon, Y.-B. André, C. D’Amico, M. Franco, B. Prade, S. Tzortzakis, A. Mysyrowicz, and R. Sauerbrey, “Long-range self-channeling of infrared laser pulses in air: a new propagation regime without ionization,” *Applied Physics B*, **79**(3):379–382, 2004.
- [82] R. Trebino, K. W. DeLong, D. N. Fittinghoff, J. N. Sweetser, M. A. Krumbügel, B. A. Richman, and D. J. Kane, “Measuring ultrashort laser pulses in the time-frequency domain using frequency-resolved optical gating,” *Review of Scientific Instruments*, **68**(9):3277–3295, 1997.
- [83] S. Linden, H. Giessen, and J. Kuhl, “XFROG - A New Method for Amplitude and Phase Characterization of Weak Ultrashort Pulses,” *physica status solidi (b)*, **206**(1):119–124, 1998.
- [84] F. X. Kärtner (editor), *Few-cycle laser pulse generation and its applications*, volume 95 of *Topics in Applied Physics*, Springer, 2004.
- [85] J. N. Sweetser, D. N. Fittinghoff, and R. Trebino, “Transient-grating frequency-resolved optical gating,” *Opt. Lett.*, **22**(8):519–521, Apr 1997.
- [86] A. C. Eckbreth, “BOXCARS: Crossed-beam phase-matched CARS generation in gases,” *Applied Physics Letters*, **32**(7):421–423, 1978.
- [87] R. Trebino, *Frequency-Resolved Optical Gating: The Measurement of Ultrashort Laser Pulses*, Kluwer Academic Publishers, Boston, 2002.
- [88] D. Lee, P. Gabolde, and R. Trebino, “Toward single-shot measurement of a broadband ultrafast continuum,” *J. Opt. Soc. Am. B*, **25**(6):A34–A40, Jun 2008.
- [89] M. Shapiro and P. Brumer, *Quantum Control of Molecular Processes, 2nd Ed.*, WILEY-VCH Verlag GmbH & Co. KGaA, 2011.

- [90] M. Shapiro and P. Brumer, *Principles of the Quantum Control of Molecular Processes*, John Wiley & Sons, Inc., Hoboken, New Jersey, 2003.
- [91] R. Kosloff, S. Rice, P. Gaspard, S. Tersigni, and D. Tannor, "Wavepacket dancing: Achieving chemical selectivity by shaping light pulses," *Chemical Physics*, **139**(1):201–220, 1989.
- [92] S. Shi and H. Rabitz, "Quantum mechanical optimal control of physical observables in microsystems," *The Journal of Chemical Physics*, **92**(1):364–376, 1990.
- [93] S. Shi, A. Woody, and H. Rabitz, "Optimal control of selective vibrational excitation in harmonic linear chain molecules," *The Journal of Chemical Physics*, **88**(11):6870–6883, 1988.
- [94] T. Bäck and H.-P. Schwefel, "An Overview of Evolutionary Algorithms for Parameter Optimization," *Evolutionary Computation*, **1**(1):1–23, 1993.
- [95] R. L. Fork, C. H. B. Cruz, P. C. Becker, and C. V. Shank, "Compression of optical pulses to six femtoseconds by using cubic phase compensation," *Opt. Lett.*, **12**(7):483–485, Jul 1987.
- [96] A. Baltuska, Z. Wei, M. S. Pshenichnikov, and D. A. Wiersma, "Optical pulse compression to 5 fs at a 1-MHz repetition rate," *Opt. Lett.*, **22**(2):102–104, Jan 1997.
- [97] M. Nisoli, S. D. Silvestri, O. Svelto, R. Szipöcs, K. Ferencz, C. Spielmann, S. Sartania, and F. Krausz, "Compression of high-energy laser pulses below 5 fs," *Opt. Lett.*, **22**(8):522–524, Apr 1997.
- [98] S. Sartania, Z. Cheng, M. Lenzner, G. Tempea, C. Spielmann, F. Krausz, and K. Ferencz, "Generation of 0.1-TW 5-fs optical pulses at a 1-kHz repetition rate," *Opt. Lett.*, **22**(20):1562–1564, Oct 1997.
- [99] O. Dühr, E. T. J. Nibbering, G. Korn, G. Tempea, and F. Krausz, "Generation of intense 8-fs pulses at 400 nm," *Opt. Lett.*, **24**(1):34–36, Jan 1999.
- [100] A. Wirth, M. T. Hassan, I. Grguraš, J. Gagnon, A. Moulet, T. T. Luu, S. Pabst, R. Santra, Z. A. Alahmed, A. M. Azzeer, V. S. Yakovlev, V. Pervak, F. Krausz, and E. Goulielmakis, "Synthesized Light Transients," *Science*, **334**(6053):195–200, 2011.
- [101] T. Binhammer, "Erzeugung und Anwendung geformter Laserpulse mit oktavbreitem Spektrum," Ph.D. thesis, Ruprecht-Karls-Universität Heidelberg, 2006.
- [102] S. Rausch, T. Binhammer, A. Harth, F. X. Kärtner, and U. Morgner, "Few-cycle femtosecond field synthesizer," *Opt. Express*, **16**(22):17410–17419, Oct 2008.
- [103] P. B. Corkum, C. Rolland, and T. Srinivasan-Rao, "Supercontinuum Generation in Gases," *Phys. Rev. Lett.*, **57**:2268–2271, Nov 1986.

- [104] C. Hauri, A. Guandalini, P. Eckle, W. Kornelis, J. Biegert, and U. Keller, "Generation of intense few-cycle laser pulses through filamentation - parameter dependence," *Opt. Express*, **13**(19):7541–7547, Sep 2005.
- [105] A. Guandalini, P. Eckle, M. Anscombe, P. Schlup, J. Biegert, and U. Keller, "5.1 fs pulses generated by filamentation and carrier envelope phase stability analysis," *Journal of Physics B: Atomic, Molecular and Optical Physics*, **39**(13):S257, 2006.
- [106] S. Skupin, G. Stibenz, L. Bergé, F. Lederer, T. Sokollik, M. Schnürer, N. Zhavoronkov, and G. Steinmeyer, "Self-compression by femtosecond pulse filamentation: Experiments versus numerical simulations," *Phys. Rev. E*, **74**:056604, Nov 2006.
- [107] N. Zhavoronkov, "Efficient spectral conversion and temporal compression of femtosecond pulses in SF₆," *Opt. Lett.*, **36**(4):529–531, Feb 2011.
- [108] L. Gallmann, T. Pfeifer, P. Nagel, M. Abel, D. Neumark, and S. Leone, "Comparison of the filamentation and the hollow-core fiber characteristics for pulse compression into the few-cycle regime," *Applied Physics B*, **86**(4):561–566, 2007.
- [109] F. Hagemann, F. Schwaneberg, C. Stanca-Kaposta, and L. Wöste, "White-Light Optimal Control of Photoinduced Processes," *The Journal of Physical Chemistry C*, **119**(20):10925–10934, 2015.
- [110] M. Li, J. P. Nibarger, C. Guo, and G. N. Gibson, "Dispersion-free Transient-grating Frequency-resolved Optical Gating," *Appl. Opt.*, **38**(24):5250–5253, Aug 1999.
- [111] B. Xu, Y. Coello, V. V. Lozovoy, D. A. Harris, and M. Dantus, "Pulse shaping of octave spanning femtosecond laser pulses," *Opt. Express*, **14**(22):10939–10944, Oct 2006.
- [112] D. G. Lee, J.-H. Kim, K.-H. Hong, and C. H. Nam, "Coherent Control of High-Order Harmonics with Chirped Femtosecond Laser Pulses," *Phys. Rev. Lett.*, **87**:243902, Nov 2001.
- [113] G. Cerullo, C. Bardeen, Q. Wang, and C. Shank, "High-power femtosecond chirped pulse excitation of molecules in solution," *Chemical Physics Letters*, **262**(3-4):362 – 368, 1996.
- [114] K. R. Asmis, M. Brümmer, C. Kaposta, G. Santambrogio, G. von Helden, G. Meijer, K. Rademann, and L. Wöste, "Mass-selected infrared photodissociation spectroscopy of V₄O₁₀+", *Phys. Chem. Chem. Phys.*, **4**:1101–1104, 2002.
- [115] T. Leisner, C. Rosche, S. Wolf, F. Granzer, and L. Wöste, "The Catalytic Role of Small Coinage-Metal Clusters in Photography," *Surf. Rev. Lett.*, **3**:1105, 1996.

- [116] K. J. Boyd, A. Łapicki, M. Aizawa, and S. L. Anderson, "A phase-space-compressing, mass-selecting beamline for hyperthermal, focused ion beam deposition," *Review of Scientific Instruments*, **69**(12):4106–4115, 1998.
- [117] E. C. Kaposta, "Gas Phase Infrared Photodissociation Spectroscopy Mass Selected Cluster Ions - Strong Hydrogen Bonds and Vanadium Oxides," Ph.D. thesis, Freie Universität Berlin, 2005.
- [118] O. Gause, "Femtosecond Spectroscopy and Coherent Control on Flavins in the Gas Phase," Ph.D. thesis, Freie Universität Berlin, 2012.
- [119] J. Westergren, H. Grönbeck, S.-G. Kim, and D. Tománek, "Noble gas temperature control of metal clusters: A molecular dynamics study," *The Journal of Chemical Physics*, **107**(8):3071–3079, 1997.
- [120] J. Küttner, "Reaktion kleiner Goldcluster mit Methan und Simulation des Tandem-Massenspektrometers in SIMION," Diploma Thesis, Freie Universität Berlin, 2011.
- [121] H. Haberland, M. Mall, M. Moseler, Y. Qiang, T. Reiners, and Y. Thurner, "Filling of micron-sized contact holes with copper by energetic cluster impact," *Journal of Vacuum Science & Technology A*, **12**(5):2925–2930, 1994.
- [122] P. Kelly and R. Arnell, "Magnetron sputtering: a review of recent developments and applications," *Vacuum*, **56**(3):159 – 172, 2000.
- [123] R. F. Stebbings, C. J. Latimer, W. P. West, F. B. Dunning, and T. B. Cook, "Studies of xenon atoms in high Rydberg states," *Phys. Rev. A*, **12**:1453–1458, Oct 1975.
- [124] H. Hess, K. Asmis, T. Leisner, and L. Wöste, "Vibrational wave packet dynamics in the silver tetramer probed by NeNePo femtosecond pump-probe spectroscopy," *The European Physical Journal D - Atomic, Molecular, Optical and Plasma Physics*, **16**(1):145–149, 2001.
- [125] S. Wolf, G. Sommerer, S. Rutz, E. Schreiber, T. Leisner, L. Wöste, and R. S. Berry, "Spectroscopy of Size-Selected Neutral Clusters: Femtosecond Evolution of Neutral Silver Trimers," *Phys. Rev. Lett.*, **74**:4177–4180, May 1995.
- [126] S. M. Weber, "New concepts for optimal control experiments using femtosecond pulse shaping," Ph.D. thesis, Free University of Berlin, 2007.
- [127] B. K. Rao and P. Jena, "Evolution of the electronic structure and properties of neutral and charged aluminum clusters: A comprehensive analysis," *The Journal of Chemical Physics*, **111**(5):1890–1904, 1999.
- [128] G. Ganteför, K. H. Meiwes-Broer, and H. O. Lutz, "Photodetachment spectroscopy of cold aluminum cluster anions," *Phys. Rev. A*, **37**:2716–2718, Apr 1988.

- [129] X. Li, H. Wu, X.-B. Wang, and L.-S. Wang, “*s-p* Hybridization and Electron Shell Structures in Aluminum Clusters: A Photoelectron Spectroscopy Study,” *Phys. Rev. Lett.*, **81**:1909–1912, Aug 1998.
- [130] D. Cox, D. Trevor, R. Whetten, and A. Kaldor, “Aluminum clusters: ionization thresholds and reactivity toward deuterium, water, oxygen, methanol, methane, and carbon monoxide,” *The Journal of Physical Chemistry*, **92**(2):421–429, 1988.
- [131] K. Jug, B. Zimmermann, P. Calaminici, and A. M. Köster, “Structure and stability of small copper clusters,” *The Journal of Chemical Physics*, **116**(11):4497–4507, 2002.
- [132] J. Ho, K. M. Ervin, and W. C. Lineberger, “Photoelectron Spectroscopy of Metal Cluster Anions: Cu_n^- , Ag_n^- , and Au_n^- ,” *J. Chem. Phys.*, **93**(10):6987–7002, 1990.
- [133] M. B. Knickelbein, “Electronic shell structure in the ionization potentials of copper clusters,” *Chemical Physics Letters*, **192**(1):129 – 134, 1992.
- [134] K. Ohmori, “Wave-Packet and Coherent Control Dynamics,” *Annual Review of Physical Chemistry*, **60**(1):487–511, 2009.
- [135] A. Lindinger, C. L. L. Vetter, M. Plewicky, S. M. Weber, A. Merli, and L. Wöste, “Learning from the Acquired Optimized Pulse Shape about the Isotope Selective Ionization of Potassium Dimers,” *J. Chem. Phys.*, **122**:024312/1 – 024312/9, 2005.
- [136] A. O’Keefe, J. Scherer, A. Cooksy, R. Sheeks, J. Heath, and R. Saykally, “Cavity Ring Down Dye Laser Spectroscopy of Jet-Cooled Metal Clusters: Cu_2 and Cu_3 ,” *Chem. Phys. Lett.*, **172**:214 – 218, 1990.
- [137] A. M. James, G. W. Lemire, and P. R. Langridge-Smith, “Threshold photoionisation spectroscopy of the CuAg molecule,” *Chemical Physics Letters*, **227**(4-5):503 – 510, 1994.
- [138] V. A. Spasov, T.-H. Lee, and K. M. Ervin, “Threshold Collision-Induced Dissociation of Anionic Copper Clusters and Copper Cluster Monocarbonyls,” *J. Chem. Phys.*, **112**:1713–1720, 2000.
- [139] M. F. Jarrold and K. M. Creegan, “Photodissociation of Copper Clusters, Cu_n^+ ($n=3-8$), in the 370-710 nm Wavelength Region,” *International Journal of Mass Spectrometry and Ion Processes*, **102**:161–181, 1990.
- [140] S. Paranthaman, K. Hong, J. Kim, D. E. Kim, and T. K. Kim, “Density Functional Theory Assessment of Molecular Structures and Energies of Neutral and Anionic Al_n ($n = 2 - 10$) Clusters,” *The Journal of Physical Chemistry A*, **117**(38):9293–9303, 2013.

- [141] Y. L. Zhao and R. J. Zhang, "Structures and Properties of Stable Al_4 , Al_4^+ , and Al_4^- Comparatively Studied by ab Initio Theories," *The Journal of Physical Chemistry A*, **111**(30):7189–7193, 2007.
- [142] M. Brümmer, C. Kaposta, G. Santambrogio, and K. R. Asmis, "Formation and photodepletion of cluster ion-messenger atom complexes in a cold ion trap: Infrared spectroscopy of VO^+ , VO_2^+ , and VO_3^+ ," *The Journal of Chemical Physics*, **119**(24):12700–12703, 2003.
- [143] K. Taylor, C. Pettiette, M. Craycraft, O. Chesnovsky, and R. Smalley, "Ups of negative aluminum clusters," *Chemical Physics Letters*, **152**(4-5):347 – 352, 1988.
- [144] G. Ganteför and W. Eberhardt, "Shell structure and s-p hybridization in small aluminum clusters," *Chemical Physics Letters*, **217**(5-6):600 – 604, 1994.
- [145] R. Fournier, "Trends in Energies and Geometric Structures of Neutral and Charged Aluminum Clusters," *Journal of Chemical Theory and Computation*, **3**(3):921–929, 2007.
- [146] G. Méjean, J. Kasparian, J. Yu, S. Frey, E. Salmon, R. Ackermann, J. Wolf, L. Bergé, L., and S. Skupin, "UV-Supercontinuum generated by femtosecond pulse filamentation in air: Meter-range experiments versus numerical simulations," *Applied Physics B*, **82**(3):341–345, 2006.
- [147] S. A. Trushin, K. Kosma, W. Fuß, and W. E. Schmid, "Sub-10-fs supercontinuum radiation generated by filamentation of few-cycle 800 nm pulses in argon," *Opt. Lett.*, **32**(16):2432–2434, Aug 2007.
- [148] M. Ghotbi, P. Trabs, and M. Beutler, "Generation of high-energy, sub-20-fs pulses in the deep ultraviolet by using spectral broadening during filamentation in argon," *Opt. Lett.*, **36**(4):463–465, Feb 2011.
- [149] C. Zhang, J. Wang, X. Chen, Y. Leng, R. Li, and Z. Xu, "Tunable ultraviolet source from fifth and seventh harmonic generated by mid-infrared pulses filamentation in air," *Laser Physics*, **19**(8):1793–1795, 2009.
- [150] B. J. Pearson and T. C. Weinacht, "Shaped ultrafast laser pulses in the deep ultraviolet," *Opt. Express*, **15**(7):4385–4388, Apr 2007.

Kurzfassung

Im Rahmen dieser Arbeit sollen die Fähigkeiten von Superkontinuums-Laserlichtquellen verbessert und erweitert werden, um im Anschluss das Potential des neu entwickelten Weißlicht-Lasersetups in der Optimalen Kontrolle kleiner Metallcluster zu erkunden.

Ein neues Weißlicht-Lasersetup wurde entwickelt, welches auf zweimaliger Filamentierung in Luft basiert. Die zweimalige Filamentierung in Luft bewirkt eine sehr stabile spektrale Verbreiterung, so dass ein Spektrum, welches von 550 bis 900 nm, bei 10 % der maximalen Intensität, reicht, erzeugt wird. Durch eine Phasenkorrektur im Pulsformer wird dieses Spektrum zu 4.9 fs kurzen Pulsen mit einer Energie von 60 μ J und einer Spitzenleistung von 12 GW komprimiert. Diese Pulse fungieren als Ausgangspunkt für die Erzeugung von nahezu willkürlichen Weißlichtpulsen mit Subpulsen von wenigen optischen Zyklen. Erstmals wurde die Erzeugung beinahe willkürlicher, verstärkter Weißlichtpulse demonstriert. Ein selbst konstruierter transient-grating frequency-resolved optical gating (TG-FROG)-Aufbau erlaubt die Charakterisierung von Pulsformen, die mehrere hundert Femtosekunden andauern, und Subpulse mit wenigen optischen Zyklen haben.

Dieses vielseitige Weißlicht-Lasersetup wurde erfolgreich in der Optimalen Kontrolle der Fragmentation während der Ladungsumkehr von zwei kleinen Metallclustern, dem Kupfer-Trimer und dem Aluminium-Tetramer, eingesetzt. Das Verhältnis zweier Produkt-Kationen ($\text{Cu}_2^+ / \text{Cu}_3^+$) wurde als Ziel für eine evolutionäre Optimierung ausgewählt und relativ zu einem 7 fs Puls, um den Faktor drei verbessert. Die erzeugten, nichttrivialen optimalen Pulsformen deuten auf einen komplexen Anregungsmechanismus hin, der eine Vielzahl elektronischer Zustände einbezieht. Die beobachteten Subpulsverzögerungen in der Größenordnung von 10 fs sind zu kurz um vibrationelle Dynamik abzufragen und weisen daher auf die Anregung und Abfrage elektronischer Wellenpakete hin. Kollisionsinduzierte-Dissoziationsexperimente lassen darauf schließen, dass die Fragmentation in Cu_2^+ in einem angeregten Zustand des neutralen Cu_3 -Clusters auftritt. Werden Cu_3^- Anionen mit Pulsen, die Wellenlängen kürzer als 540 nm enthalten, bestrahlt, entstehen Cu^- Anionen, was auf den Zerfall eines $\text{Cu}^- \text{Cu}_2^+$ Ionenpaar-Zustandes deuten könnte. Um die breite Anwendbarkeit der vorgestellten experimentellen Methode zu testen, und um zu prüfen, ob sich die für den Kupfer-Trimer erhaltenen Resultate für ein sehr unterschiedliches Modellsystem reproduzieren lassen, wurde im folgenden die Fragmentation während der Ladungsumkehr von Al_4^- untersucht. Das Verhältnis ($\text{Al}^+ / \text{Al}_4^+$) wurde als Ziel für eine Optimierung gewählt und konnte um Faktoren bis zu 3,4 verbessert werden. Wie schon beim Kupfer Trimer, sind die erhaltenen optimalen Pulse sehr komplex und Subpulsabstände in der Größenordnung von 10 fs deuten auf die Abfragen elektronischer Wellenpakete hin. Im Allgemeinen demonstrieren die hohen Optimierungsfaktoren, die für zwei sehr unterschiedliche Systeme erreicht wurden, die hohe Selektivität bei der Bevölkung spezifischer Punkte auf der Potentialfläche, die mit der vorgestellten Methode erreicht werden kann.

List of Publications

F. Hagemann, F. Schwaneberg, C. Stanca-Kaposta, and L. Wöste, “White-Light Optimal Control of Photoinduced Processes,” *The Journal of Physical Chemistry C*, **119**(20):10925–10934, 2015.

F. Hagemann, O. Gause, L. Wöste, and T. Siebert, “Supercontinuum pulse shaping in the few-cycle regime,” *Opt. Express*, **21**(5):5536–5549, Mar 2013.

E. Cristina Stanca-Kaposta, Falko Schwaneberg, Matias R. Fagiani, Torsten Wende, Franz Hagemann, Annett Wünschmann, Ludger Wöste, and Knut R. Asmis, “Infrared Photodissociation Spectroscopy of $C_{2n+1}N^-$ Anions with $n = 1 - 5$,” *Z. PHYS. CHEM.*, **228**(351), 2014.

B. E. Schmidt, O. Gause, F. Hagemann, S. Li, W. Unrau, L. Wöste, and T. Siebert, “Optimal White Light Control of the Negative to Neutral to Positive Charge Transition (NeNePo) in the Electronic Manifold of the Silver Trimer,” *The Journal of Physical Chemistry A*, **116**(46):11459–11466, 2012.

Danksagung

Ich bedanke mich ganz herzlich bei Prof. Dr. Ludger Wöste, dafür, dass er mir die Möglichkeit eröffnet hat, in seiner Arbeitsgruppe zu promovieren. In der AG Wöste herrschte stets eine sehr freundschaftliche Atmosphäre, so dass die Arbeit auch in schwierigen Zeiten nicht unangenehm wurde.

Cristina Stanca-Kaposta danke ich für ihre Unterstützung, vor allem am Massenspektrometer, für das Korrekturlesen des Manuskriptes und die nette Gesellschaft. Oliver Gause danke ich für seine Hilfe bei der Optimierung der Weißlichterzeugung, die Lösung von Labview-Problemen, die Unterstützung am Massenspektrometer und für die Korrektur des Manuskriptes. Ich danke Torsten Siebert für die Betreuung zu Beginn meiner Doktorarbeit und während meiner Diplomarbeit und für die vielen heiteren Gespräche. Falko Schwaneberg war immer ein zuverlässiger Laborhelfer und eine gute Gesellschaft. Matthieu Lalanne danke ich vor allem für die vielen lustigen Aktionen beim Mittagessen. Ich danke Brigitte Odeh für die bürokratische Unterstützung und dafür, dass sie sich immer liebevoll um die Geburtstagsgeschenke aller Gruppenmitglieder gekümmert hat. Albrecht Lindinger danke ich für das Anstimmen der Geburtstagslieder. Dank geht auch an Alexander Patas für die lustige Gesellschaft im Büro, fruchtbare Diskussionen und für die fachkundige Lösung von LabView-Problemen und an Georg Achazi für die angenehme Gesellschaft und gute Laser-Ratschläge. Janusz Küttner und Thomas Gelot danke ich für die lustigen Zeiten im Labor und Marek Hild für die nette Gesellschaft im Büro. Nicht zu vergessen sind auch Philipp Rohwetter, Kamil Stelmaszczyk und alle anderen Wösties, die immer für eine angenehme Atmosphäre gesorgt haben. Last but not least danke ich auch meinen Eltern für ihre Unterstützung, vor allem bei der Fertigstellung dieser Arbeit.

Eidesstattliche Erklärung

Hiermit versichere ich, die vorliegende Dissertation selbständig und ohne unerlaubte Hilfe angefertigt zu haben.

Bei der Verfassung der Dissertation wurden keine anderen als die im Text aufgeführten Hilfsmittel verwendet.

Ein Promotionsverfahren zu einem früheren Zeitpunkt an einer anderen Hochschule oder bei einem anderen Fachbereich wurde nicht beantragt.

Berlin, den

Franz Philip Hagemann